POLITECNICO DI TORINO

Corso di Lauera Magistrale in INGEGNERIA AEROSPAZIALE

Tesi di Laurea Magistrale

Comparison Between Indirect Methods and Approximate Methods for the Optimization of Low-Thrust Transfers Between LEO Orbits with J2 Perturbation

Relatore

Prof. Lorenzo CASALINO

Candidato

Federico FEDUZI

MARZO-APRILE 2025

A nonno Beppe e a Gaspare,
ovunque voi siate ora...

Comparison Between Indirect Methods and Approximate Methods for the Optimization of Low-Thrust Transfers Between LEO Orbits with J2 Perturbation

Federico Feduzi

Abstract

In recent years, space exploration has experienced an exponential increase in activities within low Earth orbit (LEO), a trend that is expected to continue in the coming years. This growth has drawn attention to the problem of orbital debris overcrowding and the need to design missions capable of actively mitigating this issue. As a result, there is a growing interest in developing more efficient missions, particularly in optimizing transfer manoeuvres to minimize either time or propellant consumption. LEO is an environment where the Keplerian orbit approximation alone is insufficient to accurately describe all relevant dynamics. In particular, the perturbation due to Earth's J2 effect must be considered to obtain precise results. However, these perturbations can also be exploited to optimize transfer trajectories. Electric propulsion is a promising candidate for future missions, offering significant advantages in terms of propellant efficiency. Numerous methods exist for optimizing low-thrust, multi-revolution transfers. Among these, the indirect method is a robust approach that relies on the numerical integration of differential equations and the shooting method to achieve optimal transfers. However, it poses significant challenges in terms of implementation and computational cost. Conversely, the arc-impulse method is based on an approximate analytical optimal solution and requires only a few iterations to converge. Although the optimal strategies derived from approximate methods may differ from those obtained using the indirect method, within its range of applicability, the arc-impulse method proves to be an effective approach for quickly estimating both propellant costs and the minimum time required for a mission. This becomes particularly advantageous when studying multi-target solutions.

Table of Contents

List of Figures

List of Tables

Chapter 1

Introduction

1.1 Purpose of the Study

In this work, the subject of trajectory optimization is addressed. The problem considered involves a low-thrust transfer between two LEO orbits with a single target, where the effect of the J2 perturbation is included. The optimization problem is studied using two different approaches: applying an indirect optimization method, which requires numerical algorithms for solution, and an approximate optimization method that relies on simplifications to obtain analytical solutions.

Optimization strategies related to LEO transfer manoeuvres are of great interest today. On the one hand, this is due to the significant advantages that LEO orbits offer for both commercial and scientific applications, and on the other hand, due to the overcrowding of these orbits, which leads to space debris problems. The following chapters aim to provide a brief overview of these issues and explain why they require significant attention from the scientific community.

1.2 Space Debris

There are numerous applications today that rely on satellites in orbit: from meteorology and climatology to telecommunications and navigation systems, all the way to human space exploration. It is certain that the use of satellite systems offers significant advantages, both from a commercial and scientific perspective. However, the exponential growth and use of such systems have led to a considerable issue: *space debris*.

The term *space debris* refers to all human-made objects, including fragments and parts thereof, that are present in Earth's orbit or re-entering the atmosphere and are no longer operational (definition according to the *Inter-Agency Space*

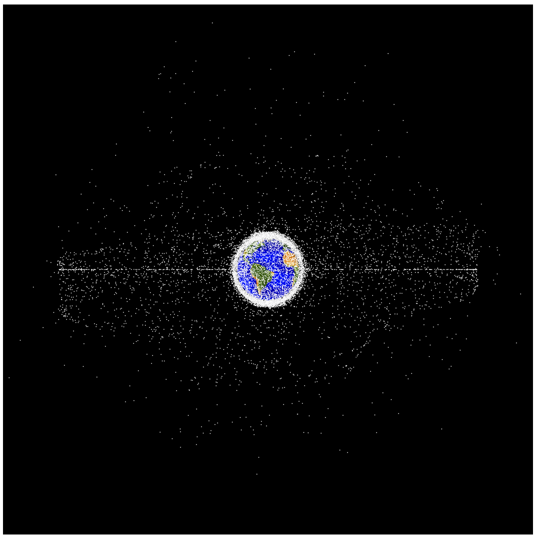

Figure 1.1: Tracked objects in Earth's orbit in 2019 [17]

Debris Coordination Committee - IADC).

In recent years, this problem has become increasingly pressing, threatening the safety of operations in Earth's orbit. According to the *ESA Space Environment Report 2024*, more satellites were launched in 2023 than in previous years, and the number and scale of commercial constellations in certain LEO orbits are continuously growing. Moreover, not enough satellites are leaving these highly congested orbits at the end of their operational life, leading currently active satellites to perform an increasing number of *collision avoidance* manoeuvrers. The adoption of countermeasures for space debris mitigation is slowly improving the situation, but it is still not enough to stop the increase in debris. Without changes, the current collective behaviour of space entities (government agencies and private companies) is not sustainable in the long term.

1.3 Historical Background

The launch of Sputnik I in 1957 not only marked the beginning of the Space Age but also the creation of the first piece of space debris. The need to track all artificial objects in orbit led the USAF (*United States Air Force*) to establish *Project Space Track*.

Space activities during the 1960s, from launches to anti-satellite (ASAT) weapon tests and the explosions of old satellites, contributed to an increase in the orbital debris population. Additional projects were created to track spacecraft in orbit, such as the *Space Object Catalogue* by NORAD (*North American Aerospace Defense Command*). The number of elements in this database tripled on June 29, 1961, following the explosion of the final stage of the Thor-Ablestar rocket, which had successfully placed the Transit-4A satellite into orbit, generating more than 200 recorded fragments. This was the first known event of the unintentional destruction of an object in space.

In 1978, NASA scientists Donald J. Kessler and Burton Cour-Palais published the paper *Collision frequency of artificial satellites: The creation of a debris belt* in the *Journal of Geophysical Research: Space Physics*, presenting a catastrophic scenario in which the growth of the space debris population is primarily driven by collisions rather than new launches. This study brought significant attention to the issue, and the scientific community began referring to this phenomenon as the *Kessler Syndrome*.

Between the 1970s and 1980s, various initiatives and programs addressing this issue emerged, including what is now known as the *Orbital Debris Program* (`OPDO`). `OPDO` began discussions with `ESA` in 1987, which later expanded to include other space agencies. During the 1980s, the *Air Force Space Debris Research Program* was established following multiple fragmentation events involving Delta launch vehicles and ASAT tests.

In 1993, the *Inter-Agency Space Debris Coordination Committee* (`IADC`) was founded with the goal of developing guidelines and coordinating efforts to manage the space debris issue and assess associated risks.

Finally, in 2001, the U.S. government released the *Orbital Debris Mitigation Standard Practices* (`ODMSP`), which represents the official U.S. guidelines for mitigating and preventing the increase of space debris. In 2004, the *European Code of Conduct for Space Debris Mitigation* was published, introducing regulations aimed at the same objective. More recently, in 2023, new policies regarding space debris mitigation came into effect as part of the *ESA's Zero Debris Approach* initiative.

1.4 Classification of Space Debris

In general, objects in orbit can be classified into two main categories: objects that can be traced back to a launch event and whose nature can be identified, and objects for which this is not possible. The latter are classified as *Unidentified* (UI), while the former are divided into:

- *Payloads* (PL), objects designed to perform specific functions in the space environment, excluding launch functions. This category includes operational satellites.
- *Payload mission-related objects* (PM), objects released as debris that served a function for the payload. A typical example is the covers of optical instrument lenses.
- *Payload fragmentation debris* (PF), fragments or objects unintentionally released from a payload whose origin can be traced back to a single event.

This category includes debris created by a payload explosion or a collision with other objects.

- *Payload debris* (PD), fragments or objects unintentionally released from a payload whose origin is unknown, but whose orbital or physical characteristics allow identification of the source.
- *Rocket body* (RB), objects designed to perform functions related to the launch. This includes upper stages of launch vehicles.
- *Rocket mission-related objects* (RM), objects intentionally released that served a function for the launcher.
- *Rocket fragmentation debris* (RF), fragments or objects unintentionally released from a launcher whose origin can be traced back to a single event.
- *Rocket debris* (RD), fragments or objects unintentionally released from a launcher whose origin is unknown, but whose orbital and physical characteristics allow identification of the source.

Space debris is primarily classified based on its size and the altitude at which it is located. The size of an object is important for tracking and for assessing the damage it can cause in the event of a collision. The larger the object, the higher the probability of collision with another object, and the greater the number of fragments generated upon impact. However, even small objects pose a significant threat, as in low Earth orbit (LEO), orbital velocities reach the order of 10 km/s. At these velocities, even fragments of 1 mm or 1 cm can cause severe impact damage to active satellites. Space debris can be therefore classified into three main categories:

- *Large Space Debris*, objects larger than 10 cm. These objects are tracked and cataloged.
- *Medium Space Debris*, objects with sizes between 1 cm and 10 cm. These objects are tracked, but with lower reliability.
- *Small Space Debris*, objects with sizes between 1 mm and 1 cm. These objects are currently not tracked.

Of particular interest are *Lethal Non-Trackable debris* (LNT). These are a subcategory of small objects, with sizes between 5 mm and 1 cm. They are too small to be tracked but large enough to cause catastrophic damage in the event of a collision with a satellite. While smaller debris is mitigated using passive protection systems such as shields, and larger debris is managed through *collision avoidance* maneuvers, LNT debris poses the highest impact risk. Debris larger than 10 cm in size are called *massive derelicts*: these include upper stages of launch vehicles and non-operational satellites. The primary threat posed by these objects is their large mass, which has the potential to

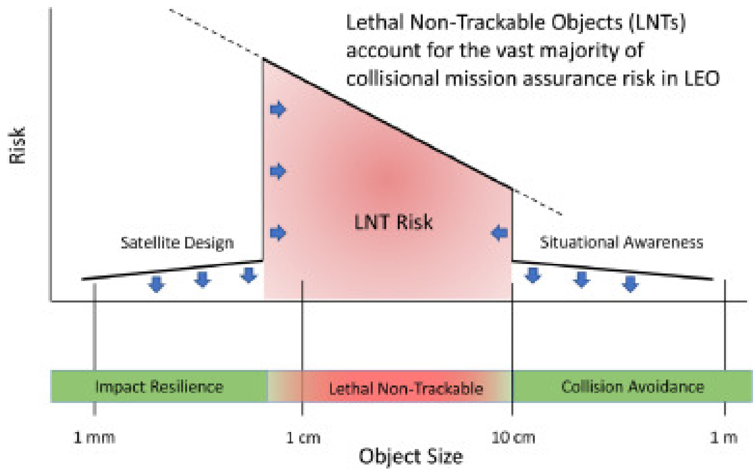

Figure 1.2: Typical risk Profile for a satellite in LEO orbit [16]

significantly increase the space debris population in the event of an explosion or collision.

1.5 Space Debris Environment

According to statistics from ESA (*European Space Agency*), since the beginning of the space age in 1957, approximately 6,740 launches have been conducted, placing a total of 19,590 satellites into orbit. Currently, around 36,860 objects are present in orbit and regularly tracked by the *US Space Surveillance Network* (SSN), of which 10,200 are currently active satellites. It is estimated that the total mass in orbit around the Earth exceeds 13,000 tons. Unfortunately, not all objects in orbit are tracked and cataloged. Using statistical models, it is estimated that there are:

- 40,500 space debris objects larger than 10 *cm*
- 1,100,000 space debris objects between 1 *cm* and 10 *cm* in size
- 130 million space debris objects between 1 *mm* and 1 *cm* in size

Large objects are continuously tracked with high precision by systems such as the *U.S. Space Surveillance Network*. The SSN tracks and maintains a public database of these objects. Medium-sized objects can be tracked with current technologies, but not always reliably: some can be tracked periodically and with reduced accuracy. The creation of the *Space Fence* radar system in 2020 by the *U.S. Space Force* has improved tracking capabilities for medium-sized objects. Tracking ability also depends on the altitude of the debris: objects in GEO orbit are more difficult to monitor precisely and rely on optical systems, whereas radar systems are used for LEO orbits.

The number of space debris objects larger than 1 *cm* (large enough to cause catastrophic damage) is extremely concerning. Particularly affected zones

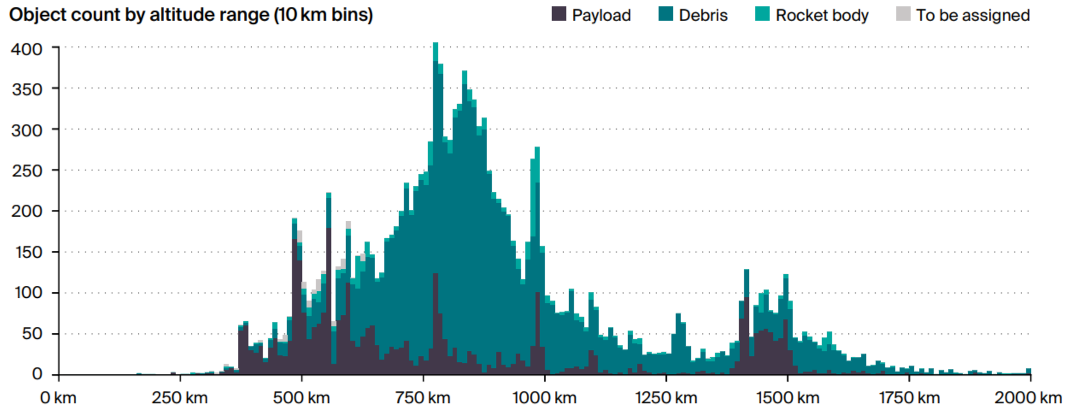

Figure 1.3: Number of objects tracked by `US SSN` in 2020 by altitude [3]

include certain LEO orbits. As shown in Figure (1.5), approximately two-thirds of active satellites are located between 500 *km* and 600 *km*. The number of satellites in this region is continuously increasing, as many of the launches conducted in 2023 were directed toward these orbits.

Every collision or explosion generating a large number of debris poses a threat to all satellites occupying these densely populated orbits and to all spacecraft that must traverse them. The number of events requiring *collision avoidance* manoeuvres is increasing, both due to the growing number of space debris and the increasing traffic in orbit.

1.6 Space Debris Formation Mechanisms

The sources of space debris can be multiple, both accidental and intentional. Almost always, the formation is related to the launcher used to place the satellite in orbit, or the satellite itself once in orbit. Among the sources of

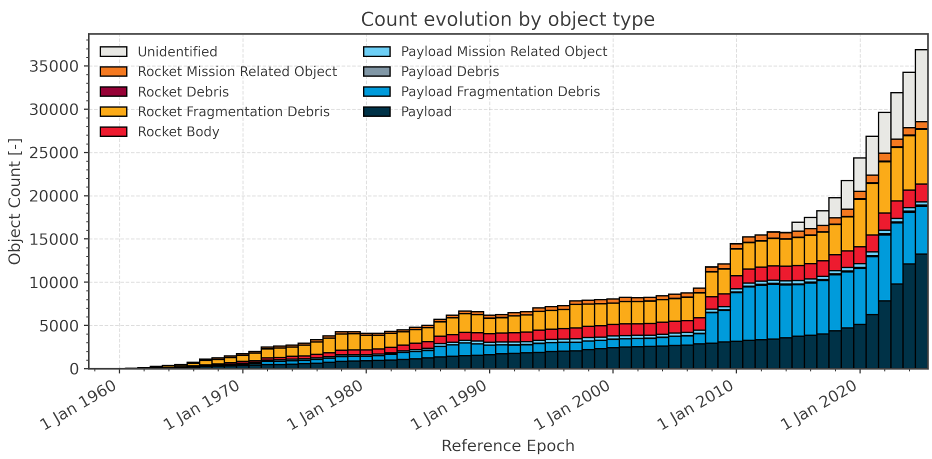

Figure 1.4: Annual objects in orbit, categorized by type [5]

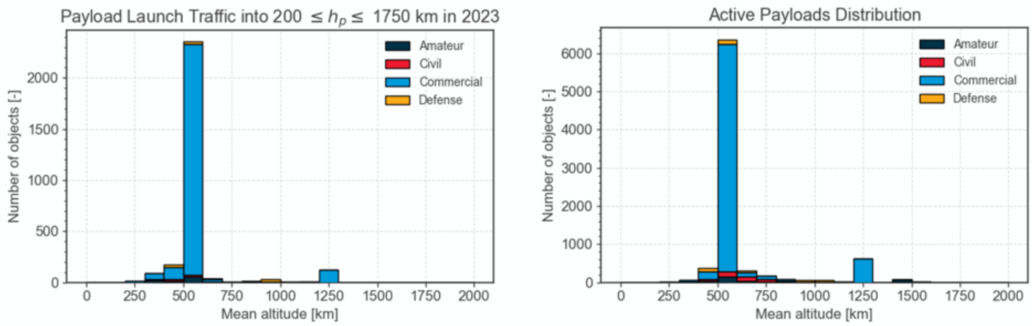

Figure 1.5: Launches to LEO orbits (left), number of active satellites in these orbits (right) [9]

intentional debris, there are:

- Objects released during spacecraft separation from the upper stage or during orbital *commissioning*. These objects include: release springs, fragments caused by pyrotechnic mechanisms, dispensers left in orbit after a multiple launch, and protective covers.
- Upper stages of launchers.
- Debris caused by the destruction of satellites due to anti-satellite (ASAT) weapon tests.
- Satellites that have reached the end of their life and are left to de-orbit naturally over several years.
- Small aluminium oxide particles produced by solid propellant rocket.

Among the sources of accidental debris, there are:

- Damage or destruction of satellites and launchers in orbit (*fragmentation events*). This can occur due to a collision with another spacecraft or space debris, or as a result of an accidental explosion.
- Intact spacecraft that, following a failure, have become inactive.
- Tools lost by astronauts during extravehicular activities.

Despite human space activity having lasted for decades, the events that have created the largest amounts of space debris have occurred in the last 20 years. Some of the most significant events include:

- **Fengyun-1C**, a Chinese meteorological satellite that was intentionally destroyed during an `ASAT` test in January 2007. It is estimated that this created 300,000 objects of 1 *cm* or larger (thus fatal size), of which about 3,300 were 10 *cm* or larger. Most of these objects remain in the satellite's orbit (850 *km* altitude, 99 inclination).

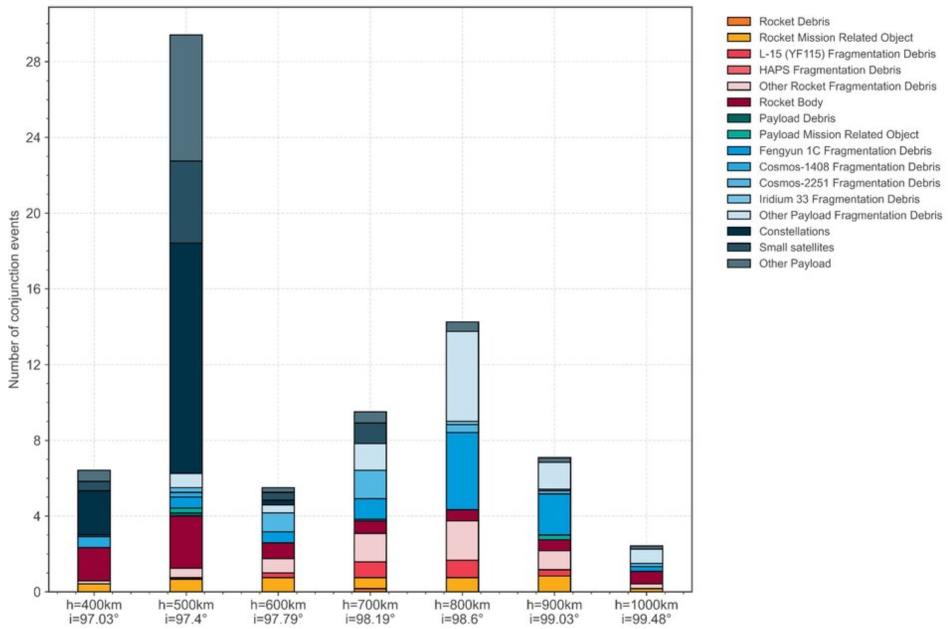

Figure 1.6: Number of conjunction events that a typical satellite at different attitudes can expect in one year [9]

- **Iridium 33 and Cosmos 2251**, two satellites that collided in February 2009. This was the first accidental collision between two large objects. Iridium 33 was an operational satellite in the Iridium constellation for telecommunications services, while Cosmos 2251 was an inactive Russian military satellite. The collision occurred at 11 km/s, destroying both satellites, creating about 200,000 objects 1 cm or larger, with about 2,000 of them being 10 cm or larger. Most of the debris is in the orbits of the two satellites, at 780 km altitude, with 86 and 74 inclinations, respectively.

- **Cosmos 1408**, an inactive Russian military satellite that was intentionally destroyed during an `ASAT` test in November 2021. It is estimated to have generated 1,500 trackable objects and several hundred thousand smaller objects. Most of the debris is located in a region between 300 km and 1,100 km in altitude and at an 82 inclination.

1.7 Response to Space Debris

The accumulation of space debris is an increasing problem that necessitates action to safeguard the future use of Earth orbits. The response to space debris can be broken down into three main strategies: Space Situational Awareness (SSA), Space Traffic Management (STM), and Space Environment Management (SEM).

Space Situational Awareness (SSA) encompasses all activities involved in providing information on orbiting objects. This includes not only the discovery, tracking, and characterization of space objects but also the distribution of this information to enable collision avoidance and ensure safe operations. SSA serves as the foundation for the other response strategies. The Space Surveillance Network (SSN), as mentioned earlier, is currently the primary source of space object data.

Space Traffic Management (STM) refers to the management of interactions between space operations and the debris population catalog, as well as the coordination of collision avoidance maneuvers. Organizations involved in STM include the Space Data Association (SDA) and Slingshot Aerospace.

Space Environment Management (SEM) activities can be divided into two categories: Passive Mitigation activities, which aim to prevent the formation of debris, and Active Remediation activities, which seek to reduce the risk once debris has already been created.

The goal of passive mitigation activities is to prevent the generation of new debris by slowing down the growth of the space debris population through careful planning and good practices during satellite operations. These measures concern both the satellite's life before launch and during its operational period. All these activities are outlined and formalized in the guidelines mentioned earlier. The main passive mitigation strategies are:

- Adequate design of the *Post Mission Disposal* (PMD), which includes *deorbiting* LEO satellites at the end of their life within a limited number of years, and *reorbiting* GEO satellites into a "graveyard" orbit.
- Collision avoidance strategies.
- Spacecraft passivation.
- Spacecraft shielding.

Active remediation activities aim to reduce the risks posed by debris once it has been generated, either by removing debris from orbit or by altering debris trajectories before predicted collisions occur. One such activity is **Active Debris Removal (ADR)**, which involves the removal of debris from space using specialized spacecraft designed for this purpose. Debris are captured using nets, harpoons, or robotic arms and then de-orbited.

The first mission to successfully demonstrate some of these technologies in orbit was the *RemoveDEBRIS* mission in 2019. The mission consisted of a mini satellite that demonstrated four key technologies: a deployable net, a vision-based navigation system, a space harpoon, and a drag sail. The vision-based navigation system was used for debris observation and for determining distances and spin rates, while the drag sail accelerated the deorbit process.

Astroscale is one of the first private companies dedicated solely to on-orbit servicing, End of Life (EOL), and ADR services. EOL services refer to the removal of objects that were launched with a docking plate, allowing for semi-cooperative removal of these objects.

The first uncrewed removal of a derelict object is planned to be conducted by the *ClearSpace-1* mission, scheduled for launch in 2028 [7]. This mission will remove the PROBA-1 satellite from orbit using four robotic arms. The mission, developed by the European Space Agency (ESA), is an in-orbit demonstration with OHB SE leading an industrial team, including the Swiss company *ClearSpace* and other subcontractors. The mission will demonstrate the technologies required for active debris removal and serve as a first step toward establishing a sustainable commercial sector in space.

Chapter 2

Fundamentals of Astrodynamics

This section provides a brief introduction to some fundamental aspects of Astrodynamics, aimed at facilitating a full understanding of the concepts and mathematical models discussed later in this work. For further information see [2], [26] and [23].

2.1 Two-Body Problem

To describe the motion of a satellite around a celestial body, the simplest mathematical model that can be used is the *so-called* two-body problem (2-BP). The 2-BP represents a simplified version of the more complex *N-body problem*. Two major assumptions are considered: the system consists only of two spherically symmetric bodies, allowing them to be treated as though their masses were concentrated at their centres, and there are no forces acting on the system other than gravitational forces.

Considering two bodies with masses M and m placed in an inertial reference frame, Newton's laws can be applied to obtain the equations:

$$m\ddot{\mathbf{r}}_m = -\frac{GMm}{r^2}\frac{\mathbf{r}}{r} \tag{2.1}$$

$$M\ddot{\mathbf{r}}_M = -\frac{GMm}{r^2}\frac{\mathbf{r}}{r} \tag{2.2}$$

where $\mathbf{r}_m$ and $\mathbf{r}_M$ are the position vectors of the two bodies with respect to the inertial reference frame, and $\mathbf{r} = \mathbf{r}_m - \mathbf{r}_M$. By subtracting the two equations, we obtain:

$$\ddot{\mathbf{r}} = -\frac{G(M+m)}{r^3}\mathbf{r} \tag{2.3}$$

When studying the motion of artificial satellites around the Earth or other planets, the mass of the orbiting object m is much smaller than the mass of the central body M. Therefore:

$$G(M+m) \simeq GM \tag{2.4}$$

and Equation (2.3) can be rewritten as:

$$\ddot{\mathbf{r}} + \frac{\mu}{r^3}\mathbf{r} = 0 \tag{2.5}$$

where the parameter $\mu = GM$ is called the *gravitational parameter.*

2.1.1 Specific Mechanical Energy

Gravitational forces are known to be conservative, as they are always directed radially toward the centre of the larger mass. Consequently, an object moving under the influence of gravity alone does not lose or gain mechanical energy, although kinetic energy can be exchanged for potential energy and vice versa.

Taking the dot product of Equation (2.5) with the velocity vector $\mathbf{V}$ yields:

$$\mathbf{V} \cdot \dot{\mathbf{V}} + \mathbf{V} \cdot \frac{\mu}{r^3}\mathbf{r} = 0 \tag{2.6}$$

where $\dot{\mathbf{V}} = \ddot{\mathbf{r}}$. The dot product $\mathbf{V} \cdot \mathbf{r}$ can be written as:

$$\mathbf{V} \cdot \mathbf{r} = rV\cos\theta = r\dot{r} \tag{2.7}$$

where $\dot{r}$ is the radial component of the position vector's rate of change. Substituting this into Equation (2.6) and simplifying the dot products leads to:

$$V\dot{V} + \dot{r}\frac{\mu}{r^2} = 0 \tag{2.8}$$

The two terms on the left-hand side can be written as:

$$\frac{d}{dt}\left(\frac{V^2}{2}\right) = V\dot{V}\ ; \qquad \frac{d}{dt}\left(-\frac{\mu}{r}\right) = \frac{\mu}{r^2}\dot{r} \tag{2.9}$$

so Equation (2.8) can be rewritten as:

$$\frac{d}{dt}\left(\frac{V^2}{2} - \frac{\mu}{r}\right) = 0 \tag{2.10}$$

Integrating Equation (2.10) with respect to time yields the expression for the *specific mechanical energy*:

$$E = \frac{v^2}{2} - \frac{\mu}{r} + c \tag{2.11}$$

where E is defined up to a constant c. In astrodynamics, c is conventionally set to zero. The term $V^2/2$ represents the *specific kinetic energy*, while the term μ/r represents the *specific potential energy.* The specific mechanical energy is also known as a *constant of motion.*

2.1.2 Specific Angular Momentum

Another *constant of motion* is the *specific angular momentum* $\mathbf{h}$. This relation can also be derived from Equation (2.5) by taking the cross product with the radius vector $\mathbf{r}$:

$$\mathbf{r} \times \ddot{\mathbf{r}} + \mathbf{r} \times \frac{\mu}{r^3}\mathbf{r} = 0 \tag{2.12}$$

The second term on the left-hand side vanishes, since $\mathbf{r} \times \mathbf{r} = 0$. The first term can be expressed as:

$$\frac{d}{dt}\left(\mathbf{r} \times \dot{\mathbf{r}}\right) = \mathbf{r} \times \ddot{\mathbf{r}} \tag{2.13}$$

so Equation (2.12) simplifies to:

$$\frac{d}{dt}\left(\mathbf{r} \times \dot{\mathbf{r}}\right) = 0 \tag{2.14}$$

Since the time derivative of $\mathbf{r} \times \dot{\mathbf{r}}$ is zero, the quantity $\mathbf{r} \times \dot{\mathbf{r}}$ must be a constant. Substituting $\dot{\mathbf{r}} = \mathbf{V}$, we obtain:

$$\mathbf{h} = \mathbf{r} \times \mathbf{V} = cost \tag{2.15}$$

This implies that a satellite's motion is confined to a fixed plane in space, since both $\mathbf{r}$ and $\mathbf{V}$ are perpendicular to $\mathbf{h}$.

2.2 Trajectory of Motion

By taking the cross product of the equation of motion (Equation (2.5)) with $\mathbf{h}$, we obtain:

$$\ddot{\mathbf{r}} \times \mathbf{h} = \frac{\mu}{r^2}(\mathbf{h} \times \mathbf{r}) \tag{2.16}$$

Observing the left-hand side and knowing that $\mathbf{h}$ is constant, it is straightforward to verify that:

$$\frac{d}{dt}\left(\dot{\mathbf{r}} \times \mathbf{h}\right) = \ddot{\mathbf{r}} \times \mathbf{h} \tag{2.17}$$

Applying some vector identities, the right-hand side of Equation (2.16) can be written as:

$$\frac{\mu}{r^2}(\mathbf{h} \times \mathbf{r}) = \frac{\mu}{r}\mathbf{v} - \frac{\mu\dot{r}}{r^2}\mathbf{r} = \frac{d}{dt}\left(\frac{\mathbf{r}}{r}\right) \tag{2.18}$$

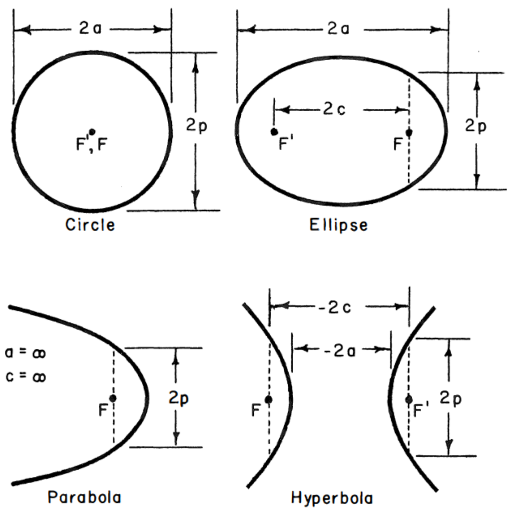

Figure 2.1: Type of conic section [2]

Thus, equation (2.16) can be rewritten as:

$$\frac{d}{dt}\left(\dot{\mathbf{r}} \times \mathbf{h}\right) = \frac{d}{dt}\left(\frac{\mathbf{r}}{r}\right) \tag{2.19}$$

Integrating both sides and taking the dot product with $\mathbf{r}$ yields the scalar equation:

$$h^2 = \mu r + rB\cos\nu \tag{2.20}$$

where B is the magnitude of the constant vector of integration $\mathbf{B}$, and ν is the angle between $\mathbf{B}$ and the radius vector $\mathbf{r}$. Solving for r, we obtain:

$$r(\nu) = \frac{h^2/\mu}{1 + \frac{B}{\mu}\cos\nu} \tag{2.21}$$

Equation (2.21) represents the trajectory expressed in polar coordinates. Comparing this expression with the general equation of a conic section in polar coordinates:

$$r(\nu) = \frac{p}{1 + e\cos\nu} \tag{2.22}$$

we see that the two equations are identical. Therefore, the solution of the two-body problem is a conic section. The parameter $p = h^2/\mu$ is called the *semi-latus rectum*, and $e = B/\mu$ is the *eccentricity*, which determines the type of conic section. The polar angle ν, known as the *true anomaly*, is the angle between $\mathbf{r}$ and the periapsis.

There are four types of conic sections, showed in Figure (2.1) : the circle ($e = 0$), the ellipse ($0 < e < 1$), the parabola ($e = 1$) and the hyperbola ($e > 1$). All conic sections have two foci, one of which marks the location of the central body. Geometrically, the eccentricity is defined as:

$$e = \frac{c}{a} \tag{2.23}$$

where c is the distance between the foci, and a is the *semi-major axis*. The semi-latus rectum p is geometrically defined as:

$$p = a\left(1 - e^2\right) \tag{2.24}$$

The extreme endpoints of the semi-major axis are called the *apses*. The nearest point to the central body is known as *periapsis*, while the farthest point is called *apoapsis*. These can be expressed geometrically by substituting $\nu = 0°$ and $\nu = 180°$ into the polar equation:

$$r_p = \frac{p}{1+e} = a(1-e) \tag{2.25}$$

$$r_a = \frac{p}{1-e} = a(1+e) \tag{2.26}$$

Another important angle is the *flight-path angle* ϕ, defined as the angle between the velocity vector $\mathbf{V}$ and the local horizon. The angular momentum h can be expressed in terms of ϕ:

$$h = rv\cos\phi. \tag{2.27}$$

At the apses, the velocity vector is aligned with the local horizon, so $\phi = 0$, and:

$$h = r_p v_p = r_a v_a. \tag{2.28}$$

By specifying the energy equation at the periapsis:

$$E = \frac{v^2}{2} - \frac{\mu}{r} = \frac{h^2}{2r_p^2} - \frac{\mu}{r_p}, \tag{2.29}$$

and using $p = \frac{h^2}{\mu}$, as well as $p = a\left(1 - e^2\right)$, leads to:

$$h^2 = \mu a\left(1 - e^2\right), \tag{2.30}$$

and substituting Equations (2.25) and (2.30) into (2.29), yields:

$$E = \frac{\mu a\left(1 - e^2\right)}{2a^2(1-e)^2} - \frac{\mu}{a(1-e)} = -\frac{\mu}{2a}. \tag{2.31}$$

Thus, the specific mechanical energy E is inversely proportional to the semi-major axis a, indicating that an increase in mechanical energy corresponds to an increase in orbit size. To summarize, h determines p, E determines a, and together they determine e:

$$p = a\left(1 - e^2\right) \quad \longrightarrow \quad e = \sqrt{1 - \frac{p}{a}} = \sqrt{1 + \frac{2Eh^2}{\mu^2}}. \tag{2.32}$$

2.2.1 The Elliptical Orbit

One of the most common types of orbits is the elliptical orbit. All the planets in the solar system, as well as the orbits of Earth satellites, follow elliptical trajectories. The ellipse is a closed curve, meaning that an object in an elliptical orbit repeatedly travels along the same path. The time required for an object to complete one full revolution around its orbit is called the *orbital period.*

Referring to Figure (2.2), it is easy to observe that the quantity $(r + r')$ remains constant. It can be straightforwardly demonstrated that:

$$r + r' = 2a \tag{2.33}$$

where a is the semi-major axis. Similarly, the apoapsis (r_a) and periapsis (r_p) are related to the semi-major axis as follows:

$$r_p + r_a = 2a \tag{2.34}$$

It can also be easily verified that:

$$r_a - r_p = 2c \tag{2.35}$$

where c is the distance from the center of the ellipse to one of its foci. By combining these relations with Equation (2.23), a new expression for the eccentricity e is obtained:

$$e = \frac{r_a - r_p}{r_a + r_p} \tag{2.36}$$

Referring to Figure (2.3), the horizontal component of the velocity of an object

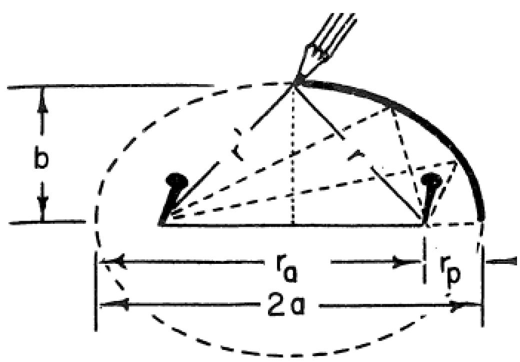

Figure 2.2: Geometric construction of an ellipse [2]

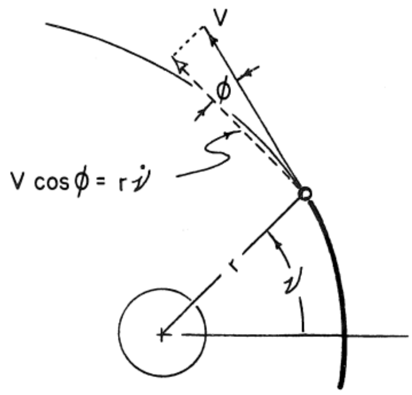

Figure 2.3: Horizontal component of **V** [2]

in an elliptical orbit can be expressed as:

$$V\cos\phi = r\dot{\nu} \tag{2.37}$$

Using the definition of specific angular momentum, it is possible to write:

$$h = r^2\frac{d\nu}{dt} \quad \longrightarrow \quad dt = \frac{r^2}{h}d\nu \tag{2.38}$$

The differential area dA swept by the radius vector as it moves through an angle $d\nu$ can be expressed as:

$$dA = \frac{1}{2}r^2 d\nu \tag{2.39}$$

Combining Equations (2.38) and (2.39), yields:

$$dt = \frac{2}{h}dA \tag{2.40}$$

Over one orbital period, the total area swept by the radius vector is the entire area of the ellipse, so integrating the Equation (2.40) over one orbital period gives:

$$T = \frac{2\pi ab}{h} \tag{2.41}$$

where b is the *semi-minor axis*. Using the geometric relation between the semi-major and semi-minor axes, $a^2 - b^2 = c^2$, and knowing that $h = \sqrt{\mu p}$, leads to:

$$T = \frac{2\pi}{\sqrt{\mu}}a^{3/2} \tag{2.42}$$

Thus, the orbital period of an elliptical orbit depends only on the size of the orbit, specifically the semi-major axis a. This equation also confirms Kepler's third law: *"The square of the orbital period is proportional to the cube of the* *semi-major axis"*.

2.2.2 The Circular Orbit

A circular orbit can be considered a special case of an elliptical one. In this case, $e = 0$, meaning that $r_a = r_p$. In this scenario, the semi-major axis is equivalent to the radius, and equation (2.42) simplifies to:

$$T = \frac{2\pi}{\sqrt{\mu}} r^{3/2} \tag{2.43}$$

A useful quantity is the *circular speed*, which represents the velocity required to maintain an object in a circular trajectory. This velocity can be directly evaluated using the mechanical energy equation for a circular orbit:

$$E = \frac{v_c^2}{r_c} - \frac{\mu}{r_c} = -\frac{\mu}{2r_c}. \tag{2.44}$$

Solving for v_c leads to:

$$v_c = \sqrt{\frac{\mu}{r_c}}. \tag{2.45}$$

Circular velocity is inversely proportional to the orbit radius. Thus, maintaining a satellite in a low-altitude Earth orbit requires greater velocity compared to a much higher orbit.

2.3 Coordinate System

The first step in describing an orbit is to select a suitable inertial reference frame. The choice of the reference frame depends on the specific problem being studied. For instance, when studying orbits of planets, asteroids, comets, or deep-space probes, a heliocentric-ecliptic coordinate system is commonly used. Conversely, for satellites orbiting the Earth, a geocentric-equatorial coordinate system is often a more suitable choice.

To fully define these coordinate systems (e.g., x, y, z), three key elements must be specified:

- The location of the origin of the system.
- The orientation of the fundamental plane (e.g., the x-y plane).
- A principal direction within the fundamental plane (e.g., the x direction).

One axis of the reference frame is defined as being perpendicular to the fundamental plane (e.g., the z axis), with its positive direction explicitly

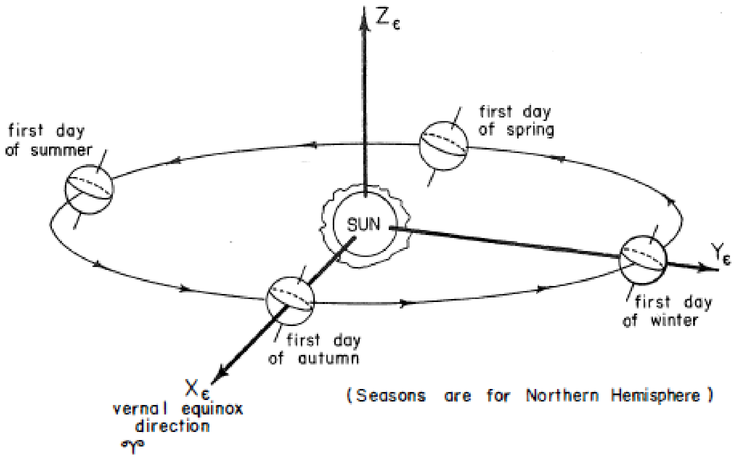

Figure 2.4: Heliocentric-ecliptic coordinate system [2]

specified. The final axis is then chosen to complete a right-handed coordinate system.

2.3.1 The Heliocentric-Ecliptic Coordinate System

The Heliocentric-Ecliptic Coordinate System [$\mathbf{X_e}$,$\mathbf{Y_e}$,$\mathbf{Z_e}$] (with reference to Figure (2.4)) has its origin at the centre of the Sun. The fundamental plane, $\mathbf{X_e}$-$\mathbf{Y_e}$, coincides with the *ecliptic*, which is the plane of Earth's orbit. The principal direction, $\mathbf{X_e}$, is defined as the line of intersection between the ecliptic plane and Earth's equatorial plane at the time of the *Vernal Equinox*. The $\mathbf{Z_e}$ axis is perpendicular to the ecliptic plane, with its positive direction pointing towards the hemisphere that contains *Polaris*. Finally, the $\mathbf{Y_e}$ axis completes the right-handed coordinate system.

This coordinate system is not perfectly inertial: the Earth experiences a slight wobble, and its axis of rotation gradually shifts direction over the centuries. As a result, the line of intersection between Earth's equatorial plane and the ecliptic plane slowly changes position. This phenomenon is known as the *precession of the equinoxes*.

2.3.2 The Geocentric-Equatorial Coordinate System

The Geocentric-Equatorial Coordinate System [$\hat{\mathbf{I}}$, $\hat{\mathbf{J}}$, $\hat{\mathbf{K}}$] (with reference to Figure (2.5)) has its origin at the centre of the Earth. The fundamental plane, $\hat{\mathbf{I}}$-$\hat{\mathbf{J}}$, is defined as Earth's equatorial plane. The principal direction, $\hat{\mathbf{I}}$, is always parallel to $\mathbf{X_e}$, with its positive direction pointing toward the Vernal Equinox. The $\hat{\mathbf{K}}$ axis is perpendicular to the equatorial plane, with its positive direction pointing toward the hemisphere that contains *Polaris*. Finally, the $\hat{\mathbf{J}}$ axis completes the right-handed coordinate system.

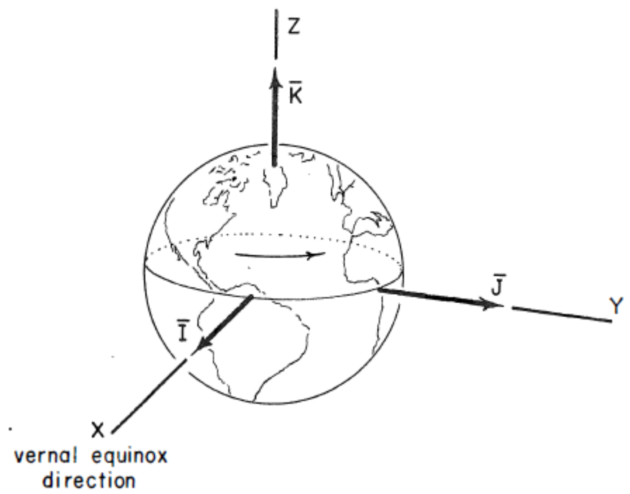

Figure 2.5: Geocentric-equatorial coordinatfl system [2]

This coordinate system is sometimes referred to as the Earth-Centered Inertial (ECI) system. It is not fixed to the Earth, instead, the Earth rotates relative to it.

2.3.3 The Perifocal Coordinate System

The perifocal coordinate system [$\hat{\mathbf{p}}$, $\hat{\mathbf{q}}$, $\hat{\mathbf{w}}$] (with reference to Figure (2.6)) is one of the most commonly used reference systems for describing the motion of a satellite. Its origin is located at the centre of the central body. The fundamental plane, $\hat{\mathbf{p}}$-$\hat{\mathbf{q}}$, is defined as the orbital plane. The principal direction, $\hat{\mathbf{p}}$, points toward the perigee. The $\hat{\mathbf{q}}$ axis is rotated 90° from the $\hat{\mathbf{p}}$ axis in the direction of the satellite's motion, and it identifies the semilatus rectum. The $\hat{\mathbf{w}}$ axis is perpendicular to the orbital plane, completing the right-handed coordinate system.

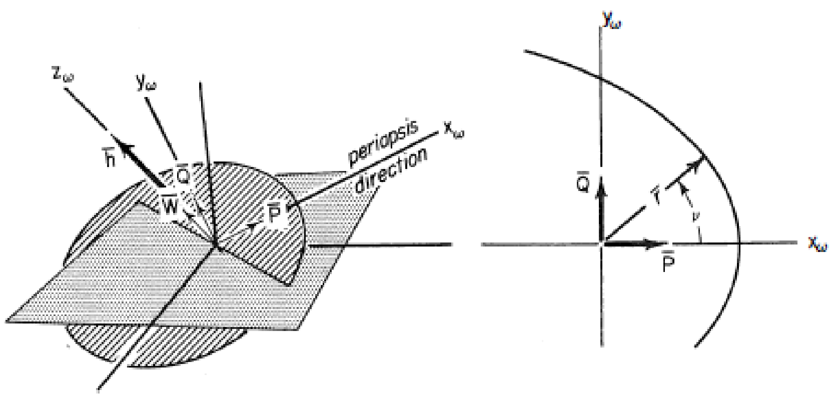

Figure 2.6: Perifocal coordinate system [2]

2.4 Classical Orbital Elements

Six scalar values are required to fully describe an orbit. These can be represented, for example, by the three components of the radius vector and the three components of the velocity vector. However, these components are time-dependent and may not be an optimal choice for orbital representation.

In Astrodynamics are commonly used the *Classical Orbital Elements*, a set of five scalar values which are time-independent for a Keplerian orbit, that describe the size, shape, and orientation of the orbit. Additionally, one time-dependent scalar value is needed to determine the position of the satellite along the orbit at a specific time. These values are defined as follows with reference to Figure (2.7):

- a (*semi-major axis*): Defines the size of the orbit.
- e (*eccentricity*): Defines the shape of the orbit.
- i (*inclination*): The angle between the **K** unit vector and the orbital angular momentum vector **h**.
- Ω (*longitude of the ascending node*): The angle in the fundamental plane between the **I** unit vector and the ascending node, the point where the satellite crosses the fundamental plane in a south-to-north direction.
- ω (*argument of periapsis*): The angle, within the plane of the satellite's orbit, between the ascending node and the periapsis (the point of closest approach to the central body).
- ν (*true anomaly*): The angle, within the orbital plane, that specifies the satellite's position at a given time. It is measured between the periapsis and the radius vector pointing to the satellite.

These elements are commonly used to describe the orbit of a satellite in the geocentric-equatorial system or the orbit of a planet in the heliocentric-ecliptic system. In certain special cases, when some of the classical orbital elements are undefined, alternative elements are used (Figure (2.8)):

- Π (*longitude of periapsis*): The angle in the orbital plane from **I** to the periapsis. This element is particularly useful when the ascending node is undefined (e.g., in an equatorial orbit). If both Ω and ω are defined, then $\Pi = \Omega + \omega$.
- u (*argument of latitude at epoch*): The angle in the orbital plane between the ascending node and the radius vector. It is used when the periapsis

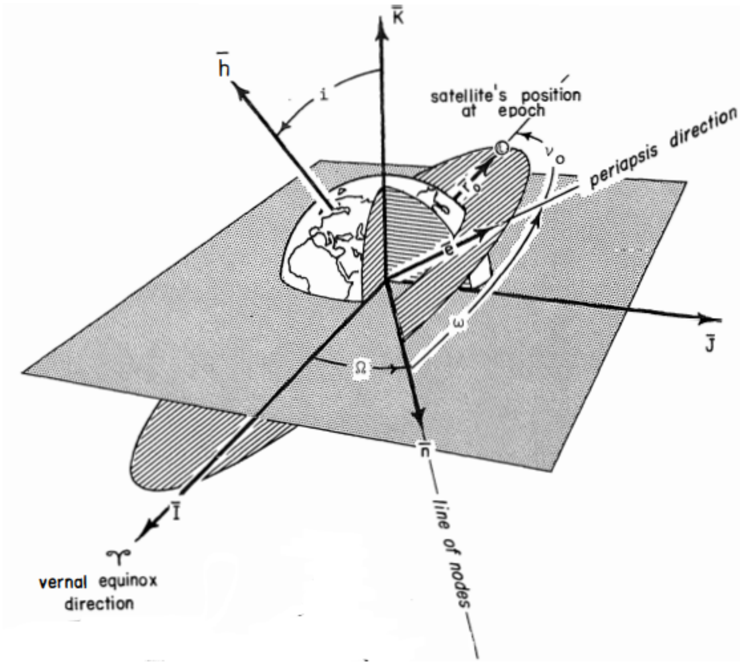

Figure 2.7: Classical Orbital elements [2]

(and consequently ν) is undefined (e.g., in a circular orbit). If both ω and ν are defined, then $u = \omega + \nu$.

- l (*true longitude at epoch*): The angle in the orbital plane between **I** and the radius vector. It is used when both Ω and ω are undefined (e.g., in a circular equatorial orbit). If both Ω and ω are defined, then $l = \Omega + \omega$. If Ω is undefined, then $l = \Pi + \nu$, and if ω is undefined, then $l = \Omega + u$.

2.5 Orbital Perturbation

A perturbation is a deviation from the expected motion. The two-body problem is a simplification of the real problem of satellite motion. In the assumptions made in the 2-BP, the gravitational pull of the central body is considered the only force acting on the system. The orbits that are solutions to the 2-BP are known as *Keplerian orbits*, which are idealized orbit inertially fixed. However, the action of other forces, such as the gravitational pull of other objects, atmospheric drag, or the radiation pressure of the Sun, perturbs the orbit, making the results of the 2-BP inaccurate in certain cases.

For example, during interplanetary missions, the gravitational attraction of other objects can be as large as, or even larger than, the primary gravitational force. If the perturbing effects of these bodies were not considered, the spacecraft could miss its target entirely. For satellites in low-altitude orbits, neglecting atmospheric drag can significantly shorten their operational lifespan, as this

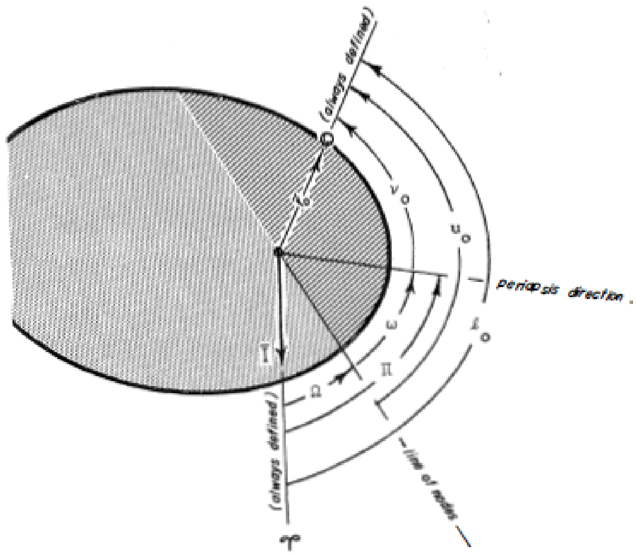

Figure 2.8: Relations between orbital elements [2]

perturbation causes the orbit to decay. It is important to understand the environment in which satellites operate to determine which perturbative effects must be taken into account to accurately predict their motion.

The study of perturbations requires specific techniques. There are two main categories, referred to as *Special Perturbations* and *General Perturbations.* In Special Perturbation methods, all necessary perturbing effects are included in the equations of motion, which are then directly integrated using numerical methods. Two widely known Special Perturbation methods are Cowell's method and Encke's method. In this approach, the satellite's trajectory is no longer a conic section. In General Perturbation methods, the perturbing acceleration is expressed as a series expansion and is then integrated analytically. This analytic approach produces closed-form solutions. In general, these techniques are more complex and time-consuming, but they provide a deeper understanding of the sources and effects of perturbations.

Generally, perturbations can be divided into *periodic* and *secular* perturbations. Periodic perturbations cause the orbital elements to change in a periodic fashion, while secular perturbations cause the orbital elements to continuously increase or decrease over time. Periodic perturbations can be further classified into *Short-Period variations*, where the period of the perturbation is less than or comparable to the orbital period, and *Long-Period variations*, where the period is greater than the orbital period.

2.5.1 The Nonspherical Earth

In the previous sections, we represented the gravitational potential of the Earth as μ/r, which is valid for a spherically symmetric mass body. However, the

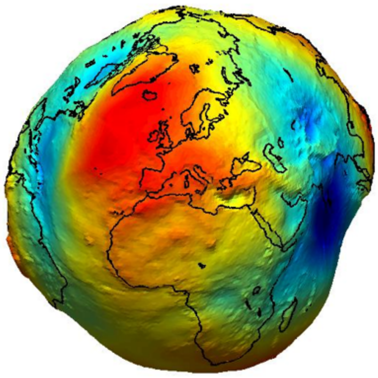

Figure 2.9: Earth's geoid as seen by GOCE [8]

Earth cannot be accurately represented as a spherically symmetric mass body, as its shape is more complex: it bulges at the equator, is flattened at the poles, and is generally asymmetric. This causes the gravitational potential field to be distorted and not fully represented by μ/r. The field of *Geodesy* is dedicated to studying and representing the geometry and gravitational field of the Earth. This discipline introduces the concept of the *Geoid*, a surface that coincides with the mean ocean surface and is used to describe the Earth's shape.

General potential theory shows that the gravitational field at a point P, external to the Earth, can be described in geocentric spherical coordinates as:

$$\begin{aligned} &U(r, \phi, \lambda) \\ &\quad = -\frac{\mu}{r}\left[1 + \sum_{n=2}^{\infty}\sum_{m=0}^{n}\left(\frac{R_e}{r}\right)^n P_{n,m}(\sin\phi)\left\{C_{n,m}\cos(m\lambda) + S_{n,m}\sin(m\lambda)\right\}\right] \end{aligned} \tag{2.46}$$

where:

- r, ϕ, and λ are the geocentric spherical coordinates: r is the geocentric distance of point P, ϕ is the geocentric latitude, and λ is the geocentric longitude measured from the Greenwich meridian.
- R_e is the Earth's mean equatorial radius.
- $C_{n,m}$ is known as the *tesseral harmonic coefficient*.
- $S_{n,m}$ is known as the *sectorial harmonic coefficient*.
- $P_{n,m}(\sin\phi)$ is the associated Legendre polynomial of the first kind, of degree n and order m.

Typically, terms with $m = 0$ are separated from those with $m \neq 0$, allowing equation (2.46) to be rewritten as:

$$U(r,\phi,\lambda) = -\frac{\mu}{r}\left[1 + \sum_{n=2}^{\infty} C_{n,0}\left(\frac{R_e}{r}\right)^n P_{n,0}(\sin\phi) + \sum_{n=2}^{\infty}\sum_{m=1}^{n}\left(\frac{R_e}{r}\right)^n P_{n,m}(\sin\phi)\left\{C_{n,m}\cos(m\lambda) + S_{n,m}\sin(m\lambda)\right\}\right] \tag{2.47}$$

It is possible to further define:

$$J_n = J_{n,0} = -C_{n,0}\ ; \qquad P_n = P_{n,0} \tag{2.48}$$

$$C_{n,m} = J_{n,m}\cos(m\lambda_{n,m})\ ; \qquad S_{n,m} = J_{n,m}\sin(m\lambda_{n,m}) \tag{2.49}$$

and substituting into equation (2.47), yields:

$$U(r,\phi,\lambda) = -\frac{\mu}{r}\left[1 - \sum_{n=2}^{\infty} J_n\left(\frac{R_e}{r}\right)^n P_n(\sin\phi) + \sum_{n=2}^{\infty}\sum_{m=1}^{n} J_{n,m}\left(\frac{R_e}{r}\right)^n P_{n,m}(\sin\phi)\cos\left(m(\lambda - \lambda_{n,m})\right)\right] \tag{2.50}$$

where $P_n(\sin\phi)$ are the Legendre polynomials of degree n and J_n are known as the *zonal harmonic coefficients*.

A gravity model essentially consists of the values of $C_{n,m}$, $S_{n,m}$, $J_{n,m}$, along with the values of μ and R_e. For example, the EGM84 model (*Earth Gravitational Model 84*) contains up to 32,400 terms ($n = m = 180$), the EGM96 model contains up to 130,000 terms ($n = m = 360$), and the EGM2008 model includes more than $4.6 \cdot 10^6$ terms ($n = 2190$, $m = 2159$).

For most applications in astrodynamics, a simplified version of these models is used, including only the terms that significantly contribute to orbital perturbations. It is useful to decompose Equation (2.50): the first term represents the gravitational potential of a spherically symmetric mass body, the second term represents the *zonal harmonics*, and the third term represents the *tesseral and sectorial harmonics*. Tesseral and sectorial harmonics are sometimes neglected, as their effects are difficult to predict and do not contribute significantly to secular perturbations. In this work, only zonal harmonics are considered.

2.5.1.1 Zonal Harmonics

The zonal harmonics represent the influence of deviations in the shape and mass density distribution of the Earth in the north-south direction. Extracting

Figure 2.10: Zonal harmonics (left), sectorial harmonics (centre) and tesseral harmonics (right) [26]

the relevant terms from Equation (2.50), yields:

$$U_{zonal}(r,\phi) = -\frac{\mu}{r}\sum_{n=2}^{\infty} J_n \left(\frac{R_e}{r}\right)^n P_n(\sin\phi) \tag{2.51}$$

where the Legendre polynomials are given by:

$$P_n(x) = \frac{1}{2^n n!}\frac{d^n}{dx^n}\left(x^2-1\right)^n \tag{2.52}$$

Through substitution and algebraic manipulation, the terms that compose $U_{zonal}(r,\phi)$ can be derived:

$$\begin{aligned}
&U_0 = -\frac{\mu}{r}\\
&U_{J1} = 0\\
&U_{J2} = \left(\frac{R_e}{r}\right)^2 J_2\left(3\sin^2\phi - 1\right)\\
&U_{J3} = \left(\frac{R_e}{r}\right)^3 J_3\left(5\sin^3\phi - 3\sin\phi\right)
\end{aligned} \tag{2.53}$$

As can be seen in Table (2.1), the first zonal harmonic term, J_2, is significantly larger than the others, making it the dominant perturbative effect. This is why, in astrodynamics, it is commonly referred to as the J_2 *effect* or J_2 *perturbation*, which is the most significant perturbation considered in this work. The primary influence of J_2 is on the right ascension of the ascending node, Ω, and the argument of periapsis, ω. The effect on Ω is known as the *regression of the line of nodes*, which consists of the rotation of the orbital plane around

	$J_n(10^{-6})$
J_1	0
J_2	1082.6357
J_3	-2.5324737
J_4	-1.6199743
J_5	-0.2279051

Table 2.1: Selected coefficients from the GRACE GGM02C Earth gravity field model [26]

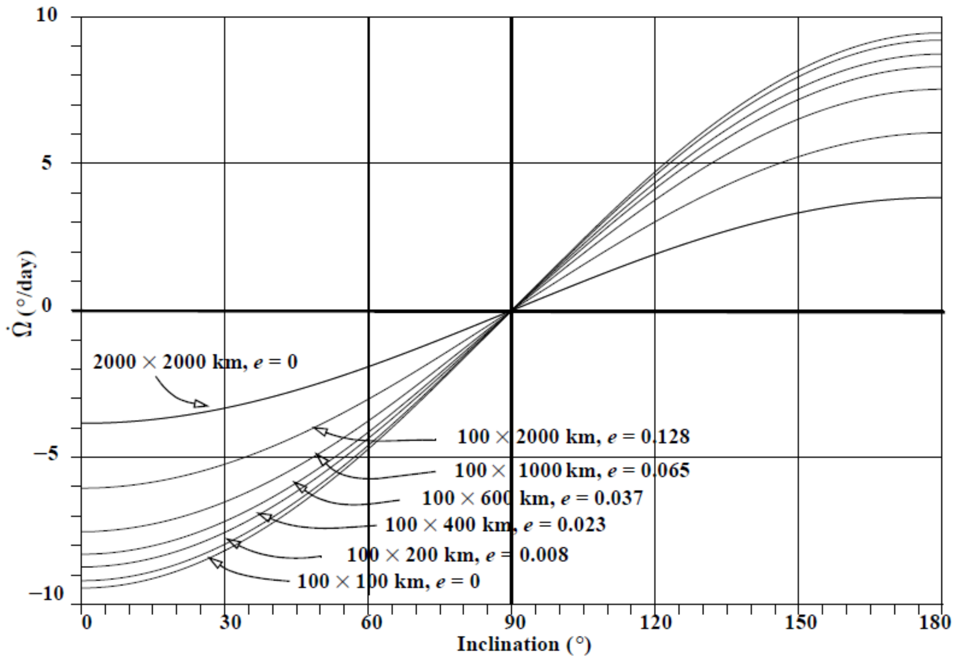

Figure 2.11: Variation of $\dot{\Omega}_{J2}$ for different combinations of altitude and orbital inclination [23]

the Earth's rotation axis at a rate that depends on both orbital inclination and altitude. By manipulating equation (2.53), we obtain:

$$\left(\frac{d\Omega}{dt}\right)_{J2} = -\frac{3}{2}J_2\left(\frac{R_e}{a(1-e^2)}\right)^2\sqrt{\frac{\mu}{a^3}}\cos(i) \tag{2.54}$$

Thus, the regression of the line of nodes is inversely proportional to the altitude of the orbit and directly proportional to the cosine of the inclination. As shown in Figure (2.11), $\dot{\Omega}_{J2}$ is strongest for low Earth orbits. This effect can be exploited to achieve a special type of orbit called a *Sun-synchronous orbit* (SSO), where the angular velocity of the line of nodes, $\dot{\Omega}$, matches the Earth's revolution around the Sun. When $i = 90°$ (polar orbits) $\dot{\Omega}_{J2}$ is zero regardless the altitude, for $i > 90°$ the line of nodes precedes.

Another effect of the zonal harmonics is the *rotation of the line of apsides*, which consists of the in-plane rotation of the major axis. The rate of this precession (or regression) also depends on orbit altitude, inclination angle and eccentricity:

$$\left(\frac{d\omega}{dt}\right)_{J2} = \frac{3}{4}J_2\left(\frac{R_e}{a(1-e^2)}\right)^2\sqrt{\frac{\mu}{a^3}}(5\cos^2 i - 1) \tag{2.55}$$

As shown in Figure (2.12), there exists a critical inclination angle of 63.4° at which $\dot{\omega}_{J2} = 0$ regardless of altitude. This is often exploited in special orbits known as *Molniya orbits*. For inclinations less than 63.4°, the line of apsides

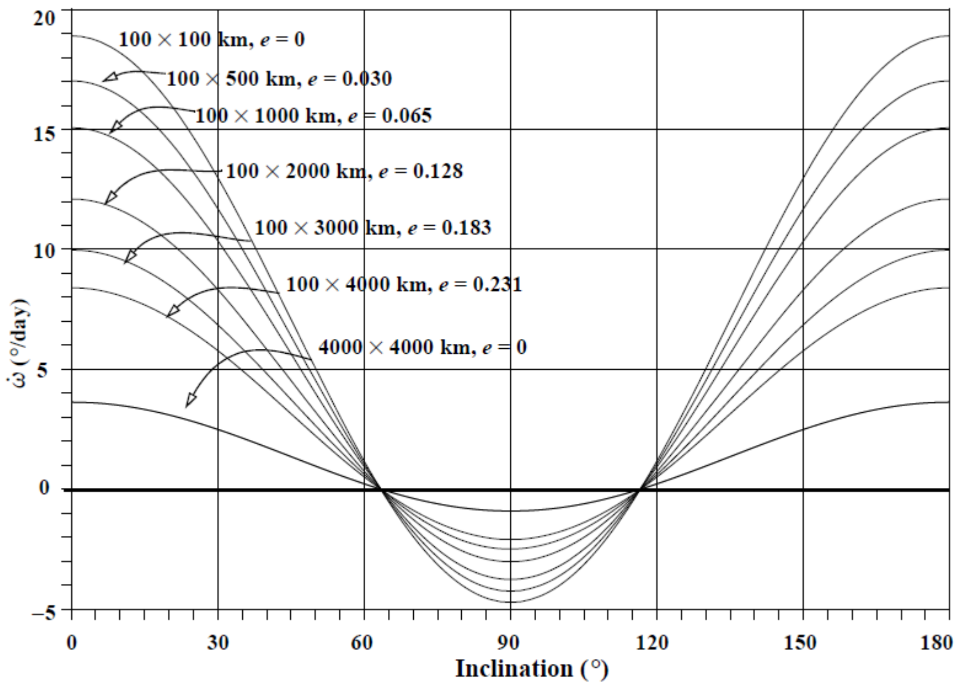

Figure 2.12: Variation of $\dot{\omega}_{J2}$ for different combinations of altitude and orbital inclination [23]

rotates in the direction of motion, whereas for inclinations greater than 63.4° and smaller than 116.6°, it rotates in the opposite direction.

2.5.2 Atmospheric Drag

In analogy with common practice in aeronautics, the acceleration due to atmospheric drag acting on the satellite can be expressed as:

$$\mathbf{f} = -\frac{1}{2}\rho\frac{A}{m}C_D|\mathbf{V}_r|\mathbf{V}_r \tag{2.56}$$

where ρ is the atmospheric density and $\mathbf{V}_r$ is the satellite's velocity relative to the Earth's atmosphere. C_D is the *drag coefficient* related to the reference surface A, m is the mass of the satellite. Atmospheric drag is a non-conservative force; its effect is a reduction in total mechanical energy, leading to a decrease in the semi-major axis and the orbital period. As the semi-major axis decreases, the effect of atmospheric drag becomes stronger because ρ increases. In the long run, the satellite tends to fall toward the Earth. This phenomenon is known as *orbital decay*, and it is crucial for determining the mission's lifespan.

The effect of atmospheric drag can be approximated as an impulsive, negative velocity increment occurring at perigee

$$m\frac{dv_r}{dt} = -\frac{1}{2}\rho A C_d V_r^2 \tag{2.57}$$

if the relative velocity is assumed approximately equal to the orbital velocity:

$$m\frac{dV}{dt} = -\frac{1}{2}\rho A C_d V^2 \tag{2.58}$$

differentiating the total mechanical energy equation leads to:

$$\dot{a} = \frac{2a^2}{\mu} V\dot{V} \tag{2.59}$$

substituting Equation (2.58) in to Equation (2.59) leads to:

$$\dot{a} = -\sqrt{\mu a}\frac{\rho A C_D}{m} \tag{2.60}$$

The term AC_D/m is also known as *ballistic coefficient* and it is used as a measure of the ability of a body to overcome air resistance in flight. A high ballistic coefficient indicates a high capability to 'penetrate' the atmosphere and results in a low negative acceleration due to drag.

2.5.3 Third-body Perturbations

The presence of other celestial bodies, as the Sun and the Moon, lead to other perturbing forces that affect satellites orbits due to their gravitational pull. A result of the N-body problem is the equation of perturbing potential, which expresses the gravitational perturbations exerted by multiple bodies j on the motion of body i relative to a non-rotating reference frame fixed at body k:

$$R = -G \sum_{j \neq k,i} m_j \left(\frac{1}{r_{ij}} - \frac{\mathbf{r_i} \cdot \mathbf{r_j}}{r_j^3} \right) \tag{2.61}$$

where $\mathbf{r_i}$ and $\mathbf{r_j}$ are the positions vectors form body k to body i and form body k to body j respectively. If body k is the Earth and body j is a single perturbing body (e.g. the Moon), then the perturbing acceleration of the satellite caused by the gravitational attraction between the satellite and the perturbing body can be written as:

$$\mathbf{f} = -\nabla \left[-\mu_j \left(\frac{1}{r_{ij}} - \frac{x_i x_j + y_i y_j + z_i z_j}{r^3} \right) \right] \tag{2.62}$$

where r_{ij} is

$$r_{ij} = (x_j - x_i)^2 + (y_j - y_i)^2 + (z_j - z_i)^2 \tag{2.63}$$

The perturbing acceleration can be decomposed as:

$$
\begin{aligned}
f_x &= \mu_j \left(\frac{x_j - x_i}{r_{ij}^3} - \frac{x_j}{r_j^3} \right) \\
f_y &= \mu_j \left(\frac{y_j - y_i}{r_{ij}^3} - \frac{y_j}{r_j^3} \right) \\
f_z &= \mu_j \left(\frac{z_j - z_i}{r_{ij}^3} - \frac{z_j}{r_j^3} \right)
\end{aligned}
\tag{2.64}
$$

If the positions of the satellite and the disturbing body are known (with respect to the non-rotating reference frame) then the acceleration components can be computed. The ratio between the magnitude of the perturbing acceleration and the magnitude of the acceleration due to the gravitational pull of the Erath can be expressed as:

$$
\left(\frac{f_d}{f_E} \right)_{max} = 2 \frac{m_d}{m_E} \left(\frac{r_i}{r_d} \right)^3 \tag{2.65}
$$

where m_d and m_E are the mass of the perturbing body and the mass of the Earth. The perturbing acceleration increases with increasing orbital altitude of the satellite, causing the attraction of the perturbing body to become the most important perturbing force.

2.5.4 Solar Radiation Pressure

The solar *irradiance* is known as the power per unit of area received from the Sun in the form of electromagnetic radiation in the wavelength range of the entire electromagnetic spectrum. The mean solar irradiance observed at a distance of 1 AU, measured on a surface perpendicular to the rays is $I_s = 1361\ W/m^2$, also known as *solar constant.* According to Maxwell's theory of electromagnetism, an electromagnetic wave carries momentum, which will be transferred to an opaque surface it strikes. The solar pressure is defined as the radiation pressure on the effective surface and can be computed as:

$$
p_s = \frac{I_s}{c} = 4.5 \cdot 10^{-6}\ Pa \tag{2.66}
$$

where c is the speed of light. An Earth satellite, in general, is exposed to a radiation force produced by direct sunlight, sunlight reflected by the Earth (*albedo radiation*), and thermal *infrared radiation* emitted by the Earth. The force an momentum generated by radiation pressure are generally too small to be noticed when other perturbation forces are acting on the satellite. The total force produced by the solar pressure upon a spacecraft can be expressed as:

$$F_s = K \cdot A \cdot p_s \tag{2.67}$$

where K is a coefficient which characterizes the interaction of the photons with the spacecraft surface. In general this perturbation can produce change in all orbital elements.

2.5.5 Special and General Perturbations Methods

As mentioned, the study of perturbations requires specific techniques. There are two main categories, referred to as Special Perturbations and General perturbations. When the motion of a satellite is described relative to a non-rotating geocentric reference frame and perturbing forces are taken into account, the equation of motion can be written as

$$\frac{d^2\mathbf{r}}{dt^2} + \frac{\mu}{r^3}\mathbf{r} = -\nabla R + \mathbf{f} \tag{2.68}$$

where R is the *perturbing potential*, that describe all perturbing forces that can be expressed by a potential function, and $\mathbf{f}$ represents all other perturbing forces that cannot be written as the gradient of a scalar function of the satellite's coordinates.

Equation (2.68) cannot be solved analytically and required numerical methods (special perturbations methods) or approximative analytical methods (general perturbations methods).

2.5.5.1 Cowell's Method

The Cowell's Method is the simplest method used for the computation of perturbed satellite orbits. In this method the equation of motion is written in the form

$$\frac{d^2\mathbf{r}}{dt^2} = \mathbf{f_t} \tag{2.69}$$

where $\mathbf{f_t}$ is

$$\mathbf{f_t} = -\frac{\mu}{r^3}\mathbf{r} - \nabla R + \mathbf{f} \tag{2.70}$$

The equation (2.69) is numerically integrated to compute the satellite trajectory. However Cowell's Method required small integration steps in the integration process, this implies long computation times and a steadily growing numerical integration error.

2.5.5.2 Encke's Method

The Encke's method makes use of a reference orbit, known as *osculating orbit*, and the deviations from the reference orbit are numerically integrated. For example, a reference orbit can be a Keplerian one. The equation of motion integrated in this method is

$$\frac{d^2\Delta\mathbf{r}}{dt^2} = \mu\left(\frac{\boldsymbol{\rho}}{\rho^3} - \frac{\mathbf{r}}{r^3}\right) - \nabla R + \mathbf{f} \tag{2.71}$$

where $\boldsymbol{\rho}$ is the position vector of the satellite if the satellite would follow the unperturbed reference orbit, and $\mathbf{r}$ is the actual position vector. The $\Delta\mathbf{r}$ is defined as

$$\Delta\mathbf{r} = \mathbf{r} - \boldsymbol{\rho} \tag{2.72}$$

and represent the deviation of the actual trajectory from the osculating one. As in Encke's method only the perturbing accelerations are integrated, the integration step can be chosen larger than in Cowell's method, but it required more computing time. If $\Delta\mathbf{r}$ become too large, the reference orbit can be rectified, such that $\Delta\mathbf{r} = 0$.

2.5.5.3 Variation of Parameters

Most analytical solutions used in general perturbation methods rely on a process known as *variation of parameters* (VOP). In this method, the motion is described using classical orbital elements, which are constant in Keplerian orbits but time-dependent in perturbed ones.

The concept is based on the premise that the constants of motion in the solution can be generalized to time-varying parameters. The VOP equations of motion form a system of first-order differential equations that describe the rate of change of the orbital elements. Two of the most well-known VOP formulations are the *Lagrange planetary equations of motion* and the *Gauss planetary equations of motion*. The latter is the one used in this work.

Gauss's planetary equations are developed in the $\{\hat{\mathbf{R}}, \hat{\mathbf{S}}, \hat{\mathbf{W}}\}$ reference frame, where $\hat{\mathbf{R}}$ identifies the direction of the radius vector, $\hat{\mathbf{S}}$ is perpendicular to $\hat{\mathbf{R}}$ within the orbital plane in the direction of the satellite's motion, and $\hat{\mathbf{W}}$ is normal to the orbital plane and oriented such that $\hat{\mathbf{R}}$, $\hat{\mathbf{S}}$, and $\hat{\mathbf{W}}$ form a right-handed set of axes. The perturbing force per unit mass, $\mathbf{f}$, can be decomposed as:

$$\mathbf{f} = f_R\hat{\mathbf{R}} + f_S\hat{\mathbf{S}} + f_W\hat{\mathbf{W}} \tag{2.73}$$

The derivation of the Gauss planetary equation is shown in [23]:

$$
\begin{aligned}
\frac{da}{dt} &= \frac{2}{n\sqrt{1-e^2}}\left[e\sin\nu f_R + \frac{p}{r}f_S\right] \\
\frac{de}{dt} &= \frac{\sqrt{1-e^2}}{na}\left[\sin\nu f_R + \left(\cos\nu + \frac{e+\cos\nu}{1+e\cos\nu}\right)f_S\right] \\
\frac{di}{dt} &= \frac{r\cos(\omega+\nu)}{na^2\sqrt{1-e^2}}f_W \\
\frac{d\Omega}{dt} &= \frac{r\sin\omega+\nu}{na^2\sqrt{1-e^2}\sin i}f_W \\
\frac{d\omega}{dt} &= \frac{\sqrt{1-e^2}}{nae}\left[-\cos\nu f_R + \sin\nu\left(1+\frac{r}{p}\right)f_S\right] - \frac{r\cot i\sin(\omega+\nu)}{h}f_w \\
\frac{dM_0}{dt} &= \frac{1}{na^2e}\left[(p\cos\nu - 2er)f_R - (p+r)\sin\nu f_S\right] - \frac{dn}{dt}(t-t_0)
\end{aligned}
\tag{2.74}
$$

It is important to note that these equations present some limitations. The eccentricity must be less than 1 due to the presence of $\sqrt{1-e^2}$, and they exhibit singularities for particular sets of orbital elements. For example, in the $\dot{\Omega}$ equation, $\sin i$ appears in the denominator, making the equation indeterminate when $i = 0$. A similar problem affects the $\dot{\omega}$ equation when e is small.

Chapter 3

Fundamental of Space Propulsion

This section provides a brief introduction to some fundamental concepts regarding space propulsion systems and orbital manoeuvres, with the aim of facilitating a full understanding of the optimization method discussed later in this work.

Space propulsion systems can be divided into three main categories: chemical rocket propulsion, nuclear rocket engines, and electric rocket propulsion. The most commonly used propulsion systems today are chemical propulsion and electric propulsion. In chemical propulsion, the energy converted to kinetic energy is stored in the propellants. When chemical propulsion is employed, the manoeuvres are typically considered impulsive. In contrast, an electric propulsion system derives its energy from an external source, the resulting trajectories are typically referred to as low-thrust trajectories.

For further information, see [2], [26], and [21].

3.1 Generalities of Space Propulsion

To evaluate the thrust of a rocket engine, an isolated system with mass m and velocity V is considered, with only the thrust force acting on it. After a time interval dt, the system expels a small particle of mass dm_p with velocity c, while its own velocity increases by dV, as shown in Figure (3.1). The momentum conservation equation for the system is given by:

$$mV = (V + dV)(m - dm) - dm_p(c - V) \tag{3.1}$$

Neglecting higher-order infinitesimal terms leads to:

$$mdV = dm_p c \quad \longrightarrow \quad m\frac{dV}{dt} = T = \dot{m}_p c \tag{3.2}$$

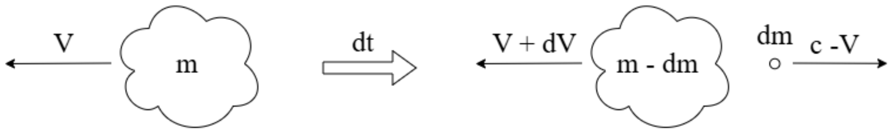

Figure 3.1: Isolated system of mass m before and after a time interval dt.

where T is the thrust force of the rocket engine, $\dot{m}_p$ is the propellant mass flow rate. Equation (3.2) is written under the assumption that the expelled mass dm does not interact with the propellant inside the spacecraft. If the momentum exchange through pressure forces between the ejected propellant and the propellant inside the spacecraft is considered, the thrust force can be expressed as:

$$T = \dot{m}_p u_e + A_e \left(p_e - p_0\right) \tag{3.3}$$

where u_e is the velocity of the exhausted gas, A_e is the exit area, p_e is the pressure at the exit surface, and p_0 is the external pressure. If $p_e = p_0$, then u_e coincides with c; in space propulsion, p_0 is typically considered to be zero. Since the values of u_e and p_e are not always available, and only thrust and propellant mass flow rate are relevant for trajectory optimization, the *effective exhaust velocity* c is introduced:

$$c \stackrel{\text{def}}{=} \frac{T}{\dot{m}_p} = u_e + \frac{A_e \left(p_e - p_0\right)}{\dot{m}_p} \tag{3.4}$$

Thus, the thrust force can be expressed as:

$$T = \dot{m}_p c \tag{3.5}$$

Dividing Equation (3.5) by m, the thrust acceleration is obtained:

$$\frac{T}{m} = \frac{\dot{m}_p c}{m} \tag{3.6}$$

Since $\dot{m}_p = -\frac{dm}{dt}$, Equation (3.6) can be rewritten as:

$$\frac{T}{m} = -\frac{dm}{dt}\frac{c}{m} \tag{3.7}$$

This equation must be integrated from an initial time t_0 to a final time t_f:

$$\int_{t_0}^{t_f} \frac{T}{m}\, dt = \int_{m_0}^{m_f} -c\frac{dm}{m} \tag{3.8}$$

which leads to:

$$\Delta V = c \ln \frac{m_0}{m_f} \tag{3.9}$$

Equation (3.9) is known as the *Tsiolkovsky equation* or *rocket equation.* Knowing the required ΔV to change orbit, it is possible to compute the amount of propellant necessary to complete the maneuver. Conversely, knowing the available propellant mass, it is possible to compute the ΔV that the propulsion system can achieve. For a given mission, the characteristic velocity ΔV is approximately constant. In Table (3.1), some characteristic velocities for different missions are reported.

Two useful quantities used to describe the performance of propulsion systems are the *total impulse* I_t and the *specific impulse* I_{sp}. The total impulse is found by integrating the thrust force over the time of application:

$$I_t = \int_{t_0}^{t_f} T\,dt \tag{3.10}$$

If the thrust force is assumed to be constant, I_t can be computed as:

$$I_t = T\Delta t \tag{3.11}$$

with $\Delta t = t_f - t_0$. In general, for a given spacecraft mass, the total impulse can be approximated as:

$$I_t \approx m_{avg}\Delta V \tag{3.12}$$

and it depends only on the mission. I_t is proportional to the total energy released by all the propellant utilized by the propulsion system. The specific impulse is defined as:

$$I_{sp} = \frac{I_t}{m_p g_0} \tag{3.13}$$

Mission	ΔV $[km/s]$
LEO Insertion	10
1 year station keeping	0.5
LEO-GEO (impulsive)	3.5
LEO-GEO (spiral)	6
Earth escape (impulsive)	3.2
Earth escape (spiral)	8
Earth-Mars (impulsive)	5.5
Earth-Mars (spiral)	6
Earth-Jupiter (spiral)	16.7
Earth-Alpha Centauri	3000

Table 3.1: Typical characteristic velocities for different missions [4]

If T and $\dot{m}_p$ are assumed constant, Equation (3.13) simplifies to:

$$I_{sp} = \frac{T}{\dot{m}_p g_0} = \frac{c}{g_0} \tag{3.14}$$

The specific impulse represents the thrust per unit propellant weight flow rate. It is an important figure of merit of the performance of any rocket propulsion system, as it represents the 'cost' of thrust in terms of propellant usage. In fact, we can express m_p as:

$$m_p = \frac{m_{avg} \Delta V}{I_{sp} g_0} \tag{3.15}$$

The mass of propellant is inversely proportional to the specific impulse: the higher the I_{sp}, the less m_p is required to achieve the same ΔV. Note that I_{sp} and c are related only by the constant g_0, so they essentially represent the same concept.

3.2 Impulsive Manoeuvres

Whit impulsive manoeuvres is intended a brief firings of onboard rocket motors that change the magnitude and the direction of the velocity vectors instantaneously. The duration of the impulse Δt is assumed tending to 0, during the impulsive manoeuvre $T \to \infty$ and the position of the spacecraft is considered to be fixed ($\mathbf{r}$=cost) while the velocity changes. The assumption of impulsive manoeuvre is generally used when chemical propulsion is used.

3.2.1 Transfer Between Coplanar Circular Orbits

Consider two coplanar circular orbits with radii r_1 and r_2, where $r_2 > r_1$, and a transfer orbit that moves a satellite from orbit r_1 to orbit r_2, as shown in Figure (3.2). The transfer orbit must intersect (or be tangent to) both circular orbits. This condition is satisfied if

$$\begin{cases} r_{Pt} = \frac{p_t}{1+e_t} \leq r_1 \\ r_{At} = \frac{p_t}{1-e_t} \geq r_2 \end{cases} \longrightarrow \begin{cases} e_t \geq \frac{p_t}{r_1} - 1 \\ e_t \geq 1 - \frac{p_t}{r_2} \end{cases} \tag{3.16}$$

where r_{Pt} and r_{At} are the perigee and apogee of the transfer orbit, respectively. By representing this equations in the e_t-p_t/r_1 plane, the feasible region can be identified. As shown in Figure (3.3), hyperbolic, parabolic, and elliptical transfer orbits are possible. The transfer manoeuvre presented is a two-impulse manoeuvre: the first impulse is required to inject in to the transfer orbit while the second one is needed to circularize the orbit and finalize the transfer. The

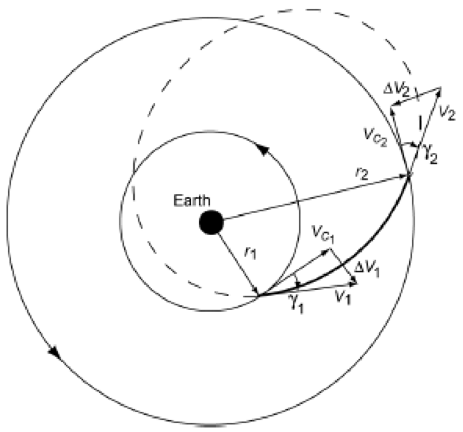

Figure 3.2: Geometry of a transfer orbit between two coplanar circular orbits [26].

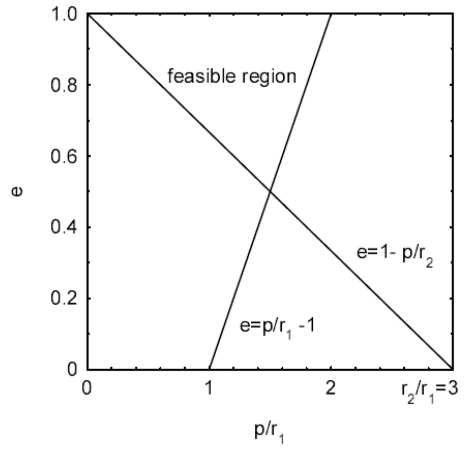

Figure 3.3: Region of possible transfer orbits between two coplanar circular orbits [4].

total ΔV can be computed as:

$$\Delta V = |\Delta V_1| + |\Delta V_2| \tag{3.17}$$

where $|\Delta V_1|$ and $|\Delta V_2|$ can be computed using the cosine rule, knowing the flight path angle at the two intersection points:

$$\begin{aligned} |\Delta V_1| &= \sqrt{V_1^2 + V_{c1}^2 - 2V_1 V_{c1}\cos\gamma_1} \\ |\Delta V_2| &= \sqrt{V_2^2 + V_{c2}^2 - 2V_2 V_{c2}\cos\gamma_2} \end{aligned} \tag{3.18}$$

where V_{c1} and V_{c2} are the circular velocities on orbits r_1 and r_2:

$$V_1 = \sqrt{\frac{\mu}{r_1}} \;; \qquad V_2 = \sqrt{\frac{\mu}{r_2}} \tag{3.19}$$

V_1 and V_2 are the velocity on the transfer orbit after the first impulse and the velocity on the transfer orbit before the second impulse respectively. V_1 and V_2 can be computed from the total mechanical energy equation:

$$V_1^2 = 2\left(\frac{\mu}{r_1} + \epsilon_t\right) \;; \qquad V_2^2 = 2\left(\frac{\mu}{r_2} + \epsilon_t\right) \tag{3.20}$$

The flight path angle can be evaluated using Equation (2.27):

$$\cos\gamma_1 = \frac{h_t}{r_1 V_1} \;; \qquad \cos\gamma_2 = \frac{h_t}{r_2 V_2} \tag{3.21}$$

When $r_{Pt} = r_1$ and $r_{At} = r_2$, we have $\gamma_1 = \gamma_2 = 0$, meaning that V_1 is parallel to V_{c1} and V_2 is parallel to V_{c2}. This particular transfer orbit is known as the

Hohmann transfer, which is the orbital maneuver requiring the minimum ΔV to transfer from r_1 to r_2. In this case, the total mechanical energy ϵ_t of the transfer orbit can be written as:

$$\epsilon_t = -\frac{\mu}{2a_H} = -\frac{\mu}{r_1 + r_2} \tag{3.22}$$

Substituting equation (3.22) into equation (3.20) leads to:

$$V_1^2 = V_{c1}^2 \frac{2r_2}{r_1 + r_2} \; ; \qquad V_2^2 = V_{c2}^2 \frac{2r_1}{r_1 + r_2} \tag{3.23}$$

and substituting into equation (3.18) yields:

$$\begin{aligned} \Delta V_1 &= V_1 - V_{c1} = V_{c1} \left(\sqrt{\tfrac{2r_2}{r_1+r_2}} - 1 \right) \\ \Delta V_2 &= V_{c2} - V_2 = V_{c2} \left(1 - \sqrt{\tfrac{2r_1}{r_1+r_2}} \right) \end{aligned} \tag{3.24}$$

While the Hohmann transfer is the most ΔV-efficient transfer between two coplanar circular orbits, it is also the one requiring the longest transfer time:

$$T_H = \pi \sqrt{\frac{a_H^3}{\mu}} \tag{3.25}$$

3.2.2 Transfer between Orbits in different Orbital planes

When only the variation of the inclination of the orbital plane is intended, this manoeuvre is referred to as a simple plane change. Assuming a plane change from an inclined orbit to an equatorial one, as shown in Figure (3.4), it is immediate from the velocity triangle to verify that:

$$\Delta V = 2V \sin \frac{\theta}{2} \tag{3.26}$$

The ΔV is applied perpendicular to the orbital plane and is proportional to V, so it is optimal to perform orbital plane change manoeuvre when the velocity is low, for example, at the apogee. Note that a pure plane change is possible if the manoeuvrer point is one of the nodes. If the ΔV is applied at other points, a change in both inclination and RAAN is obtained, and the change in i is less efficient in terms of ΔV. A change in semi-major axis and inclination can be combined in a single manoeuvre, applying the vector sum of the velocities V_1 and V_2. Using the cosine rule lead to:

$$\Delta V_{comb} = \sqrt{V_1^2 + V_2^2 - 2V_1 V_2 \cos \Delta i} \tag{3.27}$$

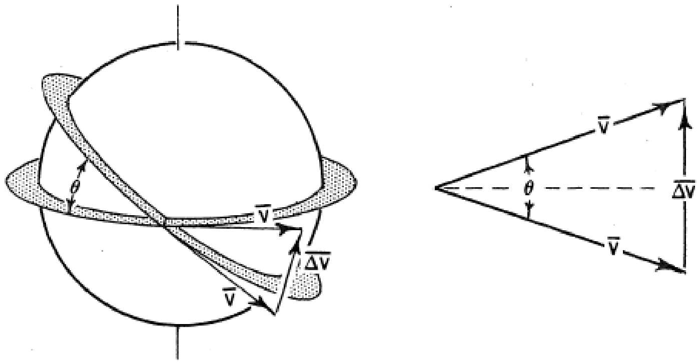

Figure 3.4: Simple plane change [2].

where V_1 and V_2 are the velocities on the departure and arrival orbits, respectively.

3.3 Chemical Propulsion

In a chemical propulsion system, two propellants are generally used: a fuel and an oxidizer. These propellants are mixed in a combustion chamber with an appropriate *mixture ratio*, which affects the performance of the propulsion system, and then ignited. The hot gas produced is subsequently expanded through a nozzle.

It is evident that the chemical energy stored in the propellants is first converted into thermal energy through combustion and then into kinetic energy through expansion. This represents a fundamental limitation of chemical propulsion: the specific impulse I_{sp} is constrained by the intrinsic energy of the chemical reaction.

The chemical power stored in the propellants can be expressed as:

$$P_T = \dot{m}_p E_{ch} \tag{3.28}$$

where E_{ch} is the energy per unit mass released by the chemical reaction. The kinetic power can be expressed as:

$$P_k = \frac{1}{2}\dot{m}_p c^2 = \frac{1}{2}Tc \tag{3.29}$$

Since chemical power is converted into kinetic power, an efficiency coefficient η must be introduced in a real system:

$$P_T\,\eta = P_k \qquad \longrightarrow \qquad \dot{m}_p E_{ch}\eta = \frac{1}{2}\dot{m}_p c^2 \tag{3.30}$$

Propellants	State	Specific Impulses [s]
LOX / LH2	L	500-450
LOX / RP-1	L	300-330
LOX / CH4	L	280-310
NTO / Hydrazine	L	280-310
NTO / MMH	L	280-310
NC / NG	S	200-250
AP / PBAN / AI	S	260-290

Table 3.2: Typical value of specific impulse for some oxidizer-fuel pair [4]

From this equation, the exhaust velocity c can be expressed as:

$$c = \sqrt{2\eta E_{ch}} \tag{3.31}$$

Equation (3.31) clearly shows that the specific impulse ($I_{sp} = c/g_0$) depends on the choice of propellants. Table (3.2) presents typical values of specific impulse for different oxidizer-fuel pairs.

One of the main advantages of chemical propulsion systems is that an external power source is not required, as the energy is directly stored in the propellants. Furthermore, since the thrust force is directly related to the propellant mass flow rate, both low and high thrust levels can be achieved.

3.4 Electric Propulsion

Unlike a chemical propulsion system, where the propellants serve as both the power source and the exhaust medium, an electric propulsion system has a separate power source and power conversion unit to impart the propulsive energy to the propellant. An electric propulsion system is characterized by very low thrust but a very high exhaust velocity, allowing the thrust to be sustained for long periods while minimizing propellant consumption.
Electric propulsion systems can be grouped into three categories:

- **Electrothermal propulsion system**: This type of system includes *resistojets* and *arcjets*. The propellant is heated electrically, and the hot gas generated is thermodynamically expanded and accelerated through an exhaust nozzle. In a resistojet, the heating element is a high-resistance metal part that heats the propellant flowing over it. Arcjets heat the propellant gas flow directly through an electric arc discharge. The I_{sp} for an electrothermal propulsion system can vary from 500 s to 1000 s.

- **Electrostatic propulsion**: This type of system includes the *Kaufman thruster* and the *Field Emission Electric Propulsion* (FEEP) thruster.

In a Kaufman thruster, the propellant atoms are ionized by electron bombardment, and then the ions are accelerated through an electric field. The energetic electrons are provided by a hot cathode filament and accelerated in the electrical field of the cathode fall to the anode. The ion beam needs to be neutralized by injecting a stream of electrons into the exhaust beam to avoid charge accumulation on the spacecraft. The I_{sp} for an electrostatic propulsion system can vary from 2000 s to 4000 s.

- **Electromagnetic propulsion**: In this type of system, a highly-ionized propellant plasma is generated, and the ions are accelerated by the interaction of electrical and magnetic fields. After acceleration, the plasma beam is neutralized by picking up electrons. *Hall thrusters* use the Hall effect to set up an electrostatic field, which accelerates the propellant ions, while *Magnetoplasmadynamic thrusters* use an electric arc discharge, similar to arcjets. The I_{sp} for Hall thrusters can vary from 1500 s to 2500 s.

In an electric propulsion system, the energy is provided by an external source. The relationship between the electric power and the kinetic power can be expressed as:

$$P_e\,\eta = \frac{1}{2}\dot{m}_p c^2 = \frac{1}{2}Tc \tag{3.32}$$

Solving for c:

$$c = \sqrt{\frac{2\eta P_e}{\dot{m}_p}} = \frac{2\eta P_e}{T} \tag{3.33}$$

The specific impulse depends on both the electric power and the propellant mass flow rate, and unlike in chemical propulsion, it is not fundamentally limited. However, achieving high thrust values requires high values of P_e, which are generally not feasible or would require excessively heavy power generators.

Another key difference from chemical propulsion systems, where a higher I_{sp} is generally preferable,is that in electric propulsion, each mission has an optimal I_{sp} value. As a result, selecting the appropriate thruster is fundamental for mission design.

For further details on electric propulsion systems, refer to [13].

3.4.1 Limits of Electric Propulsion

The necessity of an external power source is also a limitation of an electric propulsion system. The total spacecraft mass can be expressed as:

$$m = m_u + m_g + m_p \tag{3.34}$$

where m_u is the payload mass, m_p is the propellant mass, and m_g is the generator mass. The acceleration due to the applied thrust is given by:

$$a = \frac{T}{m} \tag{3.35}$$

It is evident that a is lower than the acceleration the spacecraft would experience if its mass were composed only of the generator:

$$a < \frac{T}{m_g} \tag{3.36}$$

The generator mass can be related to the electric power it provides as:

$$m_g = \alpha P_e \tag{3.37}$$

where α represents the "technology level" of the power source: a lower α corresponds to a lighter generator, indicating better technology. Substituting this expression into Equation (3.36) yields:

$$a < \frac{T}{\alpha P_e} \tag{3.38}$$

and, incorporating Equation (3.32), results in:

$$a < \frac{\eta}{\alpha}\frac{2}{c} \tag{3.39}$$

The acceleration that an electric propulsion system can sustain is constrained by the right-hand side of the inequality. It is easy to verify that for $\eta = 0.5$, $\alpha = 1\,\text{kg/kW}$, and $c = 10\,\text{km/s}$ (which are very optimistic values), the acceleration is limited to:

$$a < 0.1\,\text{km/s}^2 \tag{3.40}$$

which is less than one hundredth of Earth's gravitational acceleration g_0. This implies that the effect of thrust on the trajectory is small, and significant changes in orbital parameters can only be achieved over many revolutions.

Indeed, in the case of *electric propulsion*, the considered trajectories are low-thrust trajectories, where both the thrust direction and magnitude can be continuously varied. These types of trajectories are the subject of the optimization study in this work.

Chapter 4

Mathematical Models for Trajectory Optimization

The term *optimal control problem* refers to a mathematical problem in which the objective is to determine the inputs to a dynamic system that maximize or minimize a specified performance index while satisfying any constraints on the system's motion. More specifically, when the inputs to the system are static parameters and the goal is to determine the values of these parameters along with the trajectory that optimizes a given performance index, the problem is referred to as *trajectory optimization*. Instead, if the inputs to the system are functions and the objective is to determine both the optimal input function and trajectory, the problem is referred to as *optimal control*.

Numerical methods for solving optimal control problems are classified into two major categories: *indirect methods* and *direct methods*. In the former, the calculus of variations is used to derive optimality conditions, leading to a *two-point* (or, in the general case, a *multiple-point*) *boundary-value problem*, which must be solved to determine candidate optimal trajectories, known as *extremals*. In contrast, a direct method reformulates the optimal control problem as a *non-linear optimization problem* or *non-linear programming problem*, which is then solved using numerical optimization techniques. To summarize, in an indirect method, the optimal solution is obtained by solving a system of differential equations that satisfy the endpoint conditions. On the other hand, in a direct method, the optimal solution is found by converting an infinite-dimensional optimization problem into a finite-dimensional one.

At the core of any optimization method, three fundamental components can be identified: a method for solving differential equations, a method for solving systems of non-linear algebraic equations, and a method for solving non-linear optimization problems. In an indirect method, the numerical solution of differential equations is combined with the numerical solution of non-linear equation systems, whereas in a direct method, the numerical solution of differential equations is combined whit non-linear optimization.

In this work, two approaches are considered: the indirect method and an *approximate method.* The latter introduces simplifications that allow for the integration of the differential equations, leading to an analytical solution.

For further details see [18] or [14].

4.1 Optimal Control Problem Formulation

A dynamic system can be described by a set of non-linear differential equations that govern the time evolution of a *state vector*:

$$\dot{\mathbf{x}} = \mathbf{f}[\mathbf{x}(t), \mathbf{u}(t), t; \mathbf{p}], \quad t_0 \leq t \leq t_f \tag{4.1}$$

where $\mathbf{x}(t)$ is the state vector, $\mathbf{u}(t)$ is the control vector and $\mathbf{p}$ is the vector of static parameters:

$$\mathbf{x}(t) = \begin{bmatrix} x_1(t) \\ \vdots \\ x_n(t) \end{bmatrix} \quad ; \quad \mathbf{u}(t) = \begin{bmatrix} u_1(t) \\ \vdots \\ u_m(t) \end{bmatrix} \quad ; \quad \mathbf{p} = \begin{bmatrix} p_1 \\ \vdots \\ p_q \end{bmatrix} \quad ; \tag{4.2}$$

$\mathbf{x}(t_0)$ is given and some components of $\mathbf{x}(t_f)$ are specified. The final time t_f can be either fixed or free. The optimal control problem consists of finding $\mathbf{u}(t)$ that minimizes (or maximizes) a given performance index:

$$J = \varphi[\mathbf{x}(t_f), t_f; \mathbf{p}] + \int_{t_0}^{t_f} \Phi[\mathbf{x}(t), \mathbf{u}(t), t, ; \mathbf{p}]\, dt \tag{4.3}$$

Equation (4.3) represents the "quality" of the trajectory, where $\Phi[\mathbf{x}(t), \mathbf{u}(t), t; \mathbf{p}]$ can be interpreted as the rate of cost associated with exerting $\mathbf{u}$ in state $\mathbf{x}$, and $\varphi[\mathbf{x}(t_f), t_f; \mathbf{p}]$ represents the cost associated with reaching the final state $\mathbf{x}(t_f)$. *Path constraint* can be included as follow:

$$C_{min} \leq C[\mathbf{x}(t), \mathbf{u}(t), t; \mathbf{p}] \leq C_{max} \tag{4.4}$$

and the boundary conditions are included as follow:

$$S_{min} \leq S[\mathbf{x}(t_0), t_0, \mathbf{x}(t_f), t_f; \mathbf{p}] \leq S_{max} \tag{4.5}$$

An optimal control problem can be divided into multiple phases $p \in [1, \ldots, P]$, which are interconnected. In a multi-phase optimal control problem, the total cost to be optimized is given by:

$$J = \sum_{k=1}^{P} J^{(k)} \tag{4.6}$$

where $J^{(k)}$ represents the cost associated with each phase.

4.2 The Indirect Method

As previously mentioned, the *calculus of variations* is used to determine the first-order optimality conditions for the optimal control problem. The calculus of variations is the field concerned with determining a function that optimizes a *function of a function*, also known as a *functional*. Applying the calculus of variations to the optimal control problem described by Equations (4.1), (4.3), (4.4), and (4.5), leads to the necessary conditions for an extremal trajectory. To derive these conditions, it is necessary to introduce the *Hamiltonian*, defined as:

$$H = \boldsymbol{\lambda}^T \mathbf{f} \tag{4.7}$$

where $\boldsymbol{\lambda}$ are the time-varying *Lagrange multipliers*, also known as *adjoint variables* (or *costate* variables). The *Pontryagin's maximum principle* states that the optimal trajectory $\mathbf{x}^*$, reached with the optimal control $\mathbf{u}^*$ and the corresponding Lagrange multipliers $\boldsymbol{\lambda}^*$, must maximize the Hamiltonian H, such that:

$$H(\mathbf{x}^*(t), \mathbf{u}^*(t), \boldsymbol{\lambda}^*(t), t) \geq H(\mathbf{x}(t), \mathbf{u}(t), \boldsymbol{\lambda}(t), t), \quad t_0 \leq t \leq t_f \tag{4.8}$$

This can be achieved if the adjoint variables satisfy the *adjoint equations*:

$$\frac{d\boldsymbol{\lambda}}{dt} = -\left(\frac{\partial H}{\partial \mathbf{x}}\right)^T \tag{4.9}$$

and the algebraic equations for the control satisfy:

$$\left(\frac{\partial H}{\partial \mathbf{u}}\right)^T = 0 \tag{4.10}$$

To summarize, the optimal control problem can be reformulated as a two-point boundary value problem:

$$\begin{cases} \dfrac{d\mathbf{x}}{dt} = \mathbf{f}[\mathbf{x}(t), \mathbf{u}(t), t; \mathbf{p}] \\ \dfrac{d\boldsymbol{\lambda}}{dt} = -\left(\dfrac{\partial H}{\partial \mathbf{x}}\right)^T \\ \left(\dfrac{\partial H}{\partial \mathbf{u}}\right)^T = 0 \end{cases} \tag{4.11}$$

To find a solution to this problem, the initial values of the unknown variables must be determined, and integrating the differential equations leads to the optimal trajectory of $\mathbf{x}$. This can be achieved using a *shooting method*.

A shooting method consists of numerically integrating the differential equations from t_0 to t_f with a set of *trial* initial values for the unknown variables. Once t_f is reached, the obtained terminal conditions are compared with the known terminal conditions. If they do not match, the trial initial values are adjusted. This process is iterated until the difference between the integrated terminal conditions and the required terminal conditions is below a specified threshold.

4.3 Edelbaum Dynamic Model

In this work, the target and chaser orbits are assumed to be nearly circular, so the dynamics can be described using *Edelbaum's dynamical model*, which assumes constant circular orbits. The dynamic model is derived from Gauss's equations, considering several assumptions: the orbit is nearly circular with low inclination, and the thrust is very low (smaller than the gravitational force). These assumptions lead to the following simplifications:

$$\begin{gathered} a \approx p \approx r; \;\; V^2 \approx \mu/r; \;\; e \approx 0; \;\; \sin i \approx i; \;\; \cos i \simeq 1; \;\; E \approx \nu \approx M \\ f_V = f_T \ll \mu/r; \quad f_R \ll \mu/r; \quad f_W \ll \mu/r; \quad \theta = \omega + \nu + \Omega \end{gathered} \tag{4.12}$$

The Gauss planetary equations (Equation (2.74)) then become:

$$
\begin{aligned}
&V\frac{\dot{a}}{a} = 2f_T \\
&V\dot{e} = 2\cos\nu f_T + \sin\nu f_R \\
&V\dot{i} = \cos(\omega+\nu) f_W \\
&iV\dot{\Omega} = \sin(\omega+\nu) f_W \\
&V\dot{\omega} = -V\dot{\Omega} + (2\sin\nu f_T - \cos\nu f_R)/e \\
&\dot{\theta} = n = \sqrt{\tfrac{\mu}{a^3}}
\end{aligned}
\tag{4.13}
$$

Next, the angle α is introduced, defined as the in-plane angle between the thrust vector and the velocity, and the angle β, defined as the out-of-plane angle between the thrust vector and the velocity. The three acceleration components can then be expressed as:

$$f_T = f\cos\alpha\cos\beta; \quad f_R = f\sin\alpha\cos\beta; \quad f_W = f\sin\beta \tag{4.14}$$

where $f = T/m$ is the magnitude of the acceleration. Substituting Equation (4.14) into Equations (4.13), yields:

$$\dot{a} = \frac{2af}{V}\cos\alpha\cos\beta \tag{4.15}$$

$$\dot{e} = \frac{2f}{V}\cos\nu\cos\alpha\cos\beta + \frac{f}{V}\sin\nu\sin\alpha\cos\beta \tag{4.16}$$

$$\dot{i} = \frac{f}{V}\cos(\omega+\nu)\sin\beta \tag{4.17}$$

$$\dot{\Omega} = \frac{f}{iV}\sin(\omega+\nu)\sin\beta \tag{4.18}$$

$$\dot{\omega} = -\dot{\Omega} + \frac{f}{eV}(2\sin\nu\cos\alpha\cos\beta - \cos\nu\sin\alpha\cos\beta) \tag{4.19}$$

4.3.1 One Revolution Transfer

To analyse a one-revolution transfer, Equations (4.15)-(4.17) are integrated over one revolution. A variable change $dt = \sqrt{a^3/\mu}\, d\nu$ is performed, and the integration limits are set from 0 to 2π. This leads to:

$$\Delta a = \frac{2af}{V}\int_0^{2\pi}\cos\alpha\cos\beta\, d\nu \tag{4.20}$$

$$\Delta e = \frac{f}{V}\int_0^{2\pi}(2\cos\nu\cos\alpha + \sin\nu\sin\alpha)\cos\beta\, d\nu \tag{4.21}$$

$$\Delta i = \frac{f}{V}\int_0^{2\pi}\cos(\omega+\nu)\sin\beta\, d\nu \tag{4.22}$$

Note that the equations for $\dot{\Omega}$ and $\dot{\omega}$ are neglected in this case. The optimal values of α and β can be determined based on the desired changes in orbital parameters:

- A maximum increase in a requires $\beta = 0$ (since $\Delta i = 0$) and $\alpha = 0$ (since $\Delta e = 0$).
- A maximum increase in e requires $\beta = 0$ (since $\Delta i = 0$) and $\tan\alpha = \frac{\tan\nu}{2}$.
- A maximum increase in i requires $\alpha = 0$ (since $\Delta e = 0$) and $\beta = \frac{\pi}{2}$ if $\cos(\omega + \nu) > 0$, or $\beta = -\frac{\pi}{2}$ if $\cos(\omega + \nu) < 0$.

When both Δa and Δi must be maximized, applying the optimal control theory to the equations (4.15) and (4.17) leads to:

$$\tan\beta = K\cos(\omega + \nu) \tag{4.23}$$

where K is a constant. The angle α must be set to 0, as it is optimal for maximizing changes in a and does not influence changes in i. From Equation (4.23), the expressions for $\cos\beta$ and $\sin\beta$ can be derived:

$$\cos\beta = \frac{1}{\sqrt{1 + (K\cos(\omega + \nu))^2}}\ ; \qquad \sin\beta = \frac{K\cos(\omega + \nu)}{\sqrt{1 + (K\cos(\omega + \nu))^2}} \tag{4.24}$$

These expressions must be substituted into Equations (4.20) and (4.22) and integrated. This results in elliptic integrals, which do not have an analytical solution and must be evaluated numerically. Additionally, the practical implementation of this control law may be complex. Therefore, the control law for β can be approximated using a piecewise constant function:

$$\beta = \begin{cases} \overline{\beta}, & \cos(\omega + \nu) \geq 0 \\ -\overline{\beta}, & \cos(\omega + \nu) < 0 \end{cases} \tag{4.25}$$

Substituting this expression into Equations (4.20) and (4.22) and integrating over one revolution yields:

$$\frac{\Delta a}{a} = \frac{4\pi f \cos\overline{\beta}}{nV}\ ; \qquad \Delta i = \frac{4\pi \sin\overline{\beta}}{nV} \tag{4.26}$$

The difference between the optimal control law and the approximate control law is negligible, as shown in Figure (4.1).

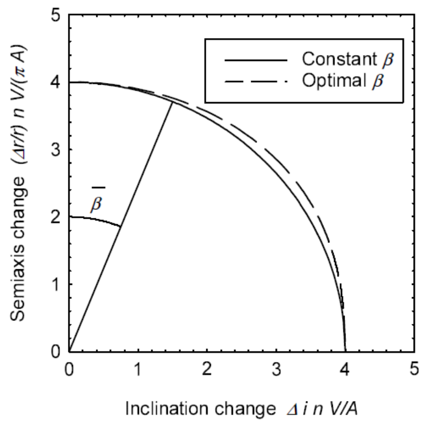

Figure 4.1: Difference between the optimal control law and the constant control law for β [4]

4.3.2 Multiple-Revolution Transfer

When larger changes in Δa and Δi are involved, a multi-revolution low-thrust transfer becomes necessary. To evaluate an optimal control law, the trajectory is assumed to remain nearly circular, and β is assumed to be constant during each revolution. The problem is now to determine the optimal value of β for each revolution along the transfer manoeuvre. The time derivatives of a and i are computed as the variation occurring over one revolution, averaged over the revolution period:

$$\frac{\dot{a}}{a} = \frac{2f\cos\beta}{V}\,; \qquad \dot{i} = \frac{2f\sin\beta}{\pi V}\,; \qquad \dot{V} = -\frac{n\dot{a}}{2} \tag{4.27}$$

After performing a change of variable, we get:

$$\frac{di}{dV} = -\frac{2\tan\beta}{\pi V}\,; \qquad \frac{dt}{dV} = -\frac{1}{f\cos\beta} \tag{4.28}$$

By applying optimal control theory to Equations (4.28), the optimal control law is derived:

$$V\sin\beta = V_0\sin\beta_0 = cost \tag{4.29}$$

This implies that the quantity $V\sin\beta$ must be conserved throughout the transfer manoeuvre, meaning that β must increase as the velocity decreases, i.e., as the spacecraft moves farther from the central body. This result is expected, as changes in inclination are optimal for low velocities, as discussed in the previous chapter. Figure (4.2) represents various transfer manoeuvres. For all initial values of β_0, there is a maximum reachable altitude r_{max}, which is attained when $\beta = 90°$. Beyond this point, β cannot increase any further. For larger inclination changes, a two-way transfer is required: after reaching

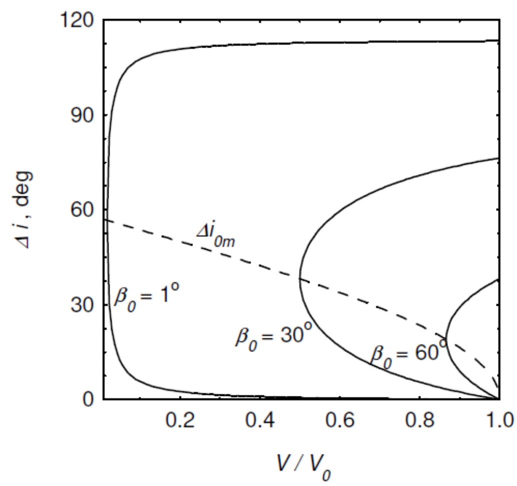

Figure 4.2: Edelbaum's three-dimensional multi-revolution transfer manoeuvre [4]

r_{max}, β is reduced, and the spacecraft is decelerated to lower the orbit altitude. Higher values of r_{max} can be achieved by starting with a lower β_0. Integrating Equations (4.28) yields:

$$\begin{aligned} \Delta V &= V_0 \cos\beta_0 - V_1 \cos\beta_1 \\ \Delta i &= \frac{2}{\pi} \sin^{-1}\left(\frac{V_0 \sin\beta_0}{V_1} - \beta_0\right) \end{aligned} \tag{4.30}$$

The maximum one-way inclination change is obtained for $\beta \to 0$, which gives $r_{max} \to \infty$, $\Delta i = 57.3°$ and $\Delta V = V_0 - V_1$. When $r_{max} \to \infty$, inclination changes become unrestricted, and i can be increased without bounds. For a two-way transfer, integrating from V_0 to $V_{r_{max}}$ and then from $V_{r_{max}}$ to V_1 leads to:

$$\Delta V = \begin{cases} \sqrt{V_0^2 + V_1^2 - 2V_0V_1\cos\left(\frac{\pi}{2}\Delta i\right)} & \text{if } \Delta i \leq 114.6° \\ V_0 + V_1 & \text{if } \Delta i > 114.6° \end{cases} \tag{4.31}$$

4.4 Edelbaum Dynamic Model with J2 Perturbation

Low Earth orbits cannot be fully described using the two-body problem approximation due to the presence of perturbing forces such as atmospheric drag and the Earth's non-sphericity. As discussed in Chapter (2.5.1), the primary effects of the Earth's non-sphericity, known as the J2 perturbation, are the regression of the line of nodes and the rotation of the line of apsides.

In this work, only the regression of the line of nodes is considered as a perturbing effect. Consequently, the Edelbaum dynamical model must be modified to account for this influence. The effect of J2 on Ω is described by the equation:

$$\dot{\Omega}_{J2} = -\frac{3}{2} J_2 \left(\frac{R_e}{a(1-e^2)} \right)^2 \sqrt{\frac{\mu}{a^3}} \cos(i) \tag{4.32}$$

Since the trajectory is assumed to remain nearly circular, e can be neglected:

$$\dot{\Omega}_{J2} = -\frac{3}{2} J_2 \frac{R_e^2 \, \mu^{1/2}}{a^{7/2}} \cos(i) \tag{4.33}$$

Including $\dot{\Omega}_{J2}$ in the dynamic model leads to:

$$\begin{aligned}
\dot{a} &= \tfrac{2af}{V} \cos\alpha \cos\beta \\
\dot{i} &= \tfrac{f}{V} \cos(\omega+\nu) \sin\beta \\
\dot{\Omega} &= f \sin(\omega+\nu) \frac{\sin\beta}{V \sin i} - \frac{3}{2} J_2 \tfrac{R_e^2 \, \mu^{1/2}}{a^{7/2}} \cos(i)
\end{aligned} \tag{4.34}$$

Equations (4.34) describe the dynamics of the system, including the perturbation due to the J2 effect. The equations for ν, ω, and e are omitted, as nearly circular orbits are considered. Furthermore, the rendezvous phase between the chaser and the target is not analyzed in this work.

4.4.1 One Revolution Transfer

The optimal control law for a one-revolution transfer is studied following a similar approach to that in Chapter (4.3). To this end, it is useful to introduce $\theta = \omega + \nu$ and rewrite Equations (4.34) using θ as the dependent variable and V as $\sqrt{\mu/a}$:

$$\begin{aligned}
\frac{da}{d\theta} &= \frac{2fa^3}{\mu} \cos\alpha \cos\beta, \\
\frac{di}{d\theta} &= \frac{fa^2}{\mu} \cos\theta \sin\beta, \\
\frac{d\Omega}{d\theta} &= \frac{fa^2}{\mu} \frac{\sin\theta \sin\beta}{\sin i} - \frac{3}{2} J_2 \left(\frac{R_e}{a} \right)^2 \cos(i), \\
\frac{dt}{d\theta} &= \sqrt{\frac{a^3}{\mu}}.
\end{aligned} \tag{4.35}$$

The thrust and mass of the spacecraft are assumed to be constant over one revolution. To obtain an indirect optimization of the problem, a Hamiltonian must be constructed as previously defined:

$$H = \boldsymbol{\lambda}^T \mathbf{f}, \tag{4.36}$$

where $\boldsymbol{\lambda} = [\lambda_a, \lambda_i, \lambda_\Omega]$ in this case. By performing some algebraic manipulations:

$$\begin{aligned} H = \lambda_a \frac{2fa^3}{\mu} \cos\alpha \cos\beta + \lambda_i \frac{fa^2}{\mu} \cos\theta \sin\beta \\ + \lambda_\Omega \frac{fa^2}{\mu} \frac{\sin\theta \sin\beta}{\sin i} - \lambda_\Omega \frac{3}{2} J_2 \left(\frac{R_e}{a}\right)^2 \cos(i). \end{aligned} \tag{4.37}$$

Since one revolution is being studied, H does not depend on the state variables (as a, i, and Ω have small variation in one revolution and can be considered as constants), and the adjoint variables result to be constant:

$$\frac{d\lambda_a}{dt} = -\frac{\partial H}{\partial a} = 0, \quad \frac{d\lambda_i}{dt} = -\frac{\partial H}{\partial i} = 0, \quad \frac{d\lambda_\Omega}{dt} = -\frac{\partial H}{\partial \Omega} = 0. \tag{4.38}$$

The optimal control law for the β angle can be obtained by setting the partial derivative of the Hamiltonian to zero:

$$\frac{\partial H}{\partial \beta} = 0 \quad \Longrightarrow \quad \tan\beta = \frac{\lambda_i \cos\theta + \lambda_\Omega \frac{\sin\theta}{\sin i}}{2\lambda_a a}. \tag{4.39}$$

It is useful to define the angle θ_0 as:

$$\tan\theta_0 = \frac{\lambda_\Omega}{\lambda_i} \sin i. \tag{4.40}$$

The parameter θ_0 helps analyze the thrust strategy, as it represents how the out-of-plane thrust effort is distributed between changes in i and changes in Ω. When $\tan\theta_0$ is close to 1 ($\lambda_\Omega \gg \lambda_i$), thrust is mainly used to change Ω, whereas when $\tan\theta_0$ is close to 0 ($\lambda_\Omega \ll \lambda_i$), thrust is mainly used to change i. Another auxiliary variable, Λ, is defined as:

$$\Lambda = \sqrt{\lambda_i^2 + \left(\frac{\lambda_\Omega}{\sin i}\right)^2}. \tag{4.41}$$

Equation (4.41) can be inverted to obtain expressions for λ_i and λ_Ω:

$$\lambda_i = \Lambda \cos\theta_0, \qquad \lambda_\Omega = \Lambda \frac{\sin\theta_0}{\sin i}. \tag{4.42}$$

Substituting these expressions into Equation (4.39) results in:

$$\tan\beta = \frac{\Lambda}{2\lambda_a a} \cos(\theta - \theta_0) = K \cos\theta'. \tag{4.43}$$

From Equation (4.43), expressions for $\cos\beta$ and $\sin\beta$ can be derived:

$$\cos\beta = \frac{1}{\sqrt{1 + (K\cos\theta')^2}}, \qquad \sin\beta = \frac{K\cos\theta'}{\sqrt{1 + (K\cos\theta')^2}}. \tag{4.44}$$

Substituting these into Equations (4.35) leads to:

$$\begin{aligned}
\frac{da}{d\theta'} &= \frac{2fa^3}{\mu}\frac{1}{\sqrt{1+(K\cos\theta')^2}}, \\
\frac{di}{d\theta'} &= \frac{fa^2}{\mu}\frac{K\cos\theta'}{\sqrt{1+(K\cos\theta')^2}}\cos(\theta'+\theta_0), \\
\frac{d\Omega}{d\theta'} &= \frac{fa^2}{\mu}\frac{\sin(\theta'+\theta_0)}{\sin i}\frac{K\cos\theta'}{\sqrt{1+(K\cos\theta')^2}} - \frac{3}{2}J_2\left(\frac{R_e}{a}\right)^2\cos(i), \\
\frac{dt}{d\theta} &= \sqrt{\frac{a^3}{\mu}}.
\end{aligned} \tag{4.45}$$

As in Chapter (4.3), solving Equations (4.45) requires elliptic integrals. In this case as well, β can also be assumed constant without losing precision, leading to:

$$\begin{aligned}
\Delta a &= \frac{4\pi a^3 f}{\mu}\cos\beta, \\
\Delta i &= \frac{fa^2}{\mu}\cos\theta_0\sin\beta, \\
\Delta\Omega &= \frac{fa^2}{\mu}\frac{\sin\beta}{\sin i}\sin\theta_0 - 3\pi J_2\left(\frac{R_e}{a}\right)^2\cos i, \\
\Delta t &= 2\pi\sqrt{\frac{a^3}{\mu}}.
\end{aligned} \tag{4.46}$$

The same solution is found for Δa. The main differences between the standard Edelbaum model and the modified Edelbaum model with J2 lie in Δi and $\Delta\Omega$ obtained through one revolution:

$$\Delta i = \Delta i_0\cos\theta_0, \qquad \Delta\Omega = \frac{\Delta i}{\sin i}\sin\theta_0 - 3\pi J_2\left(\frac{R_e}{a}\right)^2\cos i, \tag{4.47}$$

where Δi_0 is the result obtained through one-revolution integration of the standard Edelbaum model. The main differences lie in the presence of θ_0, which distributes the out-of-plane thrust effort between inclination changes and Ω changes, and the inclusion of the J2 term.

4.4.2 Multiple-Revolution Transfer

To extend the study from one-revolution transfer to a multiple-revolution transfer, the same assumptions made in Chapter (4.3.2) are considered: the trajectory is assumed to be nearly circular at all times, and β is assumed to be constant during each revolution. The time derivatives of the orbital elements are computed by averaging the changes over one revolution with respect to the orbital period. In a multiple-revolution transfer, the spacecraft mass cannot be considered constant. Therefore, the time-derivative equation of the mass must be included, and f is written as T/m:

$$\begin{aligned}
\frac{da}{dt} &= 2\frac{T}{m}\sqrt{\frac{a^3}{\mu}}\cos\beta \\
\frac{di}{dt} &= \frac{T}{2\pi m}\sqrt{\frac{a}{\mu}}\sin\beta\cos\theta_0 \\
\frac{d\Omega}{dt} &= \frac{T}{2\pi m}\sqrt{\frac{a}{\mu}}\frac{\sin\beta}{\sin i}\sin\theta_0 - \frac{3}{2}J_2\left(\frac{R_e}{a}\right)^2\sqrt{\frac{\mu}{a^3}}\cos i \\
\frac{dm}{dt} &= -\frac{T}{c}
\end{aligned} \tag{4.48}$$

where c is the effective exhaust velocity. To obtain an indirect optimization, an Hamiltonian is constructed:

$$H = \boldsymbol{\lambda}^T\mathbf{f}; \qquad \boldsymbol{\lambda}^T = [\lambda_a, \lambda_i, \lambda_\Omega, \lambda_m] \tag{4.49}$$

$$\begin{aligned}
H = {} & \frac{2T}{m\pi}\sqrt{\frac{a}{\mu}}\left(\lambda_a \pi a\cos\beta + \lambda_i\sin\beta\cos\theta_0 + \lambda_\Omega\frac{\sin\beta}{\sin i}\sin\theta_0\right) \\
& - \lambda_\Omega\frac{3}{2}J_2\left(\frac{R_e}{a}\right)^2\sqrt{\frac{\mu}{a^3}}\cos i - \lambda_m\frac{T}{m}
\end{aligned} \tag{4.50}$$

The time-derivative of the adjoint variables is computed as defined in Chapter (4.2):

$$\begin{aligned}
\frac{d\lambda_a}{dt} &= -\frac{\partial H}{\partial a} \\
&= -3\lambda_a\frac{T}{m}\sqrt{\frac{a}{\mu}}\cos\beta - \lambda_i\frac{T}{\pi m\sqrt{a\mu}}\sin\beta\cos\theta_0 \\
&\quad - \lambda_\Omega\frac{T}{\pi m\sqrt{a\mu}}\frac{\sin\beta}{\sin i}\sin\theta_0 + \lambda_\Omega\frac{21}{4}\left(\frac{R_e}{a}\right)^2\sqrt{\frac{\mu}{a^5}}\cos i
\end{aligned} \tag{4.51}$$

$$\frac{d\lambda_i}{dt} = -\frac{\partial H}{\partial i} = \lambda_\Omega\frac{2T}{m\pi}\sqrt{\frac{a}{\mu}}\frac{\cos i}{\sin^2 i}\sin\beta\sin\theta_0 - \frac{3}{2}J_2\left(\frac{R_e}{a}\right)^2\sqrt{\frac{\mu}{a^3}}\sin i \tag{4.52}$$

$$\frac{d\lambda_\Omega}{dt} = -\frac{\partial H}{\partial \Omega} = 0 \tag{4.53}$$

$$\begin{aligned}\frac{d\lambda_m}{dt} &= -\frac{\partial H}{\partial m} \\ &= \frac{2T}{\pi m^2}\sqrt{\frac{a}{\mu}}\left(\lambda_a \pi a \cos\beta + \lambda_i \sin\beta\cos\theta_0 + \lambda_\Omega \frac{\sin\beta}{\sin i}\sin\theta_0\right)\end{aligned} \tag{4.54}$$

The control variables for this problem are the thrust magnitude T, the out-of-plane thrust angle β, and θ_0. To obtain the optimal control law, the partial derivatives of the Hamiltonian with respect to θ_0 and β are nullified:

$$\frac{\partial H}{\partial \theta_0} = 0 \quad \longrightarrow \quad \tan\theta_0 = \frac{\lambda_\Omega}{\lambda_i \sin i} \tag{4.55}$$

$$\frac{\partial H}{\partial \beta} = 0 \quad \longrightarrow \quad \tan\beta = \frac{\lambda_i \cos\theta_0 + \lambda_\Omega \frac{\sin\theta_0}{\sin i}}{2\lambda_a a} \tag{4.56}$$

From Equations (4.55) and (4.56), the expressions for the sine and cosine of β and θ_0 can be derived, using the auxiliary variable Λ:

$$\sin\beta = \pm\frac{\Lambda}{\sqrt{\Lambda^2 + (\pi a \lambda_a)^2}} \tag{4.57}$$

$$\cos\beta = \pm\frac{\pi a \lambda_a}{\sqrt{\Lambda^2 + (\pi a \lambda_a)^2}} \tag{4.58}$$

$$\sin\theta_0 = \pm\frac{\lambda_\Omega}{\Lambda \sin i} \tag{4.59}$$

$$\cos\theta_0 = \pm\frac{\lambda_i}{\Lambda} \tag{4.60}$$

In agreement with Pontryagin's Maximum Principle, the optimal control laws must maximize the Hamiltonian. To achieve this, there must be consistency among the signs, and the correct quadrant for β and θ_0 must be selected. Assuming $\sin\beta$ is positive leads to:

$$\sin\beta = \frac{\Lambda}{\sqrt{\Lambda^2 + (\pi a \lambda_a)^2}} \tag{4.61}$$

$$\cos\beta = \frac{\pi a \lambda_a}{\sqrt{\Lambda^2 + (\pi a \lambda_a)^2}} \tag{4.62}$$

$$\sin\theta_0 = \frac{\lambda_\Omega}{\Lambda \sin i} \tag{4.63}$$

$$\cos\theta_0 = \frac{\lambda_i}{\Lambda} \tag{4.64}$$

Note that $\cos\beta$ has the same sign as λ_a. The same applies for $\cos\theta_0$ and $\sin\theta_0$, which have the same signs as λ_i and λ_Ω, respectively. It is important to note that the Hamiltonian is a linear function of T, so grouping the terms that contain T, Equation (4.50) can be written as:

$$H = TS_F - \lambda_\Omega \frac{3}{2} J_2 \left(\frac{R_e}{a}\right)^2 \sqrt{\frac{\mu}{a^3}} \cos i \tag{4.65}$$

where S_F is called the *Switching function*, and it is defined as:

$$S_F = \frac{2}{\pi m}\sqrt{\frac{a}{\mu}}\sqrt{(\pi a \lambda_a)^2 + \Lambda^2} - \frac{\lambda_m}{c} \tag{4.66}$$

According to Pontryagin's Maximum Principle, T and the switching function must be consistent: when $S_F > 0$, the thrust must be set to its maximum value, and when $S_F < 0$, the thrust must be set to its minimum value (i.e., the thruster should be turned off).

4.4.3 Boundary Conditions

The optimal control law depends on the boundary conditions of the problem and on the performance index. In this study, a set of initial orbital elements a_0, i_0, and Ω_0 at $t_0 = 0$ of the chaser orbit is given. The orbital elements of the target orbit, representing the final conditions, are also known and are defined as:

$$\begin{aligned} a_f &= a_0 + \Delta a \\ i_f &= i_0 + \Delta i \\ \Omega_f &= \Omega_0 + \Delta\Omega + \dot{\Omega}_{J2} \cdot t_f \end{aligned} \tag{4.67}$$

where Δa, Δi, and $\Delta\Omega$ are given, and t_f is the final time. To close the problem, two additional boundary conditions must be specified. These conditions are provided by optimal control theory and depend on the objective to be optimized. In the case of a minimum-time solution (with free final mass), the performance index to minimize is the final time, and the boundary conditions for optimality are:

$$\begin{aligned} H_f - \lambda_\Omega \dot{\Omega}_{J2} t_f &= 1 \\ \lambda_{mf} &= 0 \end{aligned} \tag{4.68}$$

In a minimum-time solution, the switching function always assumes positive values, and the thrust is always at its maximum value. The other unknown boundary conditions represent the unknowns of the two-point boundary value problem: t_f, λ_{a0}, λ_{i0}, λ_Ω, and λ_{m0}. Note that λ_Ω is constant since $\dot{\lambda}_\Omega = 0$. It is important to mention that this problem is homogeneous in the adjoint variables, so the solution is "scalable," meaning it is determined up to a scale factor. Therefore, it is possible to specify the initial value of one adjoint variable, in this case λ_Ω. Note that the sign of λ_Ω must be assigned correctly to avoid negative flight times: the sign must match that of $\Delta\Omega$. The unknowns of the problem are then reduced to four: t_f, λ_{a0}, λ_{i0}, and λ_{m0}.

In a minimum-propellant solution (or maximum final mass), the cost function to maximize is the final mass of the spacecraft, and the boundary conditions for optimality are:

$$\begin{aligned} \lambda_{mf} &= 1 \\ t_f &= k \end{aligned} \tag{4.69}$$

where k is given. If the final time is not given, then the last boundary condition can be substituted with:

$$H_f - \lambda_\Omega \dot{\Omega}_{J2} \cdot t_f = 0 \tag{4.70}$$

In this case, the switching function can assume both positive and negative values, and the engine can be turned off.

4.5 Approximate Optimization Method

The indirect trajectory optimization through the Edelbaum dynamic model, modified with J2, cannot be obtained analytically and can only be solved using numerical methods, such as the shooting method, which involves a significant computational cost. This requires the implementation of techniques to obtain numerical solutions to differential equations, such as time-marching methods (Euler method, Crank-Nicolson method, Runge-Kutta methods, etc.) or collocation methods. Another critical point is that a good initial guess for the adjoint variables is necessary; otherwise, the algorithm risks failing to converge to the solution.

On the other hand, an analytical solution does not require numerical iteration and can be useful for easily assessing trajectory optimization problems. In the following chapters, an approximate optimization method based on analytical solutions is presented, for further details see [20].

4.5.1 Approximate Transfer Cost

In Chapter (4.3), the expression for ΔV for a transfer between circular orbit with combined change in inclination and altitude was derived:

$$\Delta V = \sqrt{V_0^2 + V_f^2 - 2V_0V_f \cos\left(\frac{\pi}{2}\Delta i\right)} \tag{4.71}$$

The quantity $\frac{\pi}{2}\Delta i$ is now assumed small in order to perform the following approximation:

$$\cos\left(\frac{\pi}{2}\Delta i\right) \approx 1 - \frac{\left(\frac{\pi}{2}\Delta i\right)^2}{2} \tag{4.72}$$

substituting Equation (4.72) into Equation (4.71) leads to:

$$\Delta V = \sqrt{V_0 V_f \left(\frac{\pi}{2}\Delta i\right)^2 + (V_0 + V_f)^2} \tag{4.73}$$

for small Δa the equation can be further simplified, obtaining:

$$\Delta V = \overline{V}\sqrt{\left(\frac{\pi}{2}\Delta i\right)^2 + \left(\frac{\Delta a}{2\overline{a}}\right)} \tag{4.74}$$

where $\overline{a}$ and $\overline{V}$ are the average values of the semi-major axis and velocity respectively:

$$\overline{a} = \frac{a_0 + a_f}{2} \qquad\qquad \overline{V} = \sqrt{\frac{\mu}{\overline{a}}} \tag{4.75}$$

Equation (4.75) considers only change in inclination and altitude, the two terms contained in the parenthesis can be interpreted as the transfer cost for changing i and a. To modify Equation (4.75) to include Ω changes, the time-derivatives of i and of Ω from Equations (4.13) must be computed averaging the angular position from the unaveraged di/dt and $d\Omega/dt$, using as integration limits $u' - \pi/2$ and $u' - \pi/2$:

$$\frac{d\tilde{i}}{dt} = \frac{1}{2\pi}\int_0^{2\pi} \frac{di}{dt}\, d\theta = \frac{2f\sin\beta}{2\pi V}\int_{u'-\pi/2}^{u'+\pi/2} \cos\theta \, d\theta = \frac{2f\sin\beta}{\pi V}\cos u' \tag{4.76}$$

$$\frac{d\tilde{\Omega}}{dt} = \frac{1}{2\pi}\int_0^{2\pi} \frac{d\Omega}{dt}\, d\theta = \frac{2f\sin\beta}{2\pi V\sin i}\int_{u'-\pi/2}^{u'+\pi/2} \sin\theta \, d\theta = \frac{2f\sin\beta}{\pi V\sin i}\sin u' \tag{4.77}$$

where u' is the argument of latitude of the common point between the two orbits. Eliminating the tilde, the dynamic model can be written as:

$$\begin{aligned}\frac{di}{dt} &= \frac{2f}{\pi V}\sin\beta\cos u' \\ \frac{d\Omega}{dt} &= \frac{2f}{\pi V}\frac{\sin\beta}{\sin i}\sin u' \\ \frac{dV}{dt} &= -f\cos\beta\end{aligned} \tag{4.78}$$

If small changes in velocity, inclination and RAAN between subsequent circular orbits are considered, the common point u' and inclination i on the right-hand side of Equations (4.78) can be assumed constant. This assumption allows the analytic integration of Equations (4.78). The Hamiltonian can be constructed as:

$$H = \lambda_i \frac{2f}{\pi V} \sin\beta \cos u' + \lambda_\Omega \frac{2f}{\pi V} \frac{\sin\beta}{\sin\bar{i}} \sin u' - \lambda_V f \cos\beta \tag{4.79}$$

and the adjoint equations are:

$$\begin{aligned} \frac{d\lambda_V}{dt} &= -\frac{\partial H}{\partial V} = \lambda_i \frac{2f}{\pi V^2} \sin\beta \cos u' + \lambda_\Omega \frac{2f}{\pi V^2} \frac{\sin\beta}{\sin\bar{i}} \sin u' \\ \frac{d\lambda_i}{dt} &= -\frac{\partial H}{\partial i} = 0 \\ \frac{d\lambda_\Omega}{dt} &= -\frac{\partial H}{\partial \Omega} = 0 \end{aligned} \tag{4.80}$$

The optimal control law for β can be obtained by nullifying the partial derivative of the Hamiltonian:

$$\frac{\partial H}{\partial \beta} = 0 \qquad \longrightarrow \qquad \tan\beta = -\frac{2}{\pi V \sin\bar{i}} \frac{\lambda_\Omega}{\lambda_V} \sin u' - \frac{2}{\pi V} \frac{\lambda_i}{\lambda_V} \cos u' \tag{4.81}$$

As stated before, for a minimum-time solution the cost function to minimize is represented by the final time, which gives $H_f = 1$ as the boundary condition, and together with Equation (4.79) yields:

$$\lambda_V = -\frac{\cos\beta}{f} \tag{4.82}$$

$$\lambda_i \left(\frac{2f}{\pi V} \cos u' \right) + \lambda_\Omega \left(\frac{2f}{\pi V \sin\bar{i}} \sin u' \right) = \sin\beta. \tag{4.83}$$

Since λ_i and λ_Ω are constant, dV/dt in Equations (4.78) can be integrated to obtain:

$$V = \sqrt{V_0^2 + f^2 t^2 - f t V_0 \cos\beta_0} \tag{4.84}$$

With some manipulation, the expressions for Δi and $\Delta\Omega$ are obtained:

$$\Delta i = \frac{2\cos u'}{\pi} \left[\arctan\left(\frac{ft - V_0 \cos\beta_0}{V_0 \sin\beta_0} \right) + \frac{\pi}{2} - \beta_0 \right] \tag{4.85}$$

$$\Delta\Omega = \frac{2\sin u'}{\pi \sin\bar{i}} \left[\arctan\left(\frac{ft - V_0 \cos\beta_0}{V_0 \sin\beta_0} \right) + \frac{\pi}{2} - \beta_0 \right] \tag{4.86}$$

The three variables β_0, t and u' and the three constraints (Equations (4.84), (4.85) and (4.86)) enable V_f, i_f and Ω_f to be the desired ones. Equations (4.85) and (4.86) can be combined to obtain:

$$\sqrt{\Delta i^2 + (\sin\bar{i}\Delta\Omega)^2} = \frac{2}{\pi} \left[\arctan\left(\frac{ft - V_0 \cos\beta_0}{V_0 \sin\beta_0} \right) + \frac{\pi}{2} - \beta_0 \right] \tag{4.87}$$

This is a result similar to that obtained in the analysis of the combined maneuver of changing a and i, except for the term $\sqrt{\Delta i^2 + (\sin \bar{i} \Delta\Omega)^2}$ appearing on the right-hand side instead of Δi. Equation (4.71) can therefore be written, by analogy, as:

$$\Delta V = \sqrt{V_0^2 + V_f^2 - 2V_0 V_f \cos\left(\frac{\pi}{2}\sqrt{\Delta i^2 + (\sin \bar{i} \Delta\Omega)^2}\right)} \tag{4.88}$$

As before, the quantity $\pi/2\sqrt{\Delta i^2 + (\sin i \Delta\Omega)^2}$ is assumed to be small, so Equation (4.88) can be written as:

$$\Delta V = \sqrt{\frac{\mu}{\bar{a}}}\left[\left(\frac{\pi}{2}\Delta i\right)^2 + \left(\frac{\pi}{2}\sin \bar{i} \Delta\Omega\right)^2 + \left(\frac{\Delta a}{2\bar{a}}\right)^2\right]^{\frac{1}{2}} \tag{4.89}$$

Note that Equation (4.89) is similar to a root-sum-square of all individual ΔV values: the terms enclosed in parentheses represent the transfer cost for changing a, i and Ω to reach the target orbit.

4.5.2 Approximate J2-perturbed Transfer Cost

After obtaining an expression for the ΔV of a combined transfer of a, i, and Ω, the effect of the J2 perturbation is incorporated into the model. Referring to Equation (4.89), the three velocity changes can be denoted as x, y, and z:

$$x = \frac{\pi}{2}\left(\Omega_t(t) - \Omega_c(t)\right)\sin \bar{i}\, \overline{V} \tag{4.90}$$

$$y = \frac{a_f - a_0}{2\bar{a}}\sqrt{\frac{\mu}{\bar{a}}} \tag{4.91}$$

$$z = \frac{\pi}{2}\left(i_f - i_0\right)\overline{V} \tag{4.92}$$

where $\bar{a} = (a_f - a_0)/2$ and $\bar{i} = (i_f - i_0)/2$. Two cases are considered: an analytic solution for a combined a and i transfer, where the changes in Ω are accounted for only by natural drift, and an analytic solution for a combined a, i, and Ω transfer, where thrust is actively used to modify Ω.

4.5.2.1 Analytic Solution for a combined a and i transfer

With a given flight time, a thrust-coast-thrust profile is considered, where the Δa and Δi are distributed between the two thrust arcs. The change in Ω is obtained by natural drift, as long as the transfer time is long enough. To identify the changes in y and z at each thrust arc, the scaling terms k_y and k_z

are introduced. They represent the percentage of the velocity change at the first thrust arc. Thus, the velocity change during the first thrust phase, ΔV_1, can be written as:

$$\Delta V_1 = \sqrt{(k_y y)^2 + (k_z z)^2} \tag{4.93}$$

Note that there are no constraints on k_y and k_z, which means that the changes in a and i can be larger than the original differences, in order to exploit the J2 effect to change Ω. The expression for $\dot{\Omega}_{J2}$ (Equation (4.32)), for small changes in semi-major axis and inclination, can be written as:

$$\frac{\Delta\dot{\Omega}}{\dot{\Omega}} = -\frac{7}{2}\frac{\Delta a}{a} - \tan(i\Delta i) \tag{4.94}$$

Equation (4.94) can be combined with Equations (4.91) and (4.92) to obtain two auxiliary variables, m and n:

$$m = \frac{7\pi}{2}\bar{\dot{\Omega}} \sin \bar{i} t \qquad n = \bar{\dot{\Omega}} \tan \bar{i} \sin \bar{i} t \tag{4.95}$$

where $\bar{\dot{\Omega}}$ is the average RAAN rate of the chaser and the target. During the transfer time, the control of altitude and inclination by the first arc leads to a change in Ω:

$$\Delta x = m k_y y + n k_z z \tag{4.96}$$

The velocity change associated with the second arc, ΔV_2, can be written as:

$$\Delta V_2 = \sqrt{(y - k_y y)^2 + (z - k_z z)^2} \tag{4.97}$$

Therefore, the total ΔV is:

$$\Delta V = \Delta V_1 + \Delta V_2 = \sqrt{(k_y y)^2 + (k_z z)^2} + \sqrt{(y - k_y y)^2 + (z - k_z z)^2} \tag{4.98}$$

The change in Ω is entirely due to the J2 effect, so:

$$x + \Delta x = 0 \tag{4.99}$$

To find the minimum ΔV, an analytic approximation is derived by squaring the two velocities to remove the square roots:

$$\Delta V_1^2 + \Delta V_2^2 = (k_y y)^2 + (k_z z)^2 + (y - k_y y)^2 + (z - k_z z)^2 \tag{4.100}$$

Note that the cross-product term $2\Delta V_1 \Delta V_2$ is neglected. To obtain the minimum $\Delta V_1^2 + \Delta V_2^2$, a constrained minimization problem must be solved, with Equation

(4.99) as the constraint. Thus, a Lagrangian function can be constructed:

$$L = (k_y y)^2 + (k_z z)^2 + (y - k_y y)^2 + (z - k_z z)^2 + \rho(x + mk_y y + nk_z z) \quad (4.101)$$

where ρ is the Lagrange multiplier. Nullifying the partial derivatives of the Lagrangian function with respect to k_y and k_z yields:

$$\begin{aligned} \frac{\partial L}{\partial k_y} &= (4yk_y - 2y + \rho m)y = 0 \\ \frac{\partial L}{\partial k_z} &= (4zk_z - 2z + \rho n)z = 0 \\ \frac{\partial L}{\partial \rho} &= x + mk_y y + nk = 0 \end{aligned} \quad (4.102)$$

Equations (4.102) can be manipulated to obtain the unknowns k_y and k_z:

$$\begin{aligned} k_y &= \frac{2mx - n^2 y + mnz}{2(m^2 + n^2)y} \\ k_z &= \frac{2nx + mny - m^2 z}{2(m^2 + n^2)z} \end{aligned} \quad (4.103)$$

Substituting k_y and k_z into Equation (4.98), the optimal ΔV can be estimated.

4.5.2.2 Analytic Solution for a combined a, i and Ω transfer

When active Ω changes are involved, Equation (4.98) becomes:

$$\begin{aligned} \Delta V = \Delta V_1 + \Delta V_2 = &\sqrt{(k_x x)^2 + (k_y y)^2 + (k_z z)^2} + \\ &+ \sqrt{(x - k_x x + \Delta x)^2 + (y - k_y y)^2 + (z - k_z z)^2} \end{aligned} \quad (4.104)$$

where k_x is a term introduced to describe the magnitude of active control within the required velocity change for a Ω change of x. Equation (4.96), which expresses the change in ΔV required to close the RAAN difference due to the changes in semi-major axis and inclination, remains valid. Similar to the previous cases, the optimal values of k_x, k_y, and k_z can be obtained by setting the partial derivatives of $\Delta V_1^2 + \Delta V_2^2$ to zero:

$$\begin{aligned} \tfrac{\partial(\Delta V_1^2 + \Delta V_2^2)}{\partial k_x} &= 2x(2xk_x - myk_y - nzk_z - x) = 0 \\ \tfrac{\partial(\Delta V_1^2 + \Delta V_2^2)}{\partial k_y} &= 2y(-mxk_x + 2yk_y + m^2 yk_y + mnzk_z - y + mx) = 0 \\ \tfrac{\partial(\Delta V_1^2 + \Delta V_2^2)}{\partial k_z} &= 2z(-nxk_x + mnyk_y + 2zk_z + n^2 zk_z - z + x) = 0 \end{aligned} \quad (4.105)$$

From Equations (4.105), the optimal values of k_x, k_y, and k_z can be derived:

$$\begin{aligned} k_x x &= \frac{2x + my + nz}{4 + m^2 + n^2} \\ k_y y &= \frac{2mx - (4 + n^2)y + mnz}{8 + 2m^2 + 2n^2} \\ k_z z &= \frac{2nx + mny - (4 + m^2)z}{8 + 2m^2 + 2n^2} \end{aligned} \tag{4.106}$$

By substituting Equations (4.106) into Equation (4.104), the approximate optimal ΔV can be obtained.

4.5.3 The Arc-Impulse Method

To summarize Chapter (4.5.2), considering a thrust-coast-thrust combined $[a,\ i,\ \Omega]$ transfer manoeuvre, Equations (4.106) and (4.104) allow for the determination of the optimal velocity change for both the first and second thrust phase.

The Arc-Impulse method is a simple algorithm that improves the analytical results by accounting for the duration of the thrust arc, thereby enabling the analysis of minimum-time solutions. It is important to note that, in the cases presented in Chapter (4.5.2), the flight time Δt is given. Initially, the manoeuvre is modelled as a two-impulse transfer, with the first impulse ΔV_1 applied at t_0 and the second impulse ΔV_2 at t_f. These velocity changes are computed as in Chapter (4.5.2.2), using:

$$\Delta a = a_f - a_0; \qquad \Delta i = i_f - i_0; \qquad \Delta\Omega = \Omega_{tar}(t_0) - \Omega_{ch}(t_0) \tag{4.107}$$

and the given $\Delta t = t_f - t_0$. Additionally, the transfer cost can be evaluated as a single-impulse transfer by setting:

$$k_x = k_y = k_z = 1 \tag{4.108}$$

which considers only an impulse at the initial time, or by setting:

$$k_x = k_y = k_z = 0 \tag{4.109}$$

which considers only an impulse at the final time. The minimum total ΔV is then selected. Once ΔV_1 and ΔV_2 are determined, the impulses are converted in thrust arcs, with their durations computed as follows:

$$\Delta t_a = \frac{\Delta V_1}{a}, \qquad \Delta t_b = \frac{\Delta V_2}{a} \tag{4.110}$$

	Time	Event
Thrust Arc a	$t_0 \longrightarrow t_a = t_0 + \Delta t_a/2$	The spacecraft waits on the departure orbit
	t_a	First impulse ΔV_1
	$t_a \longrightarrow t_1 = t_a + \Delta t_a/2$	The spacecraft waits on the transfer orbit
Coast Arc	$t_1 \longrightarrow t_2 = t_1 + \Delta t_{coast}$	The spacecraft waits on the transfer orbit
Thrust Arc b	$t_2 \longrightarrow t_b = t_2 + \Delta t_b/2$	The spacecraft waits on the transfer orbit
	t_b	Second impulse ΔV_2
	$t_b \longrightarrow t_f = t_b + \Delta t_b/2$	The spacecraft waits on the arrival orbit

Table 4.1: Description of the two-impulse manoeuvre with the impulses positioned at the midpoint of their respective thrust arcs

Subsequently, the two impulses are shifted from t_0 and t_f so that they are positioned at the midpoints of their respective thrust arcs. The new two-impulse transfer is structured as shown in Table (4.1). At this stage, the actual duration of the manoeuvre is given by:

$$\Delta t_{transfer} = \Delta t - \frac{\Delta t_a}{2} - \frac{\Delta t_b}{2} = \Delta t_{coast} + \frac{\Delta t_a}{2} + \frac{\Delta t_b}{2} \tag{4.111}$$

where Δt_{coast} represents the duration of the coasting phase between the two thrust arcs. Additionally, Ω_{tar} and Ω_{ch} must be updated, since the transfer manoeuvre starts at $t_a = t_0 + \Delta t_a/2$:

$$\Omega_{tar}(t_a) = \Omega_{tar}(t_0) + \dot{\Omega}_{tar} \cdot \frac{\Delta t_a}{2}; \quad \Omega_{ch}(t_a) = \Omega_{ch}(t_0) + \dot{\Omega}_{ch} \cdot \frac{\Delta t_b}{2} \tag{4.112}$$

With the updated values of Ω_{tar}, Ω_{ch} and $\Delta t_{transfer}$, the transfer cost can be reevaluated, and the entire process can be iterated until ΔV converges.

4.5.3.1 Arc-Impulse algorithm for minimum-time solution and minimum propellant solutions

To summarize, the steps performed to obtain the **minimum-propellant solution** are shown below:

1. Δa, Δi, $\Delta\Omega$, and Δt are taken as inputs.

2. ΔV is computed by considering: an optimal 2-impulse transfer, an impulse at the initial time and an impulse at the final time. The minimum ΔV is selected.

3. The feasibility of the maneuver is assessed: if $\Delta V/a_0 \leq \Delta t$, the transfer is feasible; otherwise, the process is terminated. a_0 is computed as $a_0 = T/m_0$, with T and m_0 given.

4. The duration of the thrust arcs is computed as: $\Delta t_a = \Delta V_1/a_0$, $\Delta t_b = \Delta V_2/a_0$.

5. The two impulses are shifted so that they are positioned at the midpoints of their respective thrust arcs. The values of Δt, Ω_{ch}, and Ω_{tar} are updated. ΔV is reevaluated as in step 2.

6. Steps 2 to 6 are repeated until the relative difference between the ΔV values of two consecutive iterations is less than ϵ, with ϵ given.

7. ΔV and $m_f/m_0 = e^{-\Delta V/c}$ are returned as outputs.

In a **minimum-time solution**, Δt is an unknown. The previous algorithm is modified by adding another loop:

1. Δa, Δi, and $\Delta\Omega$ are taken as inputs.

2. A trial value of Δt is given.

3. ΔV is computed by considering an optimal 2-impulse transfer: an impulse at the initial time and an impulse at the final time. The minimum ΔV is selected.

4. The feasibility of the maneuver is assessed: if $\Delta V/a_0 \leq \Delta t$, the transfer is feasible; otherwise, Δt is incremented by a given value δt. Steps 2 and 3 are repeated until the feasibility condition is met.

5. The duration of the thrust arcs is computed as: $\Delta t_a = \Delta V_1/a_0$, $\Delta t_b = \Delta V_2/a_0$.

6. The two impulses are shifted so that they are positioned at the midpoints of their respective thrust arcs. The values of Δt, Ω_{ch}, and Ω_{tar} are updated. ΔV is reevaluated as in step 3.

7. Steps 3 to 6 are repeated until the relative difference between the ΔV values of two consecutive iterations is less than ϵ, with ϵ given.

8. Δt, ΔV, and $m_f/m_0 = e^{-\Delta V/c}$ are returned as outputs.

Note that, in the previous algorithm, the acceleration a_0 is assumed to be constant throughout the maneuver: the mass reduction due to propellant consumption is not taken into account. The algorithms can be modified to account for this effect:

- Once ΔV_1 and ΔV_2 are determined, the spacecraft mass after the two impulses is computed as: $m_a = m_0 e^{-\Delta V_1/c}$, $m_b = m_a e^{-\Delta V_2/c}$.

- The acceleration during the first thrust arc is computed as: $a_a = \frac{T}{1/2(m_0+m_a)}$. The acceleration during the second thrust arc is computed as: $a_b = \frac{T}{1/2(m_a+m_b)}$.
- The duration of the two thrust arcs is computed as: $\Delta t_a = \Delta V_1/a_a$, $\Delta t_b = \Delta V_2/a_b$.
- The feasibility condition becomes $\Delta V_1/a_a + \Delta V_2/a_b \leq \Delta t$.

Chapter 5

Results

In this chapter, the solutions for various low-thrust many-revolution transfer manoeuvres are presented, focusing on transfer optimization through the indirect method and the approximate arc-impulse method. The indirect method solutions are implemented using a `FORTRAN` script, while the approximate arc-impulse method solutions are implemented using a `MATLAB` script.

All transfer manoeuvres assume a chaser orbit at an altitude of $h = 400\ km$, with an orbital inclination of $i_0 = 51°$ and a right ascension of the ascending node of $\Omega_0 = 0°$. The spacecraft considered for these case studies has an initial mass of $m_0 = 15\ kg$, and its propulsion system is characterized by a thrust of $T = 0.01\ N$ and a specific impulse of $I_{sp} = 2500\ s$. All parameters are summarized in Table (5.1).

The transfer manoeuvres are categorized into different groups:

- Manoeuvres involving changes in altitude with $\Delta\Omega > 0$ ($\Delta a \neq 0$, $\Delta i = 0$, $\Delta\Omega \neq 0$)
- Manoeuvres involving changes in altitude with $\Delta\Omega < 0$ ($\Delta a \neq 0$, $\Delta i = 0$, $\Delta\Omega \neq 0$)
- Manoeuvres involving only changes in Ω ($\Delta a = 0$, $\Delta i = 0$, $\Delta\Omega \neq 0$)
- Manoeuvres involving combined changes in altitude and orbital inclination with $\Delta\Omega > 0$ ($\Delta a \neq 0$, $\Delta i \neq 0$, $\Delta\Omega \neq 0$)
- Manoeuvres involving combined changes in altitude and orbital inclination with $\Delta\Omega < 0$ ($\Delta a \neq 0$, $\Delta i \neq 0$, $\Delta\Omega \neq 0$)

Additionally, the solutions are further divided into *minimum-time solutions* and *minimum-propellant solutions*.

Chaser Orbit		S/c Parameters	
h	400 km	T	0.01 N
i_0	51°	I_{sp}	2500 s
Ω_0	0°	m_0	15 kg

Table 5.1: Chaser orbit and spacecraft parameters

5.1 Change of Altitude with $\Delta\Omega > 0$

5.1.1 Case 1 - Manoeuvre with $\Delta a = 700\ km$ and $\Delta\Omega = 10°$

5.1.1.1 Minimum time solution

The trends of altitude and Δi over time are shown in Figures (5.1) and (5.2), respectively. The optimal strategy followed by the indirect method consists of an increase in altitude above the target orbit, reaching a maximum altitude of $h_{max} = 1473\ km$ at $t_{h_{max}} = 14.49\ d$, and then a decrease in altitude to reach the target orbit. The same applies to Δi. Even though the orbital inclinations of the chaser and target orbits are the same, Δi is not zero throughout the manoeuvre. Instead, it increases to a maximum of $\Delta i_{max} = 0.2803°$ at $t_{\Delta i_{max}} = 13.03\ d$ and then decreases to zero to match the target orbit's inclination. This strategy is used to optimize the $\Delta\Omega$ change.

As discussed in the previous chapter, the nodal precession due to the J2 perturbation is inversely proportional to the square root of a cubed and directly proportional to the cosine of i. When $\Delta\Omega > 0$ at t_0, the two orbits tend to drift apart since the chaser orbit regresses faster than the target orbit, widening the $\Delta\Omega$ gap, as seen in Figure (5.3). To take advantage of the J2 effect, the altitude must be increased above the target orbit, and the small increase in orbital inclination aids this process.

It is worth noting that the maximum Δi is reached before the maximum altitude. This is an unexpected behaviour since, to optimize inclination changes, a should be as high as possible. It is possible that this behaviour occurs because, at higher altitudes, changes in i are less effective in influencing the J2 perturbation. Therefore, Δi_{max} is achieved first to optimize the $\Delta\Omega$ change.

Figure (5.4) shows the trends of β and θ_0 over time. From t_0 to $t_{\Delta i_{max}}$, β lies in the first quadrant ($0 < \beta < 90°$) to achieve positive changes in h and Δi. As altitude increases, β increases as well. As expected, the out-of-plane thrust component is higher when the spacecraft is near the maximum altitude, as inclination changes become more efficient. At $t_{h_{max}}$, $\beta = 90°$, and then the thrust vector is oriented to reduce h.

When Δi is near its maximum, θ_0 remains close to 90°, indicating that the

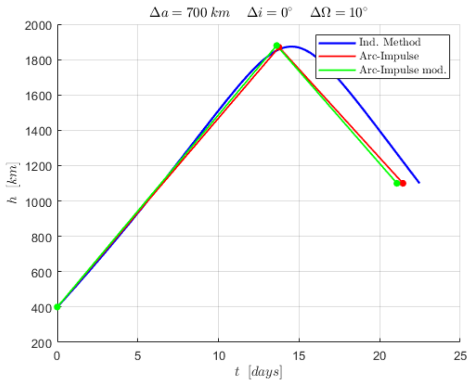

Figure 5.1: Trend of h over time (Minimum-time solution, $\Delta a = 700\,km$ $\Delta i = 0°$ $\Delta\Omega = 10°$)

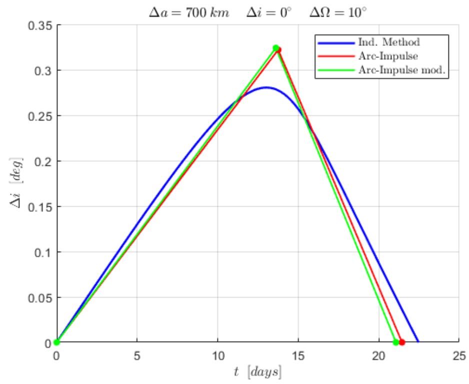

Figure 5.2: Trend of Δi over time (Minimum-time solution, $\Delta a = 700\,km$ $\Delta i = 0°$ $\Delta\Omega = 10°$)

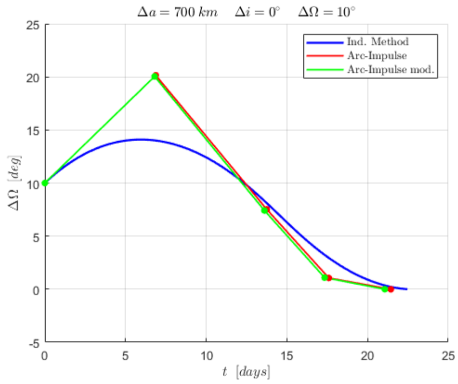

Figure 5.3: Trend of $\Delta\Omega$ over time (Minimum-time solution, $\Delta a = 700\,km$ $\Delta i = 0°$ $\Delta\Omega = 10°$)

out-of-plane thrust effort is focused on reducing $\Delta\Omega$. This is evident in Figure (5.3), where, between $t_{\Delta i_{max}}$ and $t_{h_{max}}$, the slope of the curve is steeper.

The strategy followed by the approximate method is the same. The maximum altitude reached is almost the same as in the indirect method, while the maximum Δi is higher. Both maxima are achieved simultaneously at $t = 13.75; d$. This difference is due to the fact that, to reach the target orbit, the approximate method considers two thrust arcs, t_a and t_b. In the minimum-time solution, the arc t_b starts immediately after the end of arc t_a, so the changes in altitude and inclination occur at the same time.

On the other hand, in the minimum-time solution of the indirect method, by adjusting the thrust vector angle β, the thrust effort can be distributed to achieve changes in a, i, and Ω. As a result, the maxima of altitude and Δi can occur at different times. It is worth noting that the average of $t_{h_{max}}$ and $t_{\Delta i_{max}}$ is approximately equal to t_a.

The approximate solutions closely follow the behaviour of the indirect solution during the first thrust arc. However, in the second thrust arc, a greater

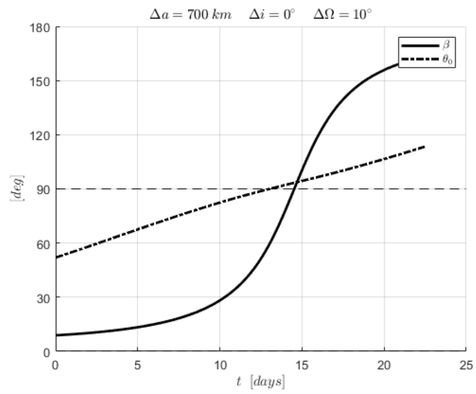

Figure 5.4: Trend of θ_0 and β angle over time in the indirect solution (Minimum-time solution, $\Delta a = 700\,km$ $\Delta i = 0°$ $\Delta\Omega = 10°$)

discrepancy arises due to the temporal offset between the peaks of h and Δi. The time evolution of $\Delta\Omega$ deviates the most due to the "impulsive" nature of the approximate method.

In terms of ΔV and Δt, the results are close to those of the indirect method, with a 6% difference in ΔV and a 4.5% difference in Δt. The solution of the modified arc-impulse method is similar to that of the arc-impulse method and does not provide any significant advantages.

5.1.1.2 Minimum propellant solution

For the minimum propellant solution, a flight time of $\Delta t = 1.5 \cdot t_{min_{ind}}$ is considered. In figures (5.5) and (5.6), the trends of h and Δi over time are shown.

The optimal strategy adopted by the indirect method consists of two thrust

[1] Average between $t_{h_{max}}$ and $t_{\Delta i_{max}}$

		Indirect Method		Arc-Imp. Method		Mod. Arc-Imp. Method	
		Arc a	Arc b	Arc a	Arc b	Arc a	Arc b
ΔV	$[km/s]$	1.3297		1.2350		1.2445	
Δt	$[days]$	22.4704		21.4430		21.0678	
ΔV	$[km/s]$	0.8092	0.5205	0.7921	0.4429	0.7966	0.4479
Δt	$[days]$	13.763 [1]	8.707	13.752	7.688	13.609	7.458
$\Delta V_{\Delta a}$	$[km/s]$			0.7709	-0.4037	0.7746	-0.4074
Δa	$[km]$	1473.43	-773.43	1469.67	-769.63	1476.72	-776.68
$\Delta V_{\Delta i}$	$[km/s]$			0.0660	-0.0660	0.0664	-0.0664
Δi	$[deg]$	0.2803	-0.2803	0.3219	-0.3219	0.3238	-0.3238
$\Delta\Omega_{tot}$	$[deg]$			35.959		35.577	
$\Delta\Omega_{J2}$	$[deg]$			-33.830		-33.396	
$\Delta V_{\Delta\Omega}$	$[km/s]$			0.1696	0.1697	0.1737	0.1737
$\Delta\Omega$	$[deg]$			1.0645	1.0651	1.0902	1.0902

Table 5.2: Results of the three methods for $\Delta a = 700\ km$, $\Delta i = 0°$, $\Delta\Omega = 10°$

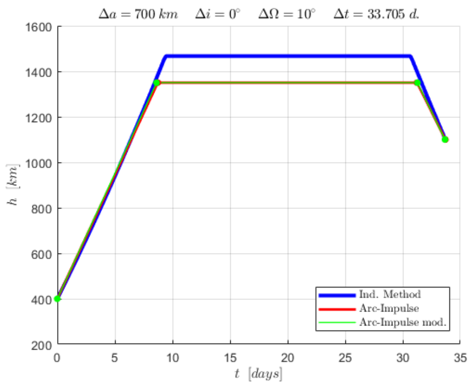

Figure 5.5: Trend of h over time (Minimum-propellant solution, $\Delta a = 700\,km$ $\Delta i = 0°$ $\Delta\Omega = 10°$, duration $= 33.705\,d$)

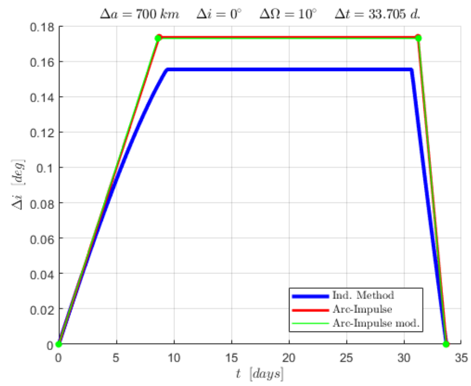

Figure 5.6: Trend of Δi over time (Minimum-propellant solution, $\Delta a = 700\,km$ $\Delta i = 0°$ $\Delta\Omega = 10°$, duration $= 33.705\,d$)

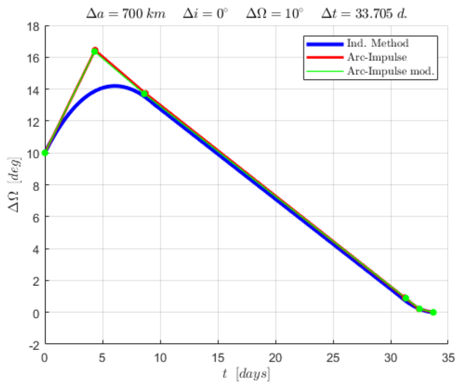

Figure 5.7: Trend of $\Delta\Omega$ over time (Minimum-propellant solution, $\Delta a = 700\,km$ $\Delta i = 0°$ $\Delta\Omega = 10°$, duration $= 33.705\,d$)

arcs with an intermediate coasting phase. During the first thrust arc, the altitude is increased above the target altitude, after which the thrust is turned off. At the end of the coasting phase, the thrust is turned on again, and the altitude is decreased to reach the target orbit. The same strategy applies to Δi.

As observed in the minimum-time solution, this strategy is used to take advantage of the differential precession between the coasting orbit and the target orbit, since the coasting orbit is higher than the target orbit. The h_{max} and Δi_{max} achieved are significantly lower than in the minimum-time solution because the J2 effect can be exploited for a longer period of time.

The approximate solutions closely follow the behaviour of the indirect solution, but the maximum altitude reached is lower, while the maximum Δi is higher. Another notable difference is that the two thrust arcs are shorter, and the coasting phase is longer. Figure (5.7) shows that the effect of the differential precession between the coasting orbit and the target orbit (the linear portion

		Indirect Method		Arc-Imp. Method		Mod. Arc-Imp. Method	
		Arc a	Arc b	Arc a	Arc b	Arc a	Arc b
ΔV	$[km/s]$	0.7250		0.6449		0.6427	
ΔV	$[km/s]$	0.5468	0.1782	0.5028	0.1421	0.5017	0.1410
Δt	$[days]$	9.437	3.033	8.730	2.468	8.621	2.392
$\Delta V_{\Delta a}$	$[km/s]$			0.5003	-0.1331	0.4992	-0.1320
Δa	$[km]$	1066.79	-351.734	953.84	-253.84	951.70	-251.71
$\Delta V_{\Delta i}$	$[km/s]$			0.0355	-0.0355	0.0354	-0.0354
Δi	$[deg]$	0.1553	-0.1553	0.1735	-0.1735	0.1729	-0.1729
$\Delta\Omega_{tot}$	$[deg]$			57.89		57.95	
$\Delta\Omega_{J2}$	$[deg]$			-57.46		-57.52	
$\Delta V_{\Delta\Omega}$	$[km/s]$			0.0348	0.0348	0.2175	0.2175
$\Delta\Omega$	$[deg]$			0.2190	0.2190	0.2175	0.2175

Table 5.3: Results of the three methods for $\Delta a = 700\ km$, $\Delta i = 0°$, $\Delta\Omega = 10°$ and $\Delta t = 33.705\ d$.

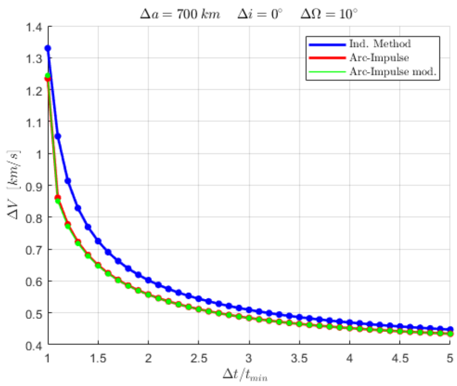

Figure 5.8: Trend of ΔV over $\Delta t/t_{min}$ ($\Delta a = 700\,km$ $\Delta i = 0°$ $\Delta\Omega = 10°$)

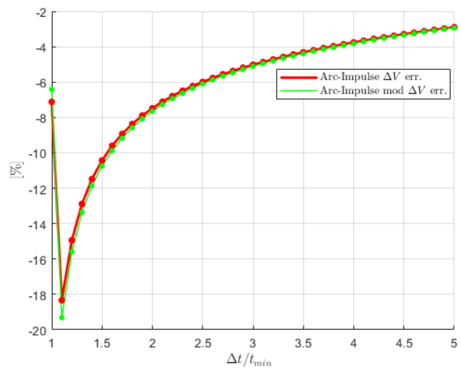

Figure 5.9: Trend of the relative error of ΔV for the two approximate methods ($\Delta a = 700\,km$ $\Delta i = 0°$ $\Delta\Omega = 10°$)

of the graph) is the same for both methods.

The solution of the modified arc-impulse method is similar to that of the arc-impulse method and does not provide any significant advantages. In terms of ΔV, the two approximate solutions show a 10% difference compared to the indirect solution, which is higher than the difference observed in the minimum-time solution.

Figure (5.8) shows the ΔV for this manoeuvre with different flight times. The ΔV initially decreases rapidly as the manoeuvre flight time increases: doubling the flight time results in a 55% reduction in ΔV. However, as the flight time continues to increase, the reduction in ΔV becomes less significant. All three solutions follow the same trend and tend to converge as the manoeuvre time increases. The maximum discrepancy between the methods is observed near the minimum flight time, where the slope of the curves is steeper.

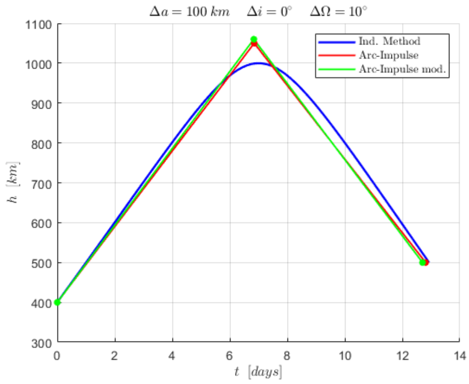

Figure 5.10: Trend of h over time (Minimum-time solution, $\Delta a = 100\, km$ $\Delta i = 0°$ $\Delta\Omega = 10°$)

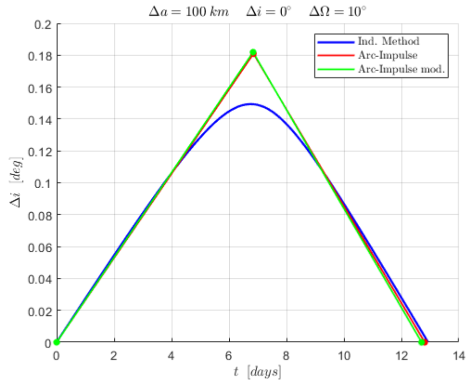

Figure 5.11: Trend of Δi over time (Minimum-time solution, $\Delta a = 100\, km$ $\Delta i = 0°$ $\Delta\Omega = 10°$)

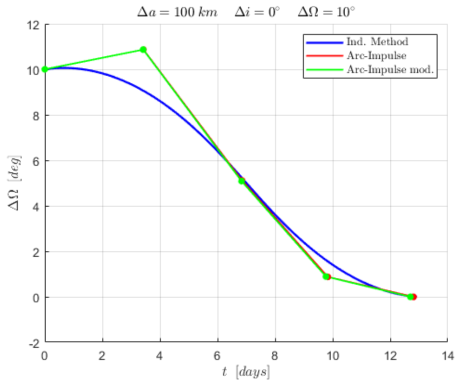

Figure 5.12: Trend of $\Delta\Omega$ over time (Minimum-time solution, $\Delta a = 100\, km$ $\Delta i = 0°$ $\Delta\Omega = 10°$)

5.1.2 Case 2 - Manoeuvre with $\Delta a = 100\ km$ and $\Delta\Omega = 10°$

5.1.2.1 Minimum time solution

As can be seen in figures (5.10) and (5.11), the strategy followed by the indirect method is the same as in case 1. This optimization strategy is commonly used when $\Delta\Omega > 0$ and the target orbit is higher than the chaser orbit. The maximum altitude and maximum Δi reached are significantly lower than in the previous case, as the target orbit is much closer to the chaser orbit. As shown in figure (5.12), $\Delta\Omega$ starts to decrease from the very beginning. It is worth noting that, in this case as well, the maximum Δi is reached before the maximum altitude ($t_{\Delta i_{max}} = 6.79; d$ and $t_{h_{max}} = 6.98; d$), but the temporal distance between the two peaks is much smaller. Regarding β, the trend is also similar to case 1. When Δi is close to its maximum, θ_0 is close to 90°, indicating a thrust contribution to change Ω, as shown in figure (5.12) with the point of maximum slope in the graph.

The approximate solutions follow the trend of the indirect solution much

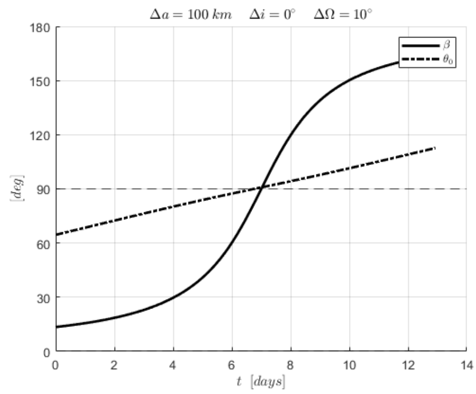

Figure 5.13: Trend of θ_0 and β angle over time in the indirect solution (Minimum-time solution, $\Delta a = 100\,km$ $\Delta i = 0°$ $\Delta\Omega = 10°$)

		Indirect Method		Arc-Imp. Method		Mod. Arc-Imp. Method	
		Arc a	Arc b	Arc a	Arc b	Arc a	Arc b
ΔV	$[km/s]$	0.7563		0.7379		0.7428	
Δt	$[days]$	12.9291		12.8120		12.7026	
ΔV	$[km/s]$	0.4016	0.3545	0.3946	0.3433	0.3946	0.397
Δt	$[days]$	6.884[2]	6.044	6.850	5.961	6.836	5.866
$\Delta V_{\Delta a}$	$[km/s]$			0.3657	-0.3098	0.3675	-0.3116
Δa	$[km]$	599.84	-499.84	653.64	-553.72	656.85	-556.94
$\Delta V_{\Delta i}$	$[km/s]$			0.0379	-0.0379	0.0381	-0.0381
Δi	$[deg]$	0.1493	-0.1493	0.1809	-0.1809	0.1818	-0.1818
$\Delta\Omega_{tot}$	$[deg]$			12.490		12.474	
$\Delta\Omega_{J2}$	$[deg]$			-10.731		-10.692	
$\Delta V_{\Delta\Omega}$	$[km/s]$			0.1431	0.1431	0.1451	0.145
$\Delta\Omega$	$[deg]$			0.8790	0.8790	0.8913	0.8907

Table 5.4: Results of the three methods for $\Delta a = 100\ km$, $\Delta i = 0°$, $\Delta\Omega = 10°$

.

more closely than in the previous case, due to the fact that the two peaks are very close in time. The maximum altitude and Δi reached are higher, but in terms of ΔV and Δt, the approximate methods are much closer to the indirect method, with only a 2% difference in ΔV and a 1% difference in Δt.

5.1.2.2 Minimum propellant solution

The minimum propellant solution considers a flight time of $\Delta t = 1.5 \cdot t_{min_{ind}}$. As can be seen in figures (5.14), (5.15), and (5.16), the approximate solutions are almost identical and closely follow the indirect solution. As in the previous case, the thrust arcs of the approximate solutions are shorter (about 6%), the altitude and Δi reached in the first arc differ by about 5%, but the effect on the reduction of $\Delta\Omega$ is the same as in the indirect method. The difference in ΔV is higher than in the minimum time propellant case; as shown before, this

[2] Average between $t_{h_{max}}$ and $t_{\Delta i_{max}}$

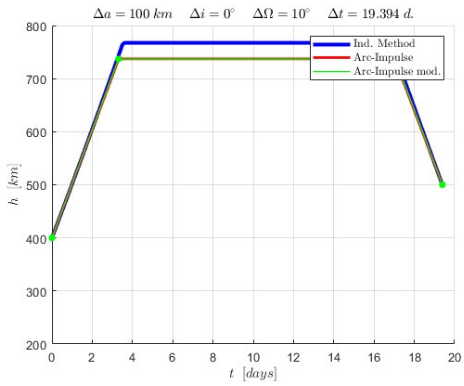

Figure 5.14: Trend of h over time (Minimum-propellant solution, $\Delta a = 100\,km$ $\Delta i = 0^\circ$ $\Delta\Omega = 10^\circ$, duration $= 19.394\,d$)

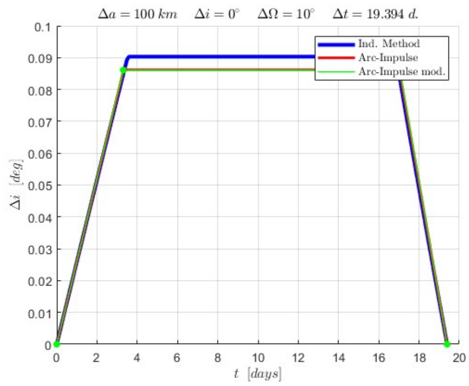

Figure 5.15: Trend of Δi over time (Minimum-propellant solution, $\Delta a = 100\,km$ $\Delta i = 0^\circ$ $\Delta\Omega = 10^\circ$, duration $= 19.394\,d$)

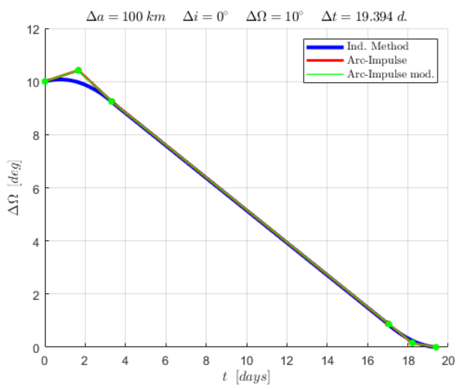

Figure 5.16: Trend of $\Delta\Omega$ over time (Minimum-propellant solution, $\Delta a = 100\,km$ $\Delta i = 0^\circ$ $\Delta\Omega = 10^\circ$, duration $= 19.394\,d$)

happens when the flight time is close to the minimum time.

5.1.3 Case 3 - Manoeuvre with $\Delta a = 1400\ km$ and $\Delta\Omega = 10^\circ$

5.1.3.1 Minimum time solution

In this case study, the altitude of the target orbit is significantly higher than that of the chaser orbit. This leads the indirect solution to reach a higher maximum altitude and a much larger Δi. While in the previous case the reduction of Δa caused the peaks of altitude and Δi to occur closer in time, in this case, the temporal gap increases: the maximum Δi is reached at $t_{\Delta i_{max}} = 20.93\ d$, and the maximum altitude is reached at $t_{h_{max}} = 23.95\ d$. The average between $t_{h_{max}}$ and $t_{\Delta i_{max}}$ is close to the duration of the first thrust arc of the approximate methods, with only a 3.5% difference. Regarding the β angle, the trend is

		Indirect Method		Arc-Imp. Method		Mod. Arc-Imp. Method	
		Arc a	Arc b	Arc a	Arc b	Arc a	Arc b
ΔV	$[km/s]$	0.3519		0.3279		0.3275	
ΔV	$[km/s]$	0.2041	0.1478	0.1913	0.1365	0.1912	0.1363
Δt	$[days]$	3.588	2.521	3.322	2.370	3.306	2.342
$\Delta V_{\Delta a}$	$[km/s]$			0.1887	-0.1327	0.1885	-0.1325
Δa	$[km]$	367.32	-267.32	337.25	-237.25	336.90	-236.90
$\Delta V_{\Delta i}$	$[km/s]$			0.01804	-0.01804	0.01802	-0.01802
Δi	$[deg]$	0.0903	-0.0903	0.0861	-0.0861	0.0860	-0.0860
$\Delta\Omega_{tot}$	$[deg]$			14.611		14.614	
$\Delta\Omega_{J2}$	$[deg]$			-14.287		-14.291	
$\Delta V_{\Delta\Omega}$	$[km/s]$			0.0263	0.0263	0.0262	0.0262
$\Delta\Omega$	$[deg]$			0.1620	0.1620	0.1615	0.1615

Table 5.5: Results of the three methods for $\Delta a = 100\ km$, $\Delta i = 0°$, $\Delta\Omega = 10°$ and $\Delta t = 19.394\ d$.

as expected, and when Δi is close to its maximum, θ_0 remains close to 90°, indicating a thrust contribution to the change in Ω.

The increase in Δa has made the differences between the indirect method and the arc-impulse methods more pronounced, as shown in figures (5.17), (5.18), and (5.19). The approximate solution has a shorter manoeuvre time (about 10% shorter), which is due to the longer timespan between $t_{\Delta i_{max}}$ and $t_{h_{max}}$. Additionally, the ΔV differs by about 13% from the indirect solution.

5.1.3.2 Minimum propellant solution

As in the previous cases, the minimum propellant solution considers a flight time of $\Delta t = 1.5 \cdot t_{min_{ind}}$. There are no significant differences compared to the previous cases; the trends of h and Δi are as expected for this type of transfer

[3] Average between $t_{h_{max}}$ and $t_{\Delta i_{max}}$

		Indirect Method		Arc-Imp. Method		Mod. Arc-Imp. Method	
		Arc a	Arc b	Arc a	Arc b	Arc a	Arc b
ΔV	$[km/s]$	2.1337		1.8345		1.8503	
Δt	$[days]$	35.476		31.850		30.946	
ΔV	$[km/s]$	1.3331	0.8004	1.2475	0.5869	1.2550	0.5953
Δt	$[days]$	22.438 [3]	13.037	21.658	10.190	21.244	9.702
$\Delta V_{\Delta a}$	$[km/s]$			1.2283	-0.5449	1.2347	-0.5513
Δa	$[km]$	2754.06	-1354.07	2516.24	-1116.26	2529.35	1129.37
$\Delta V_{\Delta i}$	$[km/s]$			0.0996	-0.0996	0.1003	-0.1003
Δi	$[deg]$	0.4497	-0.4497	0.4976	-0.4976	0.5011	-0.5011
$\Delta\Omega_{tot}$	$[deg]$			75.315		73.705	
$\Delta\Omega_{J2}$	$[deg]$			-72.820		-71.120	
$\Delta V_{\Delta\Omega}$	$[km/s]$			0.1940	0.1941	0.2011	0.2012
$\Delta\Omega$	$[deg]$			1.2471	1.2478	1.2928	1.2934

Table 5.6: Results of the three methods for $\Delta a = 1400\ km$, $\Delta i = 0°$, $\Delta\Omega = 10°$

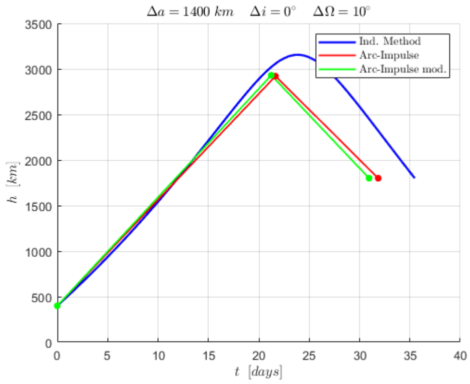

Figure 5.17: Trend of h over time (Minimum-time solution, $\Delta a = 1400\,km\ \Delta i = 0°\ \Delta\Omega = 10°$)

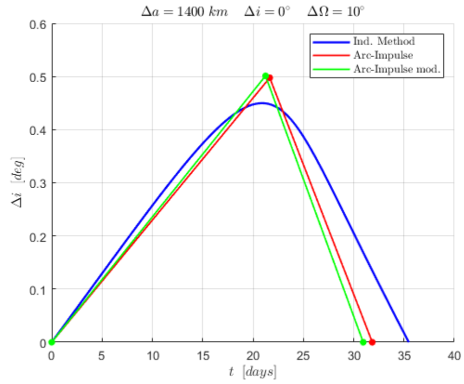

Figure 5.18: Trend of Δi over time (Minimum-time solution, $\Delta a = 1400\,km\ \Delta i = 0°\ \Delta\Omega = 10°$)

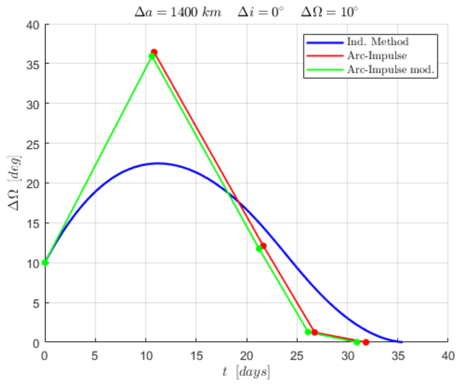

Figure 5.19: Trend of $\Delta\Omega$ over time (Minimum-time solution, $\Delta a = 1400\,km\ \Delta i = 0°\ \Delta\Omega = 10°$)

manoeuvre (figures (5.21) and (5.22)). The main differences lie in the maximum altitude reached and the respective durations of the thrust arcs, which are more pronounced between the indirect method and the arc-impulse methods. The approximate solutions reach a maximum altitude 16% lower and a maximum Δi 10% higher than the indirect solution. This leads the second thrust arc being half the duration of that in the indirect solution and results in a ΔV that is 20% lower.

5.1.4 Manoeuvre with different Δa

In the previous cases, we examined different transfer manoeuvres between orbits with the same orbital inclination but different altitudes. It is evident that as the Δa between the target and chaser orbits increases, the error introduced by using the approximate method becomes more pronounced.

This can be observed in figures (5.24) and (5.25), where the results in terms of ΔV and Δt for minimum-time transfer manoeuvres are presented. In the

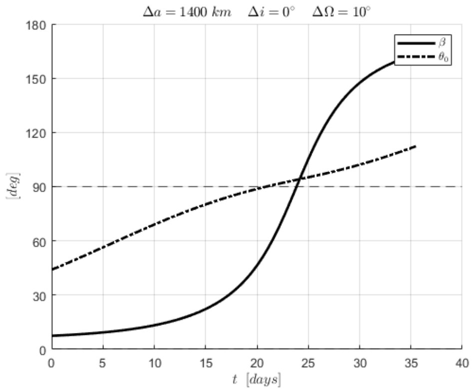

Figure 5.20: Trend of θ_0 and β angle over time in the indirect solution (Minimum-time solution, $\Delta a = 1400\,km$ $\Delta i = 0^\circ$ $\Delta\Omega = 10^\circ$)

		Indirect Method		Arc-Imp. Method		Mod. Arc-Imp. Method	
		Arco a	Arco b	Arco a	Arco b	Arco a	Arco b
ΔV	$[km/s]$	1.1916		0.9716		0.9661	
ΔV	$[km/s]$	0.9397	0.2518	0.8213	0.1502	0.8185	0.1475
Δt	$[days]$	16.230	4.257	14.260	2.608	13.977	2.470
$\Delta V_{\Delta a}$	$[km/s]$			0.8187	-0.1353	0.8160	-0.1325
Δa	$[km]$	2002.57	-602.57	1677.27	-277.27	1671.60	-271.6
$\Delta V_{\Delta i}$	$[km/s]$			0.0535	-0.0535	0.0532	-0.0532
Δi	$[deg]$	0.2455	-0.2455	0.2677	-0.2677	0.2661	-0.2661
$\Delta\Omega_{tot}$	$[deg]$			136.726		136.896	
$\Delta\Omega_{J2}$	$[deg]$			-136.250		-136.423	
$\Delta V_{\Delta\Omega}$	$[km/s]$			0.0371	0.0371	0.0367	0.0367
$\Delta\Omega$	$[deg]$			0.2387	0.2387	0.2362	0.2362

Table 5.7: Results of the three methods for $\Delta a = 1400\ km$, $\Delta i = 0^\circ$, $\Delta\Omega = 10^\circ$ and $\Delta t = 53.215\ d$.

indirect method, as the target orbit altitude increases, the cost of the manoeuvre and the minimum flight-time tend to grow in a non-linear fashion. Meanwhile, the two approximate solutions tend to grow in a more linear manner, causing the solutions to drift apart. For transfer manoeuvres with $\Delta a <$ 600-700 km ($\Delta a/a \simeq 0.1$), the difference between the indirect and approximate solutions is less than 5%, and for manoeuvres with $\Delta a <$ 1200 km ($\Delta a/a \simeq 0.2$), the difference is less than 10%. However, for larger Δa, the difference grows rapidly.

This behaviour is not unexpected. As discussed in the previous chapter, one of the assumptions considered in deriving the ΔV equation in the approximate method is that Δa should be small. As Δa increases, this assumption no longer holds true.

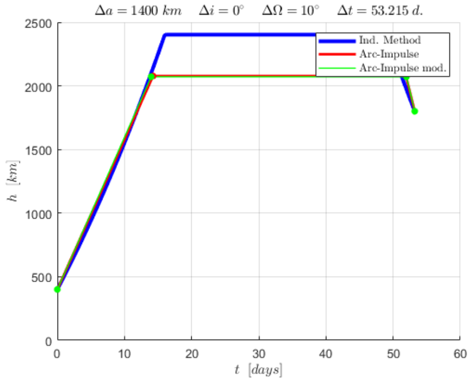

Figure 5.21: Trend of h over time (Minimum-propellant solution, $\Delta a = 1400\,km$ $\Delta i = 0°$ $\Delta\Omega = 10°$, duration $= 53.215\,d$)

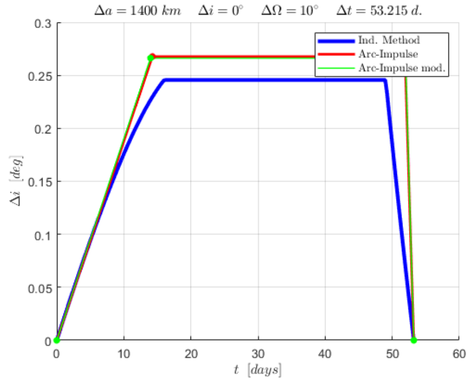

Figure 5.22: Trend of Δi over time (Minimum-propellant solution, $\Delta a = 1400\,km$ $\Delta i = 0°$ $\Delta\Omega = 10°$, duration $= 53.215\,d$)

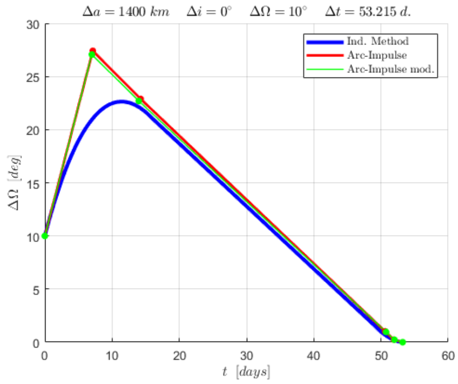

Figure 5.23: Trend of $\Delta\Omega$ over time (Minimum-propellant solution, $\Delta a = 1400\,km$ $\Delta i = 0°$ $\Delta\Omega = 10°$, duration $= 53.215\,d$)

5.2 Change of altitude with $\Delta\Omega < 0$

5.2.1 Case 1 - $\Delta a = 700\ km$ and $\Delta\Omega = -20°$

5.2.1.1 Minimum time solution

In this case study, the strategy followed by the indirect method is the opposite of that used in the corresponding case with $\Delta\Omega > 0$. As shown in Figure (5.27), the altitude of the chaser orbit is initially decreased, reaching a minimum altitude of h_{min} = 150 km at $t_{h_{min}}$ = 3.56 d, after which the altitude is increased to achieve the desired target orbit. A similar trend is observed for Δi in Figure (5.28), where the inclination of the chaser orbit initially decreases, reaching a minimum of $\Delta i_{min} = -0.1816°$ at $t_{\Delta i_{min}} = 4.91$ d, before increasing to match the target orbit's inclination.

This strategy aims to maximize the effect of differential precession between

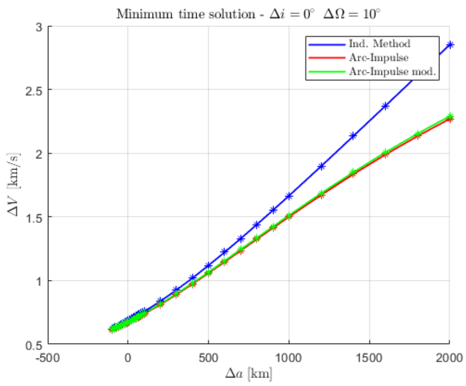

Figure 5.24: Trend of ΔV over Δa for minimum time solution ($\Delta i = 0°$ $\Delta\Omega = 10°$)

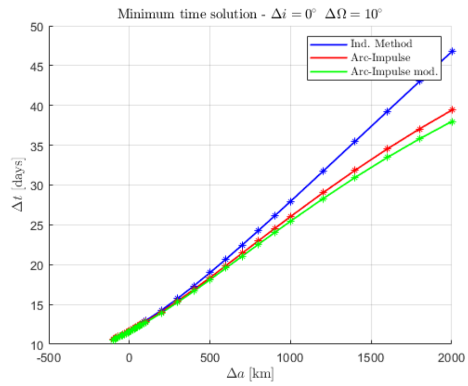

Figure 5.25: Trend of Δt over Δa for minimum time solution ($\Delta i = 0°$ $\Delta\Omega = 10°$)

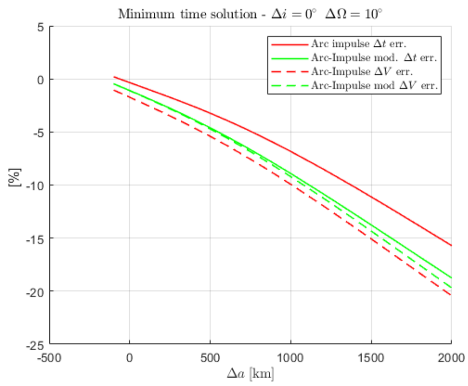

Figure 5.26: Relative error between approximate solutions and indirect solution ($\Delta i = 0°$ $\Delta\Omega = 10°$)

the two orbits, in order to optimize $\Delta\Omega$ change. Since the target orbit's ascending node is behind that of the chaser orbit, and since the chaser orbit's ascending node regresses faster, the two orbits naturally tend to close the $\Delta\Omega$ gap. Decreasing both the altitude and orbital inclination enhances this effect.

It is worth noting that, in this case, the minimum altitude is reached before the minimum Δi, which is the opposite behaviour observed in cases with $\Delta\Omega > 0$, where the peak of Δi occurred before the maximum altitude. This suggests that the observed behaviour is due to the fact that the lower the orbit, the more effective the inclination change due to J2 perturbation, thus optimizing the change in $\Delta\Omega$.

This phenomenon is evident in the trends of β and θ_0 over time, as shown in Figure (5.30). At t_0, the thrust is used to reduce both the altitude and the orbital inclination, and at $t_{h_{min}}$, β reaches 90°. Subsequently, the thrust is directed to increase the altitude while the orbital inclination continues to decrease. At $t_{\Delta i_{min}}$, Δi starts to increase. Around this point, θ_0 is close to $-90°$, indicating that the out-of-plane thrust effort is used to change Ω. This

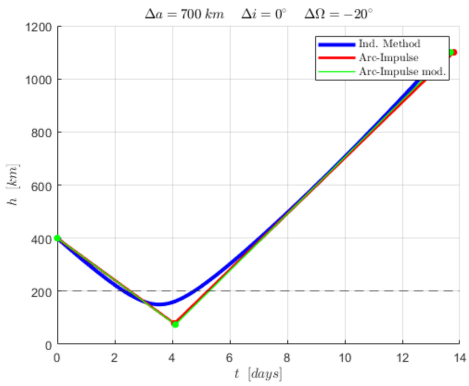

Figure 5.27: Trend of h over time (Minimum-time solution, $\Delta a = 700\,km$ $\Delta i = 0°$ $\Delta\Omega = -20°$)

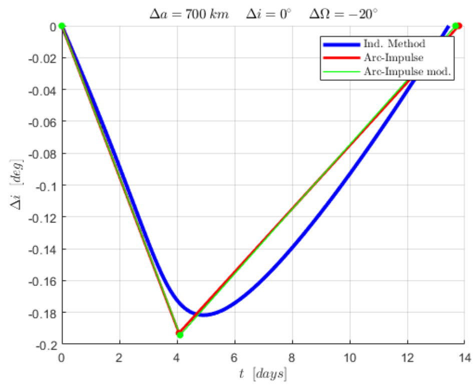

Figure 5.28: Trend of Δi over time (Minimum-time solution, $\Delta a = 700\,km$ $\Delta i = 0°$ $\Delta\Omega = -20°$)

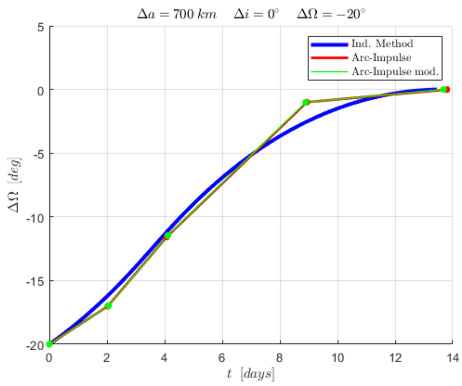

Figure 5.29: Trend of $\Delta\Omega$ over time (Minimum-time solution, $\Delta a = 700\,km$ $\Delta i = 0°$ $\Delta\Omega = -20°$)

is also evident in Figure (5.29), marked by the point of maximum slope. It is important to mention that the minimum altitude reached is below 200 km, a value conventionally considered the boundary of the atmosphere. This could render the obtained solution impractical, as the perturbative effects of atmospheric drag are not accounted for in this analysis. To make up for this limitation, a constraint on the minimum reachable altitude should be implemented in the indirect method algorithm.

Regarding the two approximate solutions, the strategy followed is the same, and the trends of altitude and Δi over time follow those of the indirect solution. The main difference is that the minimum altitude and the minimum Δi reached are lower, but the effect of the $\Delta\Omega$ reduction is similar to that of the indirect solution. The duration of the first arc t_a is close to the average between $t_{h_{min}}$ and $t_{\Delta i_{min}}$, as noted in the previous cases. In terms of ΔV and Δt, the approximate solutions are closer to the indirect solution, much more so than the corresponding cases with $\Delta\Omega > 0$, with only a 1% difference in ΔV and a 2% difference in Δt.

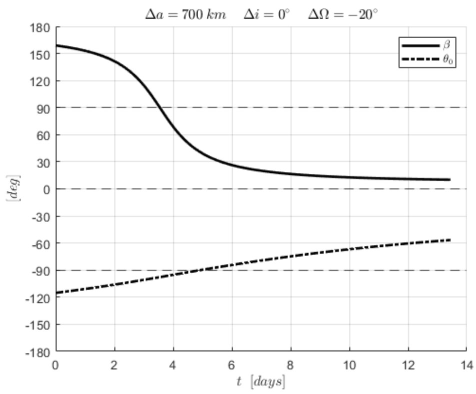

Figure 5.30: Trend of θ_0 and β angle over time in the indirect solution (Minimum-time solution, $\Delta a = 700\,km$ $\Delta i = 0°$ $\Delta\Omega = -20°$)

		Indirect Method		Arc-Imp. Method		Mod. Arc-Imp. Method	
		Arc a	Arc b	Arc a	Arc b	Arc a	Arc b
ΔV	$[km/s]$	0.7869		0.7945		0.8008	
Δt	$[days]$	13.445		13.793		13.679	
ΔV	$[km/s]$	0.2452	0.5417	0.2345	0.5600	0.2379	0.5630
Δt	$[days]$	4.235 [4]	9.210	4.071	9.722	4.109	9.570
$\Delta V_{\Delta a}$	$[km/s]$			-0.1686	0.5358	-0.1710	0.5381
Δa	$[km]$	-250.09	950.09	-321.40	1021.40	-325.92	1025.92
$\Delta V_{\Delta i}$	$[km/s]$						
Δi	$[deg]$	-0.1816	+0.1816	-0.1929	0.1929	-0.1942	0.1942
$\Delta\Omega_{tot}$	$[deg]$			-6.823		-6.879	
$\Delta\Omega_{J2}$	$[deg]$			4.838		4.864	
$\Delta V_{\Delta\Omega}$	$[km/s]$			-0.1581	-0.1581	-0.1605	-0.1605
$\Delta\Omega$	$[deg]$			-0.9924	-0.9924	-1.0074	-1.0074

Table 5.8: Results of the three methods for $\Delta a = 700\ km$, $\Delta i = 0°$ and $\Delta\Omega = -20°$

5.2.1.2 Minimum propellant solution

For this case study of the minimum propellant solution, a $\Delta t = 1.2 \cdot t_{min_{ind}}$ is considered. The expected strategy is the opposite of the strategies observed in the previous cases: a first thrust arc that decreases the altitude and the orbital inclination, followed by a coasting phase during which the thrust is turned off, and both the altitude and inclination remain constant. Finally, a second thrust arc increases the altitude and orbital inclination to the desired values.

As can be seen in Figure (5.31), the trend of altitude over time matches the expected behaviour, but the trend of Δi exhibits an unexpected behaviour (Figure (5.6)). The maximum Δi is reached during the second thrust arc, after which the orbital inclination increases to reach the desired value. This can be explained by examining the trend of β, shown in Figure (5.34). During the first thrust arc, the thrust vector is oriented to reduce the altitude, with a

[4] Average between $t_{h_{min}}$ and $t_{\Delta i_{min}}$

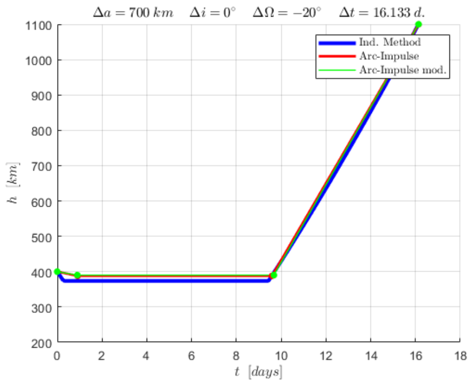

Figure 5.31: Trend of h over time (Minimum-propellant solution, $\Delta a = 700\,km$ $\Delta i = 0°$ $\Delta\Omega = -20°$, duration $= 16.133\,d$)

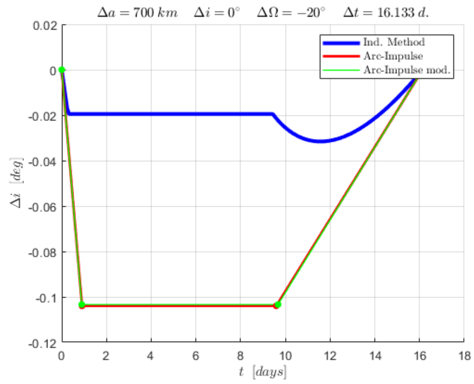

Figure 5.32: Trend of Δi over time (Minimum-propellant solution, $\Delta a = 700\,km$ $\Delta i = 0°$ $\Delta\Omega = -20°$, duration $= 16.133\,d$)

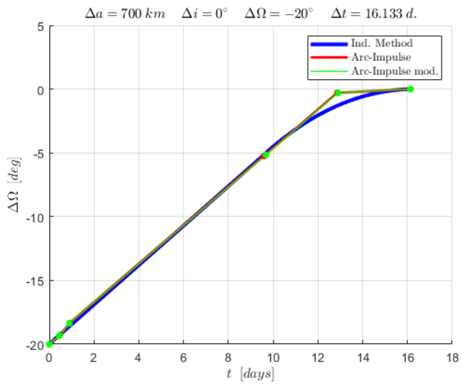

Figure 5.33: Trend of $\Delta\Omega$ over time (Minimum-propellant solution, $\Delta a = 700\,km$ $\Delta i = 0°$ $\Delta\Omega = -20°$, duration $= 16.133\,d$)

small out-of-plane component that decreases the orbital inclination. During the second arc, the thrust vector is oriented to increase the altitude, also with a small out-of-plane component that continues to decrease the orbital inclination. When Δi_{min} is reached, the inclination starts to increase. At this point, θ_0 is close to $-90°$, so the out-of-plane thrust component is used to reduce $\Delta\Omega$. When the in-plane thrust component is large, it is optimal to introduce a small out-of-plane thrust component (as observed in impulsive combined inclination and semi-major axis change manoeuvres), as in this case.

The approximate solutions do not exhibit this particular behaviour and show the expected pattern: a decrease during the first thrust arc, a coasting phase, and an increase during the second arc. The trend of Δi over time shows the most significant differences from the indirect solution. The first thrust arc decreases the orbital inclination much more than in the indirect solution. However, the altitude trend over time closely matches that of the indirect

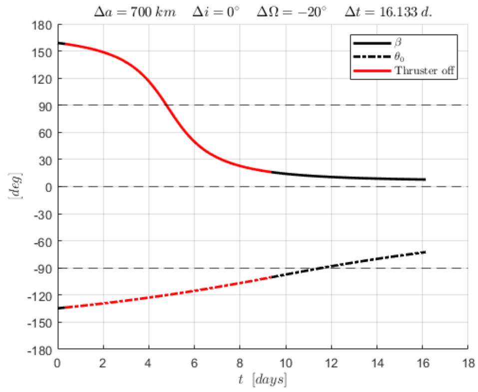

Figure 5.34: Trend of θ_0 and β angle over time in the indirect solution (Minimum-propellant solution, $\Delta a = 700\,km$ $\Delta i = 0°$ $\Delta\Omega = -20°$, duration $= 16.133\,d$)

		Indirect Method		Arc-Imp. Method		Mod. Arc-Imp. Method	
		Arc *a*	Arc *b*	Arc *a*	Arc *b*	Arc *a*	Arc *b*
ΔV	$[km/s]$	0.4054		0.4292		0.4275	
ΔV	$[km/s]$	0.0160	0.3893	0.0523	0.3769	0.0517	0.3758
Δt	$[days]$	0.323	6.776	0.908	6.544	0.897	6.461
$\Delta V_{\Delta a}$	$[km/s]$			-0.0062	0.3733	-0.0051	0.3723
Δa	$[km]$	-26.273	726.273	-11.7663	711.7663	-9.721	709.716
$\Delta V_{\Delta i}$	$[km/s]$			-0.0213	0.0213	-0.0212	0.0212
Δi	$[deg]$	-0.0195	-0.0316 [5]	-0.1040	0.1040	-0.1034	0.1034
$\Delta\Omega_{tot}$	$[deg]$			-1.025		-0.967	
$\Delta\Omega_{J2}$	$[deg]$			0.431		0.377	
$\Delta V_{\Delta\Omega}$	$[km/s]$			-0.0473	-0.0473	-0.0469	-0.0469
$\Delta\Omega$	$[deg]$			-0.2972	-0.2972	-0.2945	-0.2945

Table 5.9: Results of the three methods for $\Delta a = 700\ km$, $\Delta i = 0°$ e $\Delta\Omega = -20°$ and $\Delta t = 16.133\ d$.

solution. Another difference is that the first thrust arc is longer due to the larger ΔV of the first impulse (as a result of the greater Δi). The duration of the second thrust arc is similar to that of the indirect solution.

It is interesting to note that the solution is close to a 'waiting' type strategy, where the first thrust arc is eliminated, leaving only an initial coasting phase followed by a thrust arc that leads to the desired orbit.

5.2.2 Case 2 - $\Delta a = 100\ km$ and $\Delta\Omega = -20°$

5.2.2.1 Minimum time solution

Looking at the trend of altitude over time (Figure (5.35)), it can be seen that this transfer manoeuvre is not feasible, as the minimum altitude reached is negative. As discussed earlier, a constraint on the minimum reachable

[5] Value of Δi_{min}

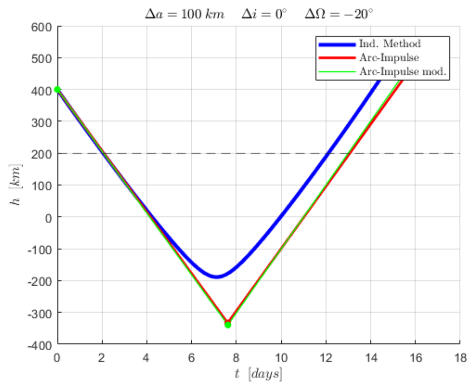

Figure 5.35: Trend of h over time (Minimum-time solution, $\Delta a = 100\,km$ $\Delta i = 0°$ $\Delta\Omega = -20°$)

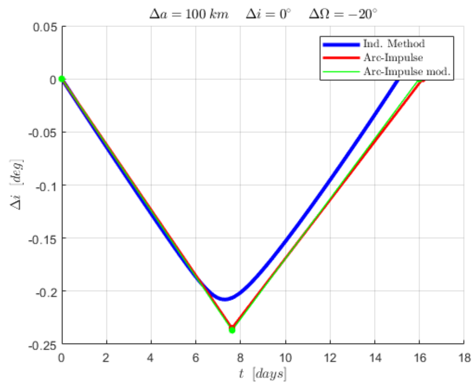

Figure 5.36: Trend of Δi over time (Minimum-time solution, $\Delta a = 100\,km$ $\Delta i = 0°$ $\Delta\Omega = -20°$)

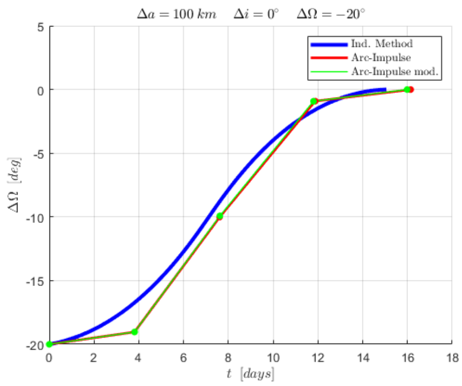

Figure 5.37: Trend of $\Delta\Omega$ over time (Minimum-time solution, $\Delta a = 100\,km$ $\Delta i = 0°$ $\Delta\Omega = -20°$)

altitude must be implemented, so this solution should only be considered a "mathematical" solution to discuss the differences between the indirect method and the arc-impulse methods. The strategy followed by the indirect solution consists of a decrease in altitude well below the target orbit, reaching the minimum altitude at $t_{h_{\min}} = 7.07\,d$, followed by an increase to reach the target altitude. The minimum altitude reached is much lower than in the previous case; this is necessary to exploit the J2 effect, as the target and chaser orbits are closer. The same behaviour applies to Δi, which reaches its minimum at $t_{\Delta i_{\min}} = 7.30\,d$. It is worth noting that the temporal distance between the two minima is shorter compared to Case 1, reflecting the same trend observed in cases with $\Delta\Omega > 0$.

This is also evident in Figure (5.38), where the point at which θ_0 crosses $-90°$ is very close to the point where β crosses $90°$. When Δi is at its minimum, θ_0 is close to $-90°$, meaning that the out-of-plane thrust effort is used to change Ω. The arc-impulse solution follows the same strategy as the indirect solution, but the minimum altitude reached is lower, and the magnitude of Δi is larger.

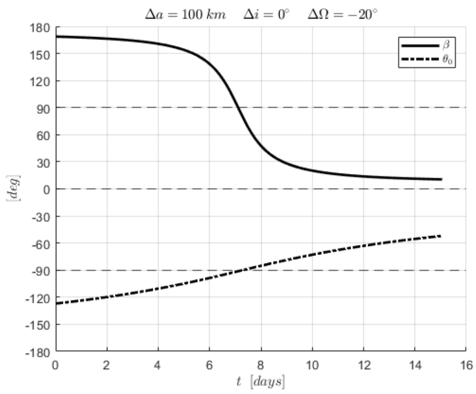

Figure 5.38: Trend of θ_0 and β angle over time in the indirect solution (Minimum-time solution, $\Delta a = 100\,km\ \Delta i = 0°\ \Delta\Omega = -20°$)

		Indirect Method		Arc-Imp. Method		Mod. Arc-Imp. Method	
		Arc a	Arc b	Arc a	Arc b	Arc a	Arc b
ΔV	$[km/s]$	0.8831		0.9296		0.9383	
Δt	$[days]$	15.058		16.138		15.982	
ΔV	$[km/s]$	0.4155	0.4676	0.4384	0.4912	0.4428	0.4955
Δt	$[days]$	7.190 [6]	7.868	7.612	8.527	7.619	8.364
$\Delta V_{\Delta a}$	$[km/s]$			0.4384	0.4912	-0.4137	0.4696
Δa	$[km]$	-588.926	688.926	-732.8463	832.8463	-739.388	839.388
$\Delta V_{\Delta i}$	$[km/s]$			-0.0492	0.0492	-0.0496	0.0496
Δi	$[deg]$	-0.2077	0.2077	-0.2348	0.2348	-0.2368	0.2368
$\Delta\Omega_{tot}$	$[deg]$			-16.992		-17.0114	
$\Delta\Omega_{J2}$	$[deg]$			15.1829		15.1689	
$\Delta V_{\Delta\Omega}$	$[km/s]$			-0.1473	-0.1473	-0.1500	-0.1500
$\Delta\Omega$	$[deg]$			-0.9047	-0.9047	-0.9213	-0.9213

Table 5.10: Results of the three methods for $\Delta a = 100\ km$, $\Delta i = 0°$ and $\Delta\Omega = -20°$

The second thrust arc is the one that deviates the most, as the first arc is longer. The ΔV shows a 5% difference from the indirect solution, while the Δt shows a 7% difference. The difference in ΔV and Δt between the methods is much larger than the corresponding cases with $\Delta\Omega > 0$.

5.2.2.2 Minimum propellant solution

For the minimum propellant solution a flight-time of $\Delta t = 1.2 \cdot t_{min_{ind}}$ is considered. The strategy followed by the indirect methods is the expected one (figures (5.39) and (5.40)): a three-phase manoeuvre, with a first thrust arc that decreases the chaser's altitude and orbital inclination, followed by a coasting phase in which the thrust is turned off, and a second thrust arc that increases the altitude and orbital inclination to reach the target orbit. The minimum altitude reached is higher, and the magnitude of Δi is smaller compared to the

[6] Average between $t_{h_{min}}$ and $t_{\Delta i_{min}}$

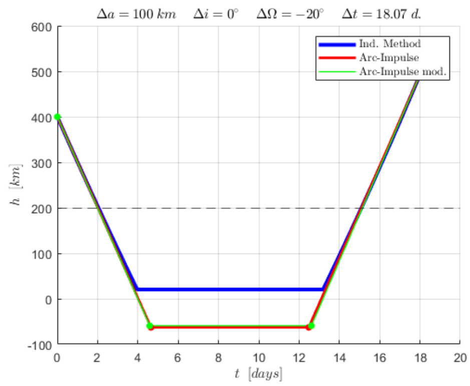

Figure 5.39: Trend of h over time (Minimum-propellant solution, $\Delta a = 100\,km$ $\Delta i = 0°$ $\Delta\Omega = -20°$, duration $= 18.07\,d$)

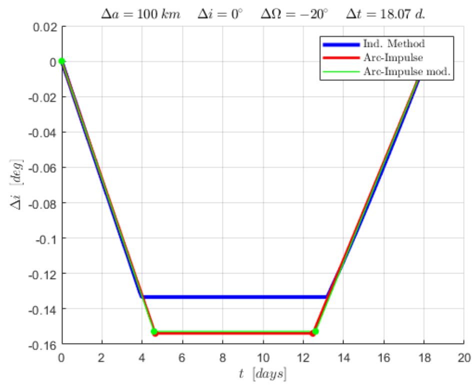

Figure 5.40: Trend of Δi over time (Minimum-propellant solution, $\Delta a = 100\,km$ $\Delta i = 0°$ $\Delta\Omega = -20°$, duration $= 18.07\,d$)

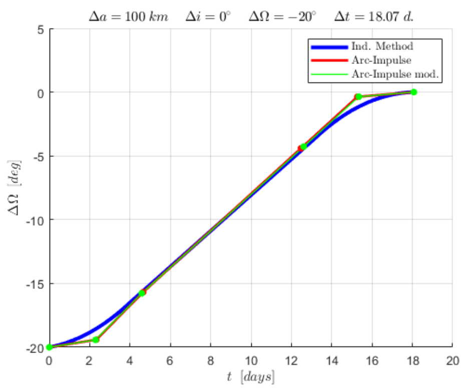

Figure 5.41: Trend of $\Delta\Omega$ over time (Minimum-propellant solution, $\Delta a = 100\,km$ $\Delta i = 0°$ $\Delta\Omega = -20°$, duration $= 18.07\,d$)

minimum-time solution, as the J2 effect can be exploited for a longer time.

The two arc-impulse solutions closely follow the trend of the indirect solution, but they reach a lower altitude and Δi, as observed in previous cases. The ΔV shows a 15% difference compared to the indirect solution.

5.2.3 Case 3 - $\Delta a = 1400\ km$ and $\Delta\Omega = -20°$

5.2.3.1 Minimum time solution

In this case study, the target orbit is significantly higher than the chaser orbit, resulting in a greater differential precession between the two orbits. As shown in Figure (5.44), at the beginning of the manoeuvre, $\Delta\Omega$ rapidly decreases. The first difference in the strategy followed by the indirect method, compared to the previous cases, is that the altitude is nearly monotonically increasing (Figure (5.42)). The trend of Δi over time is as expected (Figure (5.43)), with

		Indirect Method		Arc-Imp. Method		Mod. Arc-Imp. Method	
	Arc a	Arc b	Arc a	Arc b	Arc a	Arc b	
ΔV	$[km/s]$	0.5148		0.5901		0.5856	
ΔV	$[km/s]$	0.2294	0.2854	0.2678	0.3222	0.2656	0.3200
Δt	$[days]$	3.975	4.969	4.650	5.594	4.586	5.461
$\Delta V_{\Delta a}$	$[km/s]$			-0.2590	0.3149	-0.2569	0.3129
Δa	$[km]$	-379.59	479.59	-462.90	562.90	-459.22	559.22
$\Delta V_{\Delta i}$	$[km/s]$			-0.0322	0.0322	-0.0320	0.0320
Δi	$[deg]$	-0.1333	0.1333	-0.1539	0.1539	-0.1527	0.1527
$\Delta\Omega_{tot}$	$[deg]$			-16.132		-16.115	
$\Delta\Omega_{J2}$	$[deg]$			15.3934		15.387	
$\Delta V_{\Delta\Omega}$	$[km/s]$			-0.0601	-0.0601	-0.0593	-0.0593
$\Delta\Omega$	$[deg]$			-0.3695	-0.3695	-0.3641	-0.3641

Table 5.11: Results of the three methods for $\Delta a = 100\ km$, $\Delta i = 0°$, $\Delta\Omega = -20°$ and $\Delta t = 18.07\ d$.

the maximum $|\Delta i|$ reached being lower than in the previous cases.

The trend of the β angle (Figure (5.49)) shows a strong out-of-plane component of the thrust vector, at the beginning of the transfer manoeuvre, which slightly reduces the altitude while rapidly decreasing the orbital inclination. The out-of-plane component is then reduced, and when the inclination i is near its minimum, the out-of-plane component is used to change Ω (with θ_0 close to $-90°$). After this phase, the orbital inclination starts to increase, with a small out-of-plane component of the thrust vector. As previously discussed, this is optimal when the in-plane component of the thrust vector is large.

The strategy followed by the arc-impulse solution is slightly different in terms of the altitude trend. The first thrust arc slightly increases the orbital altitude instead of reducing it, while the second arc reaches the target orbit altitude. The Δi trend closely follows that of the indirect solution during the first arc but reaches a lower Δi.

In terms of ΔV and Δt, the two approximate solutions are much closer to the indirect solution compared to the corresponding maneuver with $\Delta\Omega > 0$, showing only a 2% difference in ΔV and a 3.5% difference in Δt.

5.2.3.2 Minimum propellant solution

If the transfer flight time is increased slightly from the Δt of the minimum-time solution (1.05 times larger), the optimal strategy for a minimum propellant solution is a 'waiting' type strategy, as shown in Figures (5.46) and (5.47). The first thrust arc is no longer present; the manoeuvre starts with a waiting phase on the chaser orbit, and after a period of time, the second thrust arc increases the altitude to reach the target orbit.

[7] Average between $t_{h_{min}}$ and $t_{\Delta i_{min}}$

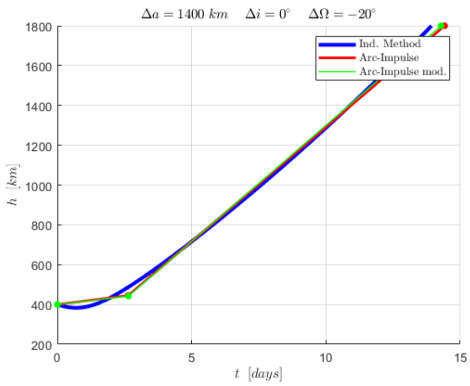

Figure 5.42: Trend of h over time (Minimum-time solution, $\Delta a = 1400\,km$ $\Delta i = 0°$ $\Delta\Omega = -20°$)

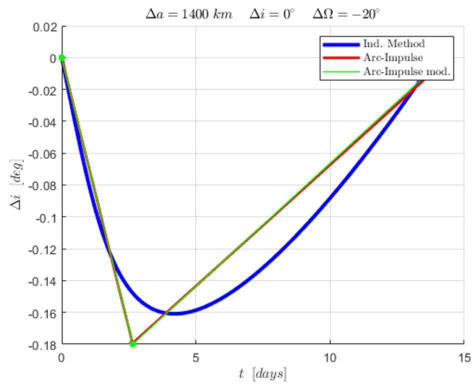

Figure 5.43: Trend of Δi over time (Minimum-time solution, $\Delta a = 1400\,km$ $\Delta i = 0°$ $\Delta\Omega = -20°$)

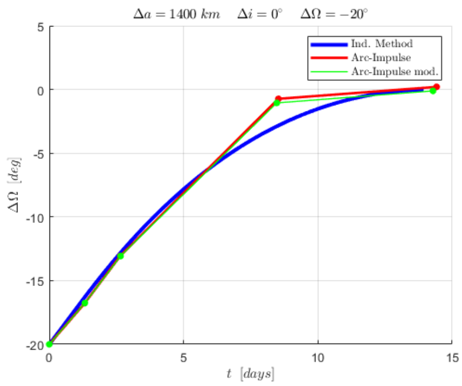

Figure 5.44: Trend of $\Delta\Omega$ over time (Minimum-time solution, $\Delta a = 1400\,km$ $\Delta i = 0°$ $\Delta\Omega = -20°$)

While the trend of altitude over time is monotonically increasing, Δi shows a decreasing-increasing trend, with the inclination of the chaser's orbit decreasing by a very small amount. Indeed, the in-plane components of the thrust vector is dominant over the out-of-plane component, as shown in Figure (5.49). The $\Delta\Omega$ gap is closed solely through the J2 effect, without involving the out-of-plane thrust.

The strategy followed by the arc-impulse solutions is a three-phase manoeuvre. The Δa is distributed between the two thrust arcs, and the Δi trend shows behavior similar to Case 1, with a change in orbital inclination larger than that of the indirect solution. Although the strategies differ, the solutions are very similar in terms of ΔV.

[8]Value of Δi_{min}

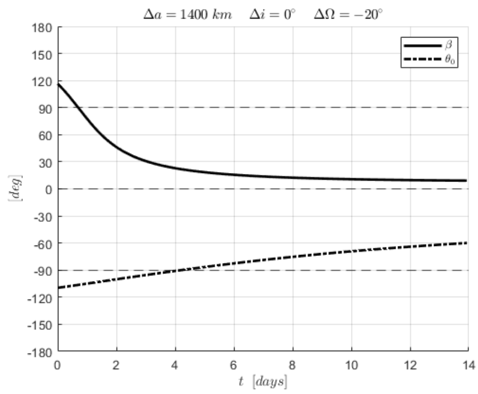

Figure 5.45: Trend of θ_0 and β angle over time in the indirect solution (Minimum-time solution, $\Delta a = 1400\,km$ $\Delta i = 0°$ $\Delta\Omega = -20°$)

		Indirect Method		Arc-Imp. Method		Mod. Arc-Imp. Method	
		Arc a	Arc b	Arc a	Arc b	Arc a	Arc b
ΔV	$[km/s]$	0.8160		0.8304		0.8325	
Δt	$[days]$	13.932		14.417		14.282	
ΔV	$[km/s]$	0.1974	0.6185	0.1520	0.6784	0.1528	0.6797
Δt	$[days]$	2.438 [7]	11.494	2.639	11.778	2.653	11.630
$\Delta V_{\Delta a}$	$[km/s]$			0.0219	0.6615	0.0207	0.6627
Δa	$[km]$	-16.89	1416.889	44.863	1355.12	42.40	1357.57
$\Delta V_{\Delta i}$	$[km/s]$			-0.0359	0.0359	-0.0360	0.0360
Δi	$[deg]$	-0.1607	0.1607	-0.1794	0.1794	-0.1799	0.1799
$\Delta\Omega_{tot}$	$[deg]$			-1.3745		-1.4214	
$\Delta\Omega_{J2}$	$[deg]$			-0.5034		-0.4687	
$\Delta V_{\Delta\Omega}$	$[km/s]$			-0.1461	-0.1460	-0.1470	-0.1470
$\Delta\Omega$	$[deg]$			-0.9393	-0.9386	-0.9450	-0.9450

Table 5.12: Results of the three methods for $\Delta a = 1400\ km$, $\Delta i = 0°$ and $\Delta\Omega = -20°$

5.3 Pure change of Ω

We observed in the previous case studies that in transfer manoeuvres with $\Delta\Omega > 0$, the maximum Δi is reached before the maximum altitude. When Δa is increased, the time gap between the two maxima tends to increase, while the opposite occurs when Δa is decreased.

For transfer manoeuvres with $\Delta\Omega < 0$, the minimum altitude is reached before the minimum orbital inclination, and decreasing Δa reduces the time gap between the two minima. This behaviour is due to the fact that changes in i are less effective for the J2 effect at higher altitudes. This result is obtained by appropriately adjusting the β angle of the thrust vector. We also noted that when Δi is close to its maximum (or minimum), the out-of-plane thrust effort is used to change Ω. The arc-impulse methods do not exhibit this behaviour, as the maxima (or minima) of altitude and Δi are reached simultaneously due to their impulsive nature. However, the duration of the thrust arc t_a is close to

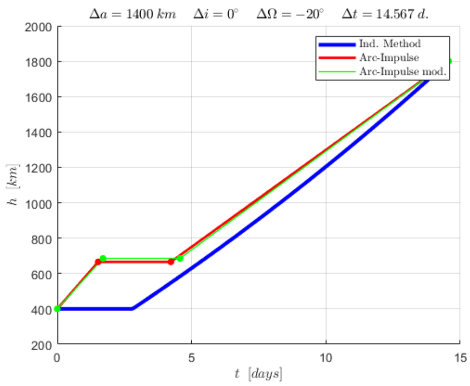

Figure 5.46: Trend of h over time (Minimum-propellant solution, $\Delta a = 1400\,km$ $\Delta i = 0°$ $\Delta\Omega = -20°$, duration $= 14.567\,d$)

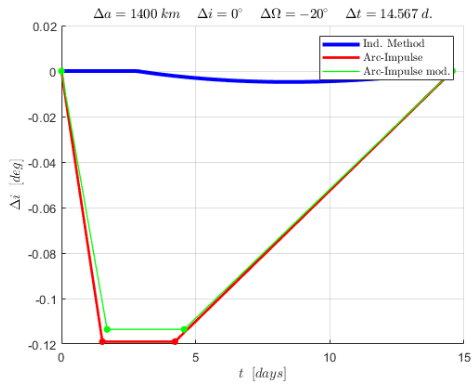

Figure 5.47: Trend of Δi over time (Minimum-propellant solution, $\Delta a = 1400\,km$ $\Delta i = 0°$ $\Delta\Omega = -20°$, duration $= 14.567\,d$)

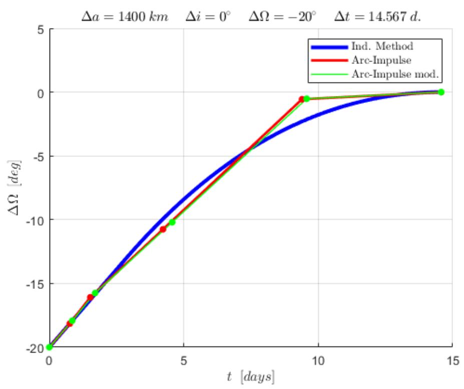

Figure 5.48: Trend of $\Delta\Omega$ over time (Minimum-propellant solution, $\Delta a = 1400\,km$ $\Delta i = 0°$ $\Delta\Omega = -20°$, duration $= 14.567\,d$)

the average of $t_{h_{\max}}$ and $t_{\Delta i_{\max}}$ (or between $t_{h_{\min}}$ and $t_{\Delta i_{\min}}$).

Figures (5.50), (5.51), and (5.52) show the trends of altitude, Δi, and $\Delta\Omega$ for a minimum-time transfer manoeuvre involving a pure change of Ω ($\Delta a = 0$ and $\Delta i = 0$). The strategy followed by the indirect method is similar to the other cases with $\Delta\Omega > 0$, featuring an increase-decrease trend. However, in this case, the solution is symmetrical, and the maxima of altitude and Δi are reached simultaneously at $t = 5.85\,d$.

The arc-impulse solution closely follows the same trend, with the duration of the first arc $t_a = 5.83\,d$ being close to that of the indirect solution. The two thrust arcs have the same duration, making the approximate solution symmetrical as well. The main difference lies in the fact that the achieved $h_{\max}$ and $\Delta i_{\max}$ are higher. The ΔV is close to that of the indirect solution, with a 1.5% difference. The same applies to Δt, with a difference of less than 1%.

This suggests that this behaviour is related to the simultaneous optimization

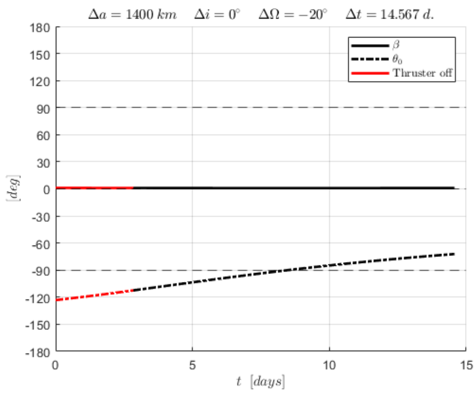

Figure 5.49: Trend of θ_0 and β angle over time in the indirect solution (Minimum-propellant solution, $\Delta a = 1400\,km$ $\Delta i = 0°$ $\Delta\Omega = -20°$, duration $= 14.567\,d$)

		Indirect Method		Arc-Imp. Method		Mod. Arc-Imp. Method	
		Arc a	Arc b	Arc a	Arc b	Arc a	Arc b
ΔV	$[km/s]$	0.6873		0.6834		0.6834	
ΔV	$[km/s]$	0	0.6873	0.0877	0.5956	0.0982	0.5852
Δt	$[days]$	0	11.727	1.524	10.341	1.702	9.999
$\Delta V_{\Delta a}$	$[km/s]$			0.1297	0.5537	0.1393	0.5441
Δa	$[km]$	0	1400	265.72	1134.28	285.38	1114.62
$\Delta V_{\Delta i}$	$[km/s]$			-0.0238	0.0238	-0.0227	0.0227
Δi	$[deg]$	0	-0.0048 [8]	-0.1190	0.1190	-0.1136	0.1136
$\Delta\Omega_{tot}$	$[deg]$			2.9465		3.3570	
$\Delta\Omega_{J2}$	$[deg]$			-4.0467		-4.3975	
$\Delta V_{\Delta\Omega}$	$[km/s]$			-0.0856	-0.0856	-0.0809	-0.0809
$\Delta\Omega$	$[deg]$			-0.5501	-0.5501	-0.5203	-0.5203

Table 5.13: Results of the three methods for $\Delta a = 1400\ km$, $\Delta i = 0°$ e $\Delta\Omega = -20°$ and $\Delta t = 14.567\ d$.

of two objectives: achieving Δa and reducing $\Delta\Omega$. It is worth noting that without the time gap between the two peaks, the arc-impulse solutions are much closer to the indirect solution in terms of ΔV and Δt.

Figure (5.53) and (5.55) shows the ΔV and Δt for minimum-time pure Ω-change transfer manoeuvres with different $\Delta\Omega$ values. The arc-impulse solutions are close to the indirect solutions for small $\Delta\Omega$ and tend to diverge as $\Delta\Omega$ increases. For $-10 < \Delta\Omega < 30$, the difference between the indirect and approximate solutions is less than 5%, while for $-40 < \Delta\Omega < 60$, the difference is less than 10%.

For comparison, Figures (5.54) and (5.56) show the ΔV and Δt for minimum-time transfer manoeuvres with $\Delta a = 700$ km and varying $\Delta\Omega$. In these cases, the solutions with $\Delta\Omega < 0$ tend to be much closer: for $-30 < \Delta\Omega < 15$, the difference between the indirect and arc-impulse solutions is less than 5%, while for $-70 < \Delta\Omega < 20$, the difference is less than 10%.

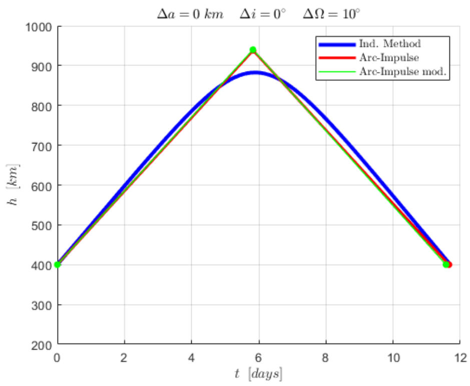

Figure 5.50: Trend of h over time (Minimum-time solution, $\Delta a = 0\,km$ $\Delta i = 0°$ $\Delta\Omega = 10°$)

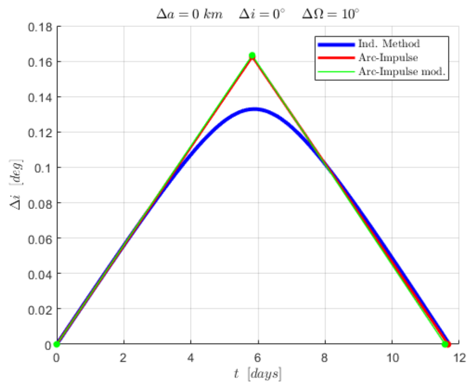

Figure 5.51: Trend of Δi over time (Minimum-time solution, $\Delta a = 0\,km$ $\Delta i = 0°$ $\Delta\Omega = 10°$)

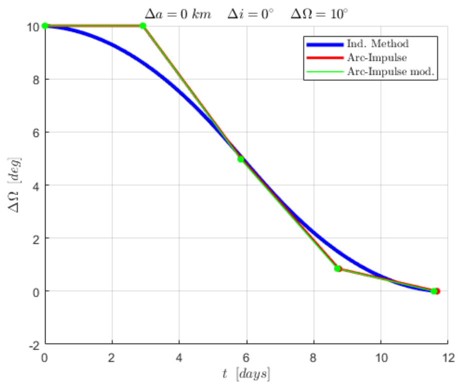

Figure 5.52: Trend of $\Delta\Omega$ over time (Minimum-time solution, $\Delta a = 0\,km$ $\Delta i = 0°$ $\Delta\Omega = 10°$)

For pure Ω-change manoeuvres with positive $\Delta\Omega$, the approximate solutions are more accurate because both solutions reach the maxima of altitude and Δi simultaneously. When $\Delta a \neq 0$, the solutions with negative $\Delta\Omega$ tend to be more accurate. This may be due to the fact that, as previously discussed, the methods do not include a constraint on the minimum reachable altitude. Therefore, in cases with $\Delta a = 0$, the minimum altitude can become too low or even negative in some cases.

5.4 Combined change of altitude inclination

5.4.1 Combined change of altitude orbital inclination with $\Omega > 0$

In this cases, in addition to reaching the required altitude, it is necessary to change the inclination of the chaser's orbit. For comparison, a $\Delta i = 1°$ and a $\Delta i = -1°$ are considered. Looking at Figures (5.57) and ((5.58), the trends

		Indirect Method		Arc-Imp. Method		Mod. Arc-Imp. Method	
		Arc a	Arc b	Arc a	Arc b	Arc a	Arc b
ΔV	$[km/s]$	0.6835		0.6716		0.6758	
Δt	$[days]$	11.703		11.661		11.573	
ΔV	$[km/s]$	0.3417	0.3417	0.3358	0.3358	0.3379	0.3379
Δt	$[days]$	5.851	5.851	5.830	5.831	5.827	5.747
$\Delta V_{\Delta a}$	$[km/s]$			0.3042	-0.3042	0.3057	-0.3057
Δa	$[km]$	482.58	482.58	537.79	-537.79	540.47	-540.47
$\Delta V_{\Delta i}$	$[km/s]$			0.0342	-0.0342	0.0343	-0.0343
Δi	$[deg]$	0.1329	0.1329	0.1625	-0.1625	0.1633	-0.1633
$\Delta\Omega_{tot}$	$[deg]$			10		10	
$\Delta\Omega_{J2}$	$[deg]$			-8.31		-8.29	
$\Delta V_{\Delta\Omega}$	$[km/s]$			0.1380	0.1380	0.1398	0.1398
$\Delta\Omega$	$[deg]$			0.8449	0.8449	0.8555	0.8555

Table 5.14: Results of the three methods for $\Delta a = 0\ km$, $\Delta i = 0°$ and $\Delta\Omega = 10°$

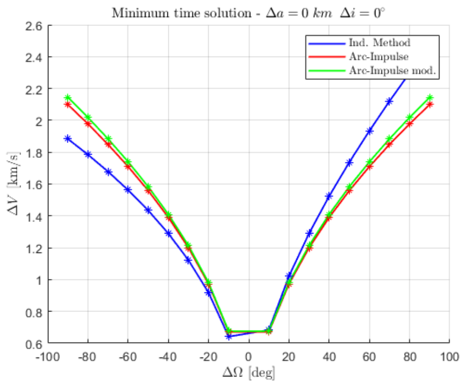

Figure 5.53: Trend of ΔV over $\Delta\Omega$ for minimum time manoeuvre with $\Delta a = 0$

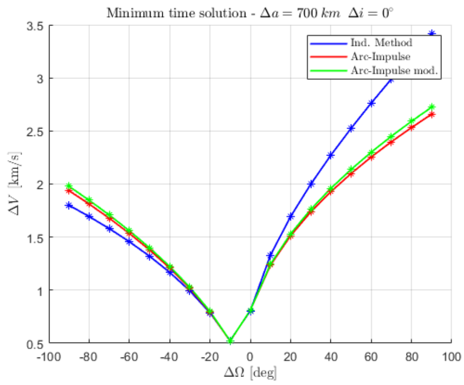

Figure 5.54: Trend of ΔV over $\Delta\Omega$ for minimum time manoeuvre with $\Delta a = 700\ km$

of altitude over time is similar to the corresponding case with $\Delta i = 0$: the chaser's altitude is increased beyond the target altitude, and then decreased to reach the desired altitude.

The trends of Δi (Figures (5.59) and ((5.60)) show different behaviours. In the case with $\Delta i = 1°$, the trend is almost monotonically increasing. In the final part of the manoeuvre, Δi slightly exceeds 1° and then decreases to reach the target orbital inclination.

Looking at Figure (5.61), we can see that in the first part of the manoeuvre, the in-plane thrust component is dominant (to increase the altitude), while the inclination increases due to a small out-of-plane thrust component. As the altitude increases, β starts to rise, as it becomes optimal to change the orbital inclination. When Δi is near its maximum, θ_0 approaches 90°, and the out-of-plane thrust component is primarily used to change Ω. This behaviour is due to the fact that the reduction of Δi to reach the target orbit inclination

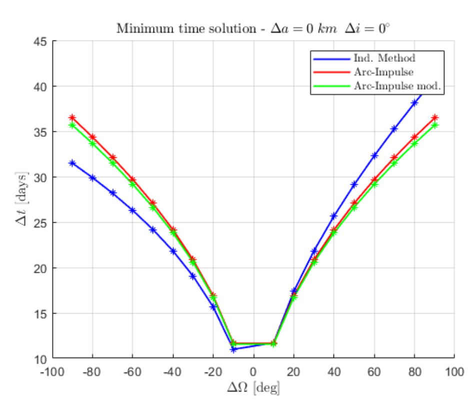

Figure 5.55: Trend of Δt over $\Delta\Omega$ for minimum time manoeuvre with $\Delta a = 0$

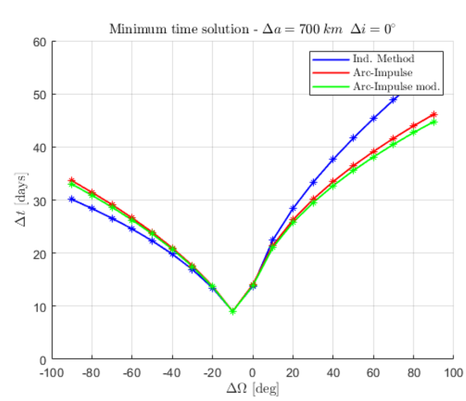

Figure 5.56: Trend of Δt over $\Delta\Omega$ for minimum time manoeuvre with $\Delta a = 700\ km$

is in contrast with the increase in Δi needed to optimize the reduction of $\Delta\Omega$.

In the case with $\Delta i = -1°$, the behaviour is also different. In the first half of the manoeuvre, the chaser's orbital inclination is slightly increased, and the out-of-plane thrust effort is used to change Ω (Figure (5.62)). When the altitude approaches its maximum, the inclination decreases rapidly to reach the desired value.

In the arc-impulse solutions, Δi does not exhibit the same behaviour: the total Δi is distributed between the two thrust arcs. However, similar trends are followed: in the case with $\Delta i = 1°$, the first arc achieves the largest portion of Δi, while in the case with $\Delta i = -1°$, it is the second arc that achieves the largest portion.

It is worth noting that the duration of the first arc is close to $t_{h_{\max}}$ in both cases. The differences in ΔV and Δt are similar to the corresponding cases with $\Delta i = 0$.

[9]time at h_{max}

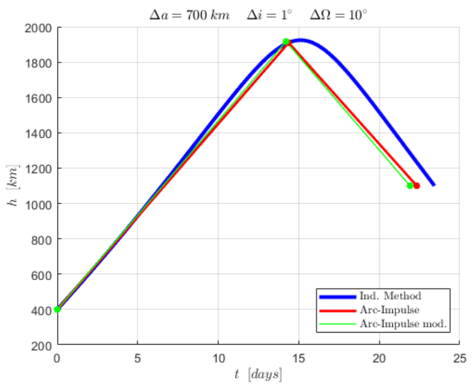

Figure 5.57: Trend of h over time for $\Delta i = 1$ (Minimum-time solution, $\Delta a = 700\,km$ $\Delta\Omega = 10°$)

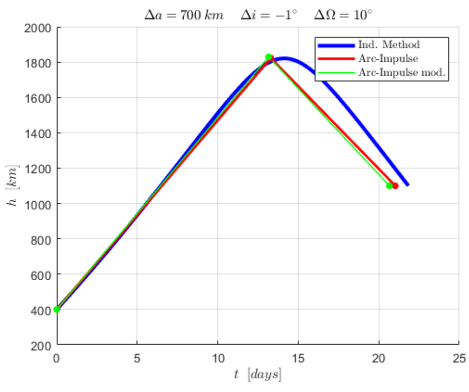

Figure 5.58: Trend of h over time for $\Delta i = -1$ (Minimum-time solution, $\Delta a = 700\,km$ $\Delta\Omega = 10°$)

		Indirect Method		Arc-Imp. Method		Mod. Arc-Imp. Method	
		Arc a	Arc b	Arc a	Arc b	Arc a	Arc b
ΔV	$[km/s]$	1.3879		1.2859		1.2953	
Δt	$[days]$	23.426		22.324		21.905	
ΔV	$[km/s]$	0.8861	0.5017	0.8277	0.4582	0.8322	0.4631
Δt	$[days]$	15.109[9]	8.316	14.370	7.955	14.206	7.699
$\Delta V_{\Delta a}$	$[km/s]$			0.7918	-0.4246	0.7955	-0.4283
Δa	$[km]$	1524.06	-824.06	1509.46	-809.46	1516.49	-816.49
$\Delta V_{\Delta i}$	$[km/s]$			0.1720	0.0330	0.1725	0.0325
Δi	$[deg]$			0.8392	0.1608	0.8412	0.1588
$\Delta\Omega_{tot}$	$[deg]$			38.4964		38.0571	
$\Delta\Omega_{J2}$	$[deg]$			-36.3891		-35.8982	
$\Delta V_{\Delta\Omega}$	$[km/s]$			0.1691	0.1691	0.1732	0.1732
$\Delta\Omega$	$[deg]$			1.0537	1.0537	1.0795	1.0795

Table 5.15: Results of the three methods for $\Delta a = 700\ km$, $\Delta i = 1°$ and $\Delta\Omega = 10°$

5.4.2 Combined change of altitude orbital inclination with $\Omega < 0$

The trends of altitude over time (Figures (5.63) and (5.64)) are as expected for cases with $\Delta\Omega < 0$: the altitude is first decreased and then increased to reach the target altitude.

The Δi trend in the $\Delta i = 1°$ case (Figure (5.65)) shows a significant increase in orbital inclination during the first half of the manoeuvre, due to the large out-of-plane component of the thrust vector (Figure (5.67)); in the second half, the orbital inclination continues to steadily increase with a small β angle. In the $\Delta i = -1°$ case (Figures (5.66)), the trend is similar, with an initial rapid decrease in orbital inclination due to the large β (Figure (5.68)), followed

[10] time at h_{max}

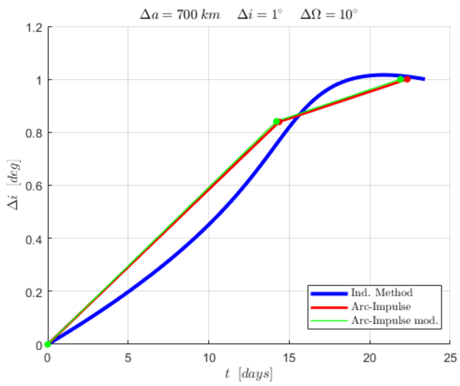

Figure 5.59: Trend of Δi over time for $\Delta i = 1$ (Minimum-time solution, $\Delta a = 700\,km$ $\Delta\Omega = 10°$)

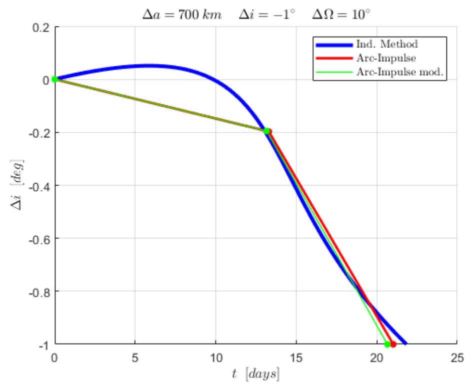

Figure 5.60: Trend of Δi over time for $\Delta i = -1$ (Minimum-time solution, $\Delta a = 700\,km$ $\Delta\Omega = 10°$)

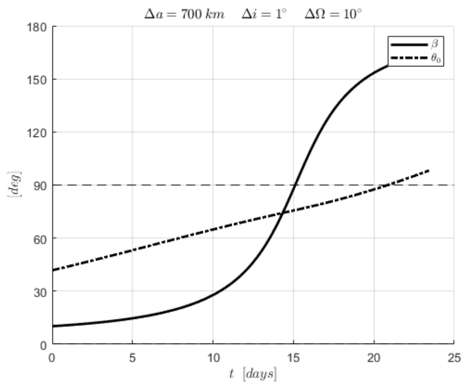

Figure 5.61: Trend of β and θ_0 over time for $\Delta i = 1°$ (Minimum-time solution, $\Delta a = 700\,km$ $\Delta\Omega = 10°$)

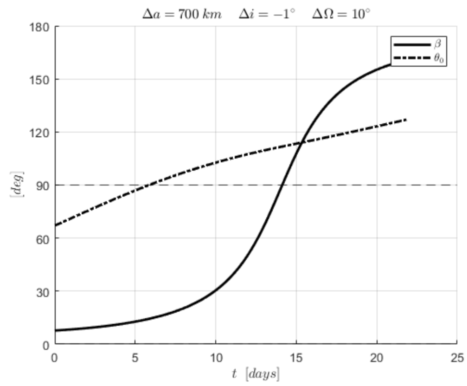

Figure 5.62: Trend of β and θ_0 over time for $\Delta i = -1°$ (Minimum-time solution, $\Delta a = 700\,km$ $\Delta\Omega = 10°$)

		Indirect Method		Arc-Imp. Method		Mod. Arc-Imp. Method	
		Arc a	Arc b	Arc a	Arc b	Arc a	Arc b
ΔV	$[km/s]$	1.2913		1.2110		1.2199	
Δt	$[days]$	21.838		21.023		20.663	
ΔV	$[km/s]$	0.8251	0.4662	0.7656	0.4453	0.7699	0.4500
Δt	$[days]$	14.085[10]	7.752	13.292	7.731	13.160	7.502
$\Delta V_{\Delta a}$	$[km/s]$			0.7464	-0.3792	0.7500	-0.3828
Δa	$[km]$	1420.85	-720.85	1423.02	-723.02	1429.83	-729.83
$\Delta V_{\Delta i}$	$[km/s]$			-0.0404	-0.1646	-0.0400	-0.1650
Δi	$[deg]$			-0.1971	-0.8029	-0.1952	-0.8048
$\Delta\Omega_{tot}$	$[deg]$			33.9912		33.6473	
$\Delta\Omega_{J2}$	$[deg]$			-31.8986		-31.5047	
$\Delta V_{\Delta\Omega}$	$[km/s]$			0.1655	0.1655	0.1695	0.1695
$\Delta\Omega$	$[deg]$			1.0463	1.0463	1.0713	1.0713

Table 5.16: Results of the three methods for $\Delta a = 700\ km$, $\Delta i = -1°$ and $\Delta\Omega = 10°$

by a continued decrease in the second half with a small out-of-plane thrust component. The arc-impulse solutions follow the trends of both altitude and Δi. In both cases, the total Δi is distributed between the two thrust arcs. It is worth mentioning that the end of the first arc (and the beginning of the second arc) is close to the point where the graph changes concavity.

5.4.3 Manoeuvre with different Δi

In the previous case studies, we considered $\Delta i = \pm 1°$. We observed that the differences between the indirect solution and the arc-impulse solution in terms of ΔV and Δt are of the same order of magnitude as the corresponding cases with $\Delta i = 0$.

Figures (5.69) and (5.70) show the ΔV and Δt for minimum-time transfer

[11] time at h_{min}
[12] time at h_{min}

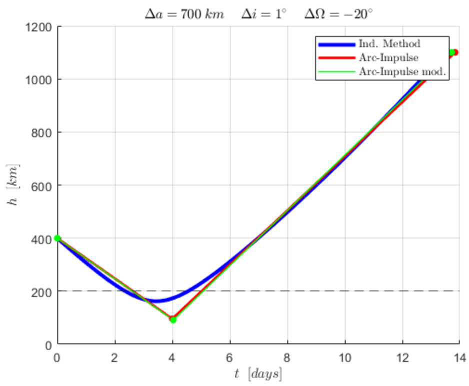

Figure 5.63: Trend of h over time for $\Delta i = 1$ (Minimum-time solution, $\Delta a = 700\,km$ $\Delta\Omega = -20°$)

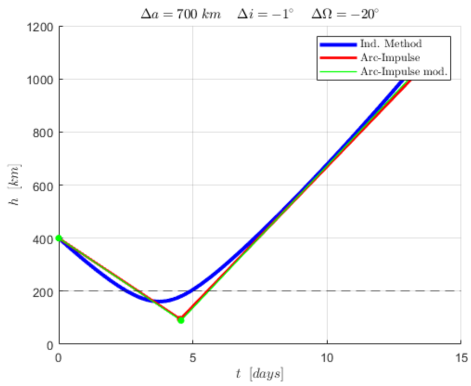

Figure 5.64: Trend of h over time for $\Delta i = -1$ (Minimum-time solution, $\Delta a = 700\,km$ $\Delta\Omega = -20°$)

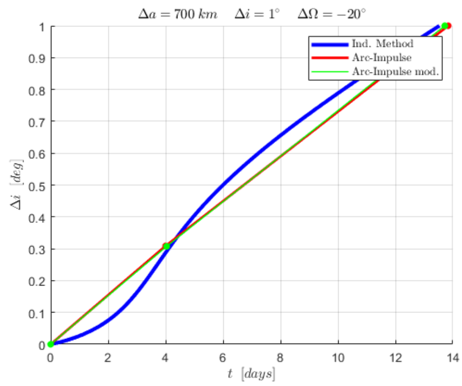

Figure 5.65: Trend of Δi over time for $\Delta i = 1$ (Minimum-time solution, $\Delta a = 700\,km$ $\Delta\Omega = -20°$)

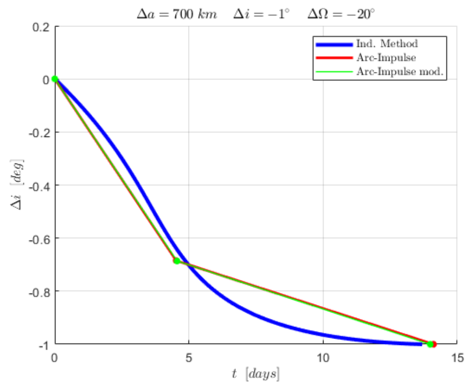

Figure 5.66: Trend of Δi over time for $\Delta i = -1$ (Minimum-time solution, $\Delta a = 700\,km$ $\Delta\Omega = -20°$)

manoeuvres with different values of Δi. As Δi increases, the ΔV and Δt of the indirect solution tend to grow in a non-linear fashion, whereas the two arc-impulse solutions exhibit a more linear growth. Consequently, for larger Δi values, the two methods tend to diverge.

For $-15° < \Delta i < 15°$, the difference between the two methods is less than 5%. This behaviour is not unexpected, since, as discussed in the previous chapter, one of the assumptions made when deriving the ΔV equation in the approximate method is that the quantity $\sqrt{\Delta i^2 + (\sin \bar{i} \Delta\Omega)^2}$ must be small. As Δi increases, this assumption no longer holds true.

		Indirect Method		Arc-Imp. Method		Mod. Arc-Imp. Method	
		Arc a	Arc b	Arc a	Arc b	Arc a	Arc b
ΔV	$[km/s]$	0.7921		0.7970		0.8032	
Δt	$[days]$	13.531		13.837		13.719	
ΔV	$[km/s]$	0.1996	0.5925	0.2304	0.5666	0.2336	0.5696
Δt	$[days]$	3.450 [11]	10.080	4.000	9.837	4.037	9.683
$\Delta V_{\Delta a}$	$[km/s]$			-0.1594	0.5266	-0.1619	0.5290
Δa	$[km]$	-237.72	937.72	-303.94	1003.94	-308.58	1008.58
$\Delta V_{\Delta i}$	$[km/s]$			0.0633	0.1417	0.0630	0.1420
Δi	$[deg]$	0.2167	0.7833	0.3087	0.6913	0.3073	0.6927
$\Delta\Omega_{tot}$	$[deg]$			-6.1478		-6.2100	
$\Delta\Omega_{J2}$	$[deg]$			4.2302		4.2624	
$\Delta V_{\Delta\Omega}$	$[km/s]$			-0.1538	-0.1538	-0.1562	-0.1562
$\Delta\Omega$	$[deg]$			-0.9588	-0.9588	-0.9738	-0.9738

Table 5.17: Results of the three methods for $\Delta a = 700\ km$, $\Delta i = +1°$ and $\Delta\Omega = -20°$

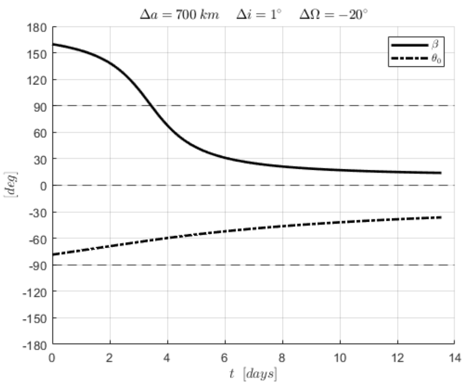

Figure 5.67: Trend of β and θ_0 over time for $\Delta i = 1°$ (Minimum-time solution, $\Delta a = 700\,km$ $\Delta\Omega = -20°$)

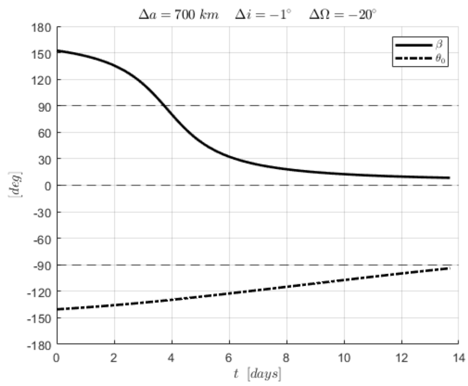

Figure 5.68: Trend of β and θ_0 over time for $\Delta i = -1°$ (Minimum-time solution, $\Delta a = 700\,km$ $\Delta\Omega = -20°$)

		Indirect Method		Arc-Imp. Method		Mod. Arc-Imp. Method	
		Arc a	Arc b	Arc a	Arc b	Arc a	Arc b
ΔV	$[km/s]$	0.8015		0.8128		0.8193	
Δt	$[days]$	13.690		14.112		13.989	
ΔV	$[km/s]$	0.2178	0.5837	0.2608	0.5521	0.2640	0.5553
Δt	$[days]$	3.765 [12]	9.925	4.527	9.585	4.559	9.430
$\Delta V_{\Delta a}$	$[km/s]$			-0.1600	0.5272	-0.1627	0.5299
Δa	$[km]$	238.87	938.87	-305.11	1005.11	-310.17	1010.17
$\Delta V_{\Delta i}$	$[km/s]$			-0.1404	-0.0646	-0.1407	-0.0643
Δi	$[deg]$	-0.5131	-0.4869	-0.6849	-0.3151	-0.6864	-0.3136
$\Delta\Omega_{tot}$	$[deg]$			-6.9689		-7.0330	
$\Delta\Omega_{J2}$	$[deg]$			5.0655		5.0981	
$\Delta V_{\Delta\Omega}$	$[km/s]$			-0.1505	-0.1505	-0.1530	-0.1530
$\Delta\Omega$	$[deg]$			-0.9517	-0.9517	-0.9675	-0.9675

Table 5.18: Results of the three methods for $\Delta a = 700\ km$, $\Delta i = -1°$ and $\Delta\Omega = -20°$

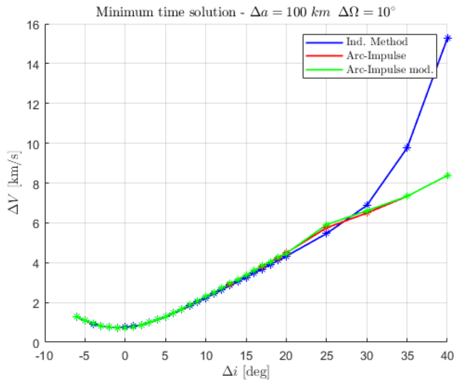

Figure 5.69: Trend of ΔV over Δi (Minimum-time solution, $\Delta a = 700\,km$ $\Delta\Omega = 10°$)

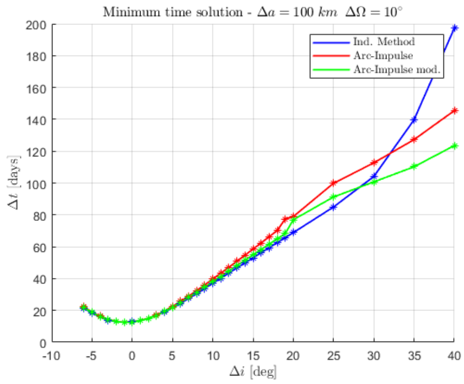

Figure 5.70: Trend of Δt over Δi (Minimum-time solution, $\Delta a = 700\,km$ $\Delta\Omega = 10°$)

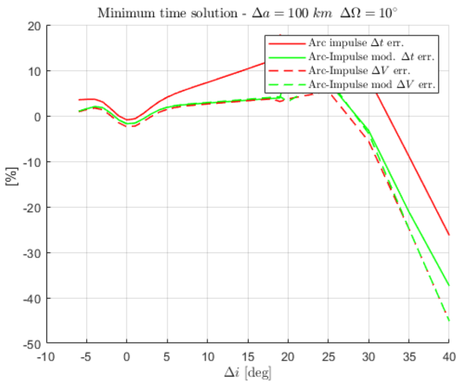

Figure 5.71: Relative error between approximate solutions and indirect solution (Minimum-time solution, $\Delta a = 700\,km$ $\Delta\Omega = 10°$)

Chapter 6

Conclusions

6.1 Conclusions

The increasing interest in LEO orbits for both commercial and scientific purposes, along with the growing population of space objects in these orbits, has drawn the attention of the scientific community to the problem of space debris. Whether for future Active Debris Removal (ADR) missions or other types of space operations, trajectory optimization plays a crucial role in mission design, aiming to minimize either flight time or propellant consumption.

After defining how an optimal control problem is formulated, two optimization methods have been considered: an indirect method, which relies on numerical solutions, and an approximate method that includes assumptions and relies on analytical solutions. The types of transfers analysed were single-target, many-revolution, low-thrust transfers. The dynamic model considered is the Edelbaum dynamic model whit the addition of the influence of the J_2 perturbation.

The indirect approach consists in reformulating the optimal control problem as a boundary value problem, solved using a shooting method; the system of differential equations is then solved numerically. In the Approximate Arc-Impulse method, the assumption of a small difference between the chaser and target orbits is introduced. The transfer cost is then evaluated using average quantities and the variations Δa, Δi, and $\Delta\Omega$. The transfer manoeuvre is initially treated as impulsive, and the impulses are subsequently converted into thrust arcs through an iterative process.

The optimal strategy obtained via indirect optimization shows that the effect of J_2 can be exploited to reduce the gap between RAAN by increasing (or decreasing) orbital altitude and inclination relative to the target orbit. This is achieved through the optimal control law governing the out-of-plane thrust angle β. The approximate method tends to follow the same transfer strategies but exhibits some differences. In the minimum-time solutions, the maximum (or minimum) values of altitude and inclination are reached simultaneously due to the "impulsive" nature of the approximation. However, this does not happen in the indirect solution, as it depends on the control law of β, which the approximate methods do not provide. The maximum (or minimum) altitude and inclination reached may also differ as a result of the optimization of the analytical equations. Furthermore, the duration of the thrust arcs may vary, as it is evaluated through ΔV.

The solutions provided by the indirect method are "exact", as they result from integrating the differential equations. However, implementing this method is more complex, and the use of a shooting method requires a good initial guess for the adjoint variables. Additionally, a large number of iterations is typically needed to converge to a solution. On the other hand, the Arc-Impulse method relies on algebraic formulas and converges within very few iterations (10–15), making its computational cost significantly lower than that of the indirect method.

Although the transfer strategy may differ (or be less accurate compared to the indirect approach), within its range of applicability—small changes in orbital elements—the transfer cost and minimum flight time remain accurate, with discrepancies below 5%. Therefore, the Arc-Impulse methods can be a useful tool for quickly assessing minimum flight time and transfer costs. This can be particularly advantageous when considering multi-target solutions for future ADR missions.

Bibliography

[1] Aerospace. "A brief history of space debris." (2022), [Online]. Available: https://aerospace.org/article/brief-history-space-debris (visited on 10/23/2024).

[2] R. R. Bate, D. D. Mueller, J. E. White, and W. W. Saylor, *Fundamentals of astrodynamics*. Courier Dover Publications, 2020 (cit. on pp. 11, 14, 16, 17, 19, 20, 22, 23, 34, 40).

[3] R. Buchs and M.-V. Florin, *Collision risk from space debris: Current status, challenges and response strategies*, 2021 (cit. on p. 6).

[4] L. Casalino, *Space Propulsion*. Politecnico di Torino, Department of Mechanical and Aerospace Engineering, 2024 (cit. on pp. 36, 38, 41, 50, 51).

[5] ESA. "About space debris." (2024), [Online]. Available: https://www.esa.int/Space_Safety/Space_Debris/About_space_debris (visited on 10/22/2024) (cit. on p. 6).

[6] ESA, *Active debris removal*, https://www.esa.int/Space_Safety/Space_Debris/Active_debris_removal, Accessed: 24/10/2024.

[7] ESA. "Clearspace-1." (2024), [Online]. Available: https://www.esa.int/Space_Safety/ClearSpace-1 (visited on 03/05/2025) (cit. on p. 10).

[8] ESA, *Esa multimedia*, https://www.esa.int/ESA_Multimedia/Images/2008/05/Earth_s_geoid_as_seen_by_GOCE, Accessed: 22/01/2025 (cit. on p. 24).

[9] ESA. "Esa space environment report 2024." (2024), [Online]. Available: https://www.esa.int/Space_Safety/Space_Debris/ESA_Space_Environment_Report_2024 (cit. on pp. 7, 8).

[10] ESA. "Esa's zero debris approach." (), [Online]. Available: https://www.esa.int/Space_Safety/Clean_Space/ESA_s_Zero_Debris_approach (visited on 10/23/2024).

[11] ESA. "New space debris mitigation policy and requirements in effect." (2024), [Online]. Available: https://esoc.esa.int/new-space-debris-mitigation-policy-and-requirements-effect (visited on 10/23/2024).

[12] ESA. "Space environment statistics." (2024), [Online]. Available: https://sdup.esoc.esa.int/discosweb/statistics/ (visited on 10/22/2024).

[13] R. G. Jahn, *Physics of electric propulsion*. Courier Corporation, 2006 (cit. on p. 42).

[14] D. E. Kirk, *Optimal control theory: an introduction*. Courier Corporation, 2004 (cit. on p. 45).

[15] H. G. Luke Shadbolt. "A brief history of space debris." (2023), [Online]. Available: https://www.hdi.global/globalassets/_local/international/newsroom/hdi_global_specialty_study_space_debris_2023_corpv5.pdf (visited on 10/23/2024).

[16] T. Maclay and D. McKnight, "Space environment management: Framing the objective and setting priorities for controlling orbital debris risk," *Journal of Space Safety Engineering*, vol. 8, no. 1, pp. 93–97, 2021 (cit. on p. 5).

[17] NASA. "Photo gallery." (2024), [Online]. Available: https://orbitaldebris.jsc.nasa.gov/photo-gallery/ (visited on 10/23/2024) (cit. on p. 2).

[18] A. V. Rao, "A survey of numerical methods for optimal control," *Advances in the astronautical Sciences*, vol. 135, no. 1, pp. 497–528, 2009 (cit. on p. 45).

[19] E. Russo, "Ottimizzazione di trasferte a bassa spinta tra orbite leo con perturbazione j2," Master's Thesis, Politecnico di Torino, 2023.

[20] H.-X. Shen, "Explicit approximation for j2-perturbed low-thrust transfers between circular orbits," *Journal of Guidance, Control, and Dynamics*, vol. 44, no. 8, pp. 1525–1531, 2021 (cit. on p. 58).

[21] G. P. Sutton, "Rocket propulsion elements: An introduction to the engineering of rockets," 1982 (cit. on p. 34).

[22] E. Todorov, *Optimal control theory*, Bayesian Brain, Doya, K. (ed), MIT Press (2006), 2006.

[23] D. A. Vallado, *Fundamentals of astrodynamics and applications*. Springer Science & Business Media, 2001, vol. 12 (cit. on pp. 11, 27, 28, 33).

[24] A. Verri, "Low-thrust many-revolutions maneuver optimization for future active debris removal applications," Master's Thesis, Politecnico di Torino, 2022.

[25] O. Von Stryk and R. Bulirsch, "Direct and indirect methods for trajectory optimization," *Annals of operations research*, vol. 37, pp. 357–373, 1992.

[26] K. F. Wakker, "Fundamentals of astrodynamics," *TU Delft Repository, Delft*, 2015 (cit. on pp. 11, 26, 34, 38).

Acknowledgments

Un ringraziamento è dovuto a tutte le persone che hanno contribuito e mi hanno supportato lungo questo percorso di studi, rendendo possibile la realizzazione di questo lavoro.

Prima di tutto, vorrei ringraziare i miei genitori, Cristina e Moreno, che hanno reso possibile il mio percorso universitario senza farmi mai mancare nulla, sostenendomi e incoraggiandomi. Un grazie speciale va anche alle mie sorelle, Martina e Chiara, che, affrontando carriere universitarie diverse, mi hanno offerto preziosi spunti di confronto, aiutandomi ad ampliare il mio bagaglio culturale e a osservare il mondo da prospettive diverse. Un pensiero speciale va a mia nonna Anna, che più di tutti desidera vedere il coronamento di questo percorso, e a mio nonno Beppe che, anche se non è più con noi, sarebbe stato felice di vedere questo sogno realizzarsi.

Desidero ringraziare i miei amici più stretti, che mi hanno accompagnato in questa fase della mia vita: Federico ed Eric, con cui ho condiviso la passione per la Scienza e lo Spazio; Leonardo, Samuele e Stefano, per le serate trascorse insieme; e infine Andrea, con cui ho condiviso gioie e difficoltà di questo corso di studi, tra infinite ore passate nei corridoi del Poli.

Infine, vorrei esprimere la mia gratitudine al mio relatore, il prof. Lorenzo Casalino, per aver reso possibile la realizzazione di questo progetto, per la pazienza, la disponibilità e il tempo che mi ha dedicato.